Naval Research Laboratory

Washington, DC 20375-5320

NRL/MR/6720--98-8144

Advanced Radiation Theory Support Annual Report 1997, Final Report

Radiation Hydrodynamics Branch
Plasma Physics Division

May 22, 1998

REPORT DOCUMENTATION PAGE

Form Approved
OMB No. 0704-0188

1. AGENCY USE ONLY (*Leave Blank*)	2. REPORT DATE	3. REPORT TYPE AND DATES COVERED
	May 22, 1998	Final Report

4. TITLE AND SUBTITLE

Advanced Radiation Theory Support Annual Report 1997, Final Report

5. FUNDING NUMBERS

6. AUTHOR(S)

Radiation Hydrodynamics Branch

7. PERFORMING ORGANIZATION NAME(S) AND ADDRESS(ES)

Naval Research Laboratory
Washington, DC 20375-5320

8. PERFORMING ORGANIZATION REPORT NUMBER

NRL/MR/6720--98-8144

9. SPONSORING/MONITORING AGENCY NAME(S) AND ADDRESS(ES)

Defense Special Weapons Agency
6801 Telegraph Road
Alexandria, VA 22310

10. SPONSORING/MONITORING AGENCY REPORT NUMBER

11. SUPPLEMENTARY NOTES

This research was sponsored by the Defense Special Weapons Agency under Job Order Titles, "Advanced Radiation Theory Support," MIPR No. 97-2009, "Operational Simulator Support," No. 97-2070, and "Decade Load PRS Design," No. 96-2167.

12a. DISTRIBUTION/AVAILABILITY STATEMENT

Approved for public release; distribution unlimited.

12b. DISTRIBUTION CODE

13. ABSTRACT (*Maximum 200 words*)

This report describes the work of the Radiation Hydrodynamics Branch during FY 97 in support of the DSWA PRS program. Critical issues covered are: (1) Long time implosions, power flow, and stability on Decade Quad, (2) Analysis of time resolved and time integrated Z-pinch data, (3) Spectroscopic PRS diagnosis, (4) Radiation magneto-hydrodynamics code development and assessment, and (5) Analysis of novel PRS loads.

14. SUBJECT TERMS

Decade quad
Radiation MHD
Transport coefficients
Z-pinch physics
Plasma radiation source
Long time implosions
Rayleigh-Taylor instability
Diagnostic line ratios

15. NUMBER OF PAGES

143

16. PRICE CODE

17. SECURITY CLASSIFICATION OF REPORT	18. SECURITY CLASSIFICATION OF THIS PAGE	19. SECURITY CLASSIFICATION OF ABSTRACT	20. LIMITATION OF ABSTRACT
UNCLASSIFIED	UNCLASSIFIED	UNCLASSIFIED	UL

CONTENTS

EXECUTIVE SUMMARY

This report describes the theory support of DSWA's Plasma Radiation Source (PRS) program carried out by NRL's Radiation Hydrodynamics Branch (Code 6720) in FY 1997. Included is work called for in MIPRs 97-2009, Advanced Radiation Theory Support, 97-2070, and 96-2167, Decade Load PRS Design.

The two major goals of the PRS program are to improve yields and fidelity. In this regard, it has been a landmark year as over 150 kJ of titanium K-shell x rays and 50 kJ of iron K-shell x rays were obtained from DSWA supported experiments on Sandia's Z generator as had been predicted by NRL Code 6720. In addition Code 6720 pioneered the nested wire array configuration that was instrumental in the achievement of 300 TW radiation power levels on Z. Z is a fast current rise time machine whereas DECADE QUAD is designed to be a longer rise time machine. A long rise time makes it essential that DECADE QUAD have the ability to efficiently extract K-shell emission from large radius loads. Indeed, when imploding conventional small initial radius loads, a long rise time machine like DECADE QUAD would have to produce twice as much short circuit current as a conventional short rise time water line machine in order to achieve the same K-shell emission from properly massed high-Z loads. Under these conventional conditions, any cost savings envisioned by using a long pulse machine are purely an illusion. Therefore, the effective conversion of the energy stored in DECADE/DECADE QUAD to high energy radiation (without an opening switch that performs significantly better than it has to date) requires the usage of large initial radius loads. Properly designed, with enough current to drive large number wire loads, the performance of DECADE could be equal to or exceed that of the Z generator. With this thought in mind, the work described in this report is directed towards the general goals of obtaining increased yields and fidelity as well as issues relevant to obtaining these goals with large radius loads. The subjects discussed are, section by section:

(1) In order to take full advantage of the energy that DECADE QUAD can deliver to a PRS load it will also be necessary, in addition to starting from large initial radius, to implode sufficient mass. However, as the mass is increased, the opacity of the pinch in critical regions of the x-ray spectrum such as the K-shell lines can strongly influence and diminish the achievable yield. This section

describes how this opacity problem can be mitigated and eliminated through the use of mixture plasmas. The basic approach employed is that it is better for a load to radiate four K-shell alpha lines from two elements, each of which has roughly half the optical depth of the two alpha lines that would result from a one-element load. This principle held up for an earlier series of Al:Mg loads shot on Double Eagle and it is further and more dramatically tested and analyzed using Al:Mg wire alloy loads and Al:Mg wires coated with KCl loads that were shot on the Saturn generator. The Saturn experimental results are also used to help answer the question: how tightly constrained are the properties of a pinch (which one would like to infer from a data analysis) by a given selection of data? In particular a strong argument is made that there is a decreasing temperature profile from the axis to the outer radius of the pinch in order to fit both Al and Mg spectral information. This deduction could not have been made with diagnostics only from a single element plasma. This potential for mixture plasma loads to both increase diagnostic understanding and to enhance yields is just starting to be realized. Mixture loads will without doubt play a large role in increasing fidelity and yield for future DSWA applications, and in advancing understanding of the important role of temperature gradients on x-ray yield performance.

(2) At present our 1D radiative magneto-hydrodynamic (1D RMHD) calculations and static analyses (e.g. the Al:Mg mixture analysis above) that give the best agreement with experimental data, have produced a consistent picture of a hot core plasma surrounded by a cooler halo plasma at larger radius. The 1D RMHD calculations also show that the core region can have an ion temperature one to two orders of magnitude larger than its electron temperature and densities orders of magnitude larger in the halo region than the core. It is important from the standpoint of fidelity that we understand these gradients as well as the origin and evolution of these large ion temperatures, which are also seen experimentally. It is important because, for high and medium atomic number loads, such as titanium, only the high temperature inner core regions may be sufficiently hot to achieve ionization into the titanium K-shell and produce 4-5 keV photon emission. In the 1D RMHD calculations it is found that adjustments to the coefficients of heat conductivity and viscosity were needed in order to give temperature and density gradients that match the data. The physical justification for these adjustments is that the classical values of the transport coefficients cannot account for some of the multi-dimensional effects of fluid turbulence. However before

such adjustments can be attributed entirely to turbulence, one must be certain the non-turbulent component of transport phenomena in a plasma is complete and adequately accounted for. This issue is addressed in this section by including a term that depends on the radial temperature gradient into the axial component of the electric field MHD equation. This term is usually neglected in 1D models, but because density and temperature gradients will be more severe in high current machines like DECADE, its effects need to be investigated. One of this term's important effects, discussed in Section II, is to reduce the size of the gradients. Analyzes of two sets of Saturn experiments in which array mass and radius were held fixed and the wire number was varied are also described in this section. More evidence for the existence of large temperature gradients and the importance of symmetry (as measured by wire gap spacing) in maintaining good K-shell yield production as the initial radius is increased are important additional results from this work.

(3)-(4) Large radius implosions are known to be susceptible to the Rayleigh Taylor (RT) instability. The extent to which this instability affects the ability of a large initial radius load to radiate K-shell photons is not known and is one of DSWA's important addressable issues. One way to establish a theoretical relationship between the RT instability of a load and its ability to efficiently radiate K-shell photons would be to perform two-dimensional (2D) or three-dimensional (3D), time dependent, non-LTE, full radiation transport, MHD calculations. However, this capability does not fully exist in the Z-pinch community primarily because the computer requirements for performing the zone-to-zone coupling needed to transport radiation in a 2D or 3D plasma are currently prohibitive. Even to adequately handle the 1D problem requires all of the computer resources currently available. Our 2D MHD model assumes that either the plasma is transparent to radiation or that a local probability of escape model can be used to model some of the self-absorption physics. The LTE radiative diffusion model, used by the 2D Z-pinch community, is also inadequate for modeling the radiation physics of PRS loads designed for super kilovolt K-shell emission because neither the diffusion approximation nor the LTE assumption are valid for this type of plasma. Given these model limitations, a technique for analyzing load K-shell emission capabilities was developed that allows us to use the strength of the 2D code to follow the fluid motion while still retaining the radiation transport advantages of the 1D codes. In Section III, this approach is applied to examining stability and its effect on K-shell yield performance on the front

running candidate for the first load to be fielded on DECADE QUAD, which is a uniform fill 3.6 cm initial radius load. Section IV examines uniform fill, hollow fill, and annular load implosions on DECADE QUAD. The uniform fill load initially has uniform density between the axis and the outer radius of the pinch while the hollow fill load is like a donut with a vacuum hole and uniform density between the inner and outer radii. Both Sections III and IV show that the RT instability has the potential to substantially alter the amount of K-shell emission from that which is expected from 1D behavior.

(5) Assuming that stabilization of imploding PRS Z-pinch loads against the RT instability is important for achieving efficient K-shell emission from large initial radius implosions, then some of the load energy might need to be sacrificed for improved stability. Otherwise, this energy could be made available for conversion into usable x rays. For example, the initial pinch radius could be made smaller than the optimal value or the current pulse could be shortened. In either case, energy is traded for better stability. In this section the 2D results of an alternative way of mitigating the RT instability, which has the potential of providing a better trade-off between stability and energy coupling, is discussed. This alternative load is one for which the initial density profile is tailored in both the axial and radial directions. This load is suited for producing regions of plasma that have high specific energy. An obvious DSWA application is high-Z K-shell loads.

(6) Last year the transmission line behavior - including convolute losses - and argon K-shell emission potential of the "baseline" DECADE QUAD design were described. This year a more "aggressive" DECADE QUAD design was analyzed. The aggressive design is basically the same as the baseline design except there is no oil transmission line and the vacuum gaps are reduced. These alterations lower the inductance of the baseline design. The more aggressive design is better than the baseline design from the standpoint that experiments do not have to be performed at as large a radius to achieve the radiation goals of DSWA's PRS program. Reduced implosion symmetry and the RT instability are the two major reasons for the possibility of uncertainty in our knowledge of the implosion behavior of large initial radius loads. This section also discusses the idea of twisting the return current cage to reduce the RT instability.

(7) Since the present route to achieving significant K-shell emission from high-Z loads requires that

bigger drivers, i.e. Z, DECADE, and X1 be built, it is important that loads and machines be designed to properly utilize this energy. In this regard, there has always been some speculation that it might be more efficient to take the Inertial Confinement Fusion approach and devise schemes and design loads that heat an already compressed plasma. One such scheme has been proposed by Rudakov, et. al. and is referred to as a "Line Converter" scheme (Rudakov, L.L .et. al., Proceedings of the 4^{th} International Conference on Z-Pinches, Vancouver (1997)). This scheme, which is analyzed in this section, involves producing and heating a plasma to very hot temperatures with minimal radiation losses with a conventional z pinch and then transferring via thermal conduction the thermal energy of the z-pinch plasma to a high density K-shell emitting converter layer.

(8) Modeling the energy coupling of large radius DECADE and DECADE QUAD loads is going to entail 2-D and possibly 3-D calculations. In order to perform these computationally expensive calculations it may be necessary to change our algorithms to accommodate parallel computer architectures. In addition, it will also be necessary to make educated decisions about how to minimize the computational overhead while still maintaining the integrity of the calculation. In this regard knowledge of the degree of sophistication required in the ionization dynamics and radiation transport routines to effectively model the given DECADE problem is imperative. This section addresses the issue by assessing the uniqueness and sensitivity of the calculated emission spectrum to variations in the radiation models.

I. SATURN MIXTURE EXPERIMENTS: A NEW SPECTROSCOPIC METHOD FOR OBTAINING THE TEMPERATURE PROFILE

A. SUMMARY OF EXPERIMENTS AND RESULTS

X-ray spectral analysis is often the readily accessible method of choice for inferring conditions in Z-pinch plasmas [1]-[17]. Reliable diagnosis of the temperature and density profiles of these plasmas is needed to address several fundamental questions about the relationship of the x-ray emission capabilities to the pulsed-power generator, load design, Z-pinch implosion dynamics and on-axis assembly conditions. For instance, how does the magnitude and risetime of the current affect x-ray performance and how does the radius and spatial profile of the initial mass load affect emission during load assembly?

One aspect of the load radiation physics which will be of increasing importance as Z pinch drivers are able to deliver more current is the opacity of the pinch in regions of the x-ray spectrum such as the K shell lines which are of great importance to the achieved yield. As these key lines become increasingly optically thick due to the large mass loads supportable by very high currents, absorption and subsequent conversion to softer x-rays can limit the achievable K shell yield. Fortunately, it has proven possible to avoid this problem to some degree through the use of mixtures [13]. The basic principle is: it is better for a load to radiate four alpha lines from two elements, each of which has roughly half the optical depth of the two alpha lines which would result from using a one-element load. Mixed Al:Mg loads on Double EAGLE (Physics International Corp.) showed yield enhancements of 28-50% over pure Al wire loads [13].

In December 1996, a series of experiments were mounted under DSWA auspices on the Saturn generator at Sandia National Laboratories whose purpose was to extend and demonstrate this principle on a machine with significantly higher current (7 MA vs. 4 MA) than Double EAGLE. In addition to Al:Mg wire alloy shots, Al:Mg wires coated with KCl were also imploded. KCl appeared promising for the very straightforward reason that the Cl and K atomic numbers of 17 and 19 straddle the 18 of Ar, which has produced 50 kJ of K shell radiation on Saturn.

The conditions and results of this mixture campaign on Saturn may be summarized as follows:

Manuscript approved February 12, 1998

all shots employed arrays of 30 wires, the initial diameter of the array was 24 mm, and the total mass load (all elements included) was 410 μg/cm. Peak currents were very close to 7.0 MA, and implosion times 70 ns. The highest total K shell yields were 60 kJ, obtained on shots with a 6% Mg alloy and also when the Al wires were coated with a Mg layer amounting to 20% of the total array mass. These yields exceeded by 20% those obtained when essentially pure Al wires were deployed (only 1% Mg). Therefore, the principle that mixing Al and Mg can enhance K shell yield was confirmed, even though Saturn's higher temperatures are less favorable to the relatively low atomic number, 12, of Mg.

However, the results with a KCl coating on the Al wires were inconclusive. It was possible to monitor the Cl yield separately, and, for the same nominal initial conditions, (the KCl mass was 20% of the total) the Cl yield varied from 0.6% to 13% of the total K shell emission. Note that KCl, in contrast to Mg, is a dielectric. It has been established, in the work reported in Ref. 13, that the behavior of the outer wire coat is critical to the performance of such mixed loads. We speculate that the cause of the irreproducible results with KCl coated Al wires lies in the early time behavior of this dielectric coating which establishes whether and to what extent the KCl becomes part of the pinch. A definitive answer would require more shots with special emphasis on state-of-the-art early time diagnostics. The remainder of this Section deals with the excellent data and diagnostic progress which resulted from the Al:Mg shots in this series.

B. USING AVAILABLE DATA TO CONSTRAIN PINCH CONDITIONS

Clearly, it is not always possible to obtain an optimal data set during a Z-pinch experiment. For instance, many if not all of the higher-order K-shell lines can be too weak for quantitative characterization. Sometimes, one cannot deploy both high resolution and survey spectrometers and therefore some of the lines are either unresolved or not detected. Very often, spatially resolved data is not available. Even if excellent quality, comprehensive data is obtained, the fundamental physics question remains: how uniquely does such spectroscopic data pin down the conditions in the Z-pinch? What additional procedures or data may be needed to assure that the diagnostic result is reliable and not misleading? In this report, we begin to begin to address this issue. In subsection C, the basic theoretical considerations are presented along with a description of the calculations used in our study. Subsection D applies the theory to the abovementioned experiment carried out

on the Saturn pulsed-power generator at Sandia National Laboratories in which limited but high quality spectroscopic data from a Z-pinch composed of 99% Al and 1% Mg was obtained. Our results and conclusions are summarized in E.

C. THEORETICAL CONSIDERATIONS AND CALCULATIONS

The focus of the present work is the determination of the properties of the K shell emitting region of a Z-pinch. For this analysis it is essential that the diameter of the pinch in the spectral region of the K shell emissions has been measured with a time-resolved filtered pinhole camera (as in the experiments described in Refs. [18]-[20]). As described in Refs. [1] and [18], the apparent diameter of a typical Z- pinch shrinks as one looks at increasingly harder photons, leading to a picture of a hot K-shell emitting core surrounded by a cooler, mostly L-shell emitting halo. Any halo region which is too cool to emit K shell radiation cannot be diagnosed by K shell emission spectroscopy. When temperature and density profiles are referred to in the remainder of this work, it is with respect to the K shell core of the pinch, the diameter of which is presumed known from measurement. Existing experimental and theoretical work, including pinhole images [20],[21] supports electron temperature profiles which decrease from the axis to the pinch halo, therefore, most of our assumed temperature gradients are consistent with this picture.

Consider the problem of calculating the radiation emitted from a one-dimensional (1D) cylindrical Z-pinch whose properties are a function of radius (r) only. For computational purposes, divide the plasma into N spatial cells, gradually increase N and note the theoretical spectra resulting from the successive calculations. At some point, it will become clear that no further increase in N is necessary because the spectrum converges. In practice, N's as low as 10 can be used for homogeneous plasmas, but may need to range as high as 50 or so when severe gradients are present. In the following considerations, N is assumed sufficient for an accurate spectral calculation in 1D.

The power P emitted in a K shell line from a Z pinch in the N-cell approximation is given by

$$P = \sum_{i=1}^{N} C_i f_i. \tag{1}$$

In Eq. (1), C_i is the creation rate at which population of the upper level of the transition is filled, and f_i is the fraction of such creations that result in a K shell photon being emitted from the pinch. Obviously, f_i depends on the single flight photon escape probability as well as the

probability of collisional de-excitation of the upper level (quenching). Each f_i is therefore a highly non-linear function of the density, electron, and ion temperatures of all of the N spatial cells. Even if the ion temperature is assumed known from high-resolution spectroscopic measurements of the line Doppler widths, the emitted power of each K shell line is a function of 2N variables. For the most favorable case N=10, each of the 6 or so K shell lines which are usually measured is therefore a highly nonlinear function of 20 variables, even for a plasma in collisional-radiative equilibrium. The functional forms of the dependences of collisional excitation rates and escape probabilities include terms which are exponential in temperature, and inverse square root of optical depth (i.e, density), not to mention the very complex implicit dependences of ionization fractions which determine in part the excitation rates and optical depths. Clearly, the theoretical problem of using analytic approaches to demonstrate spectroscopic uniqueness or the lack thereof is hopeless if applied to any realistic plasma. Since the number of physical variables which determine the emitted line power greatly exceeds the number of strong K shell lines, a rigorous demonstration of the possibility of a unique fit will be difficult at best. However, the more lines measured, the more likely that the plasma can be constrained to a reasonably tight range of conditions which must be satisfied to match the observed spectrum. The approach followed in the present analysis is numerical, with emphasis placed on the physical dependences which tie the properties of the pinch plasma to the character of its emitted spectrum.

The calculations of K-shell powers and line ratios were performed assuming collisional-radiative-equilibrium (CRE), i.e., a set of rate equations is solved for the steady-state populations of the atomic levels of interest. A recent study [16] employing a 1-D radiation hydrodynamics model of Z-pinch implosions has shown that this assumption is valid for the K-shell emissions of elements up to and including at least Z=22 (titanium). The processes coupling the levels and determining their populations are: radiative, three-body, and dielectronic recombination, collisional excitation and de-excitation, collisional ionization, spontaneous and induced radiative decay, and photoexcitation.

Detailed radiation transport is necessary to get accurate photoexcitation rates as well as to compute the power outputs of optically thick transitions. For Al Z-pinches produced on a superpower generator such as Saturn, the optical depths of the principal resonance lines of the K shell are typically several hundred. For additional information and references concerning the

models and methods used to compute atomic rates and to calculate the radiation transport, the reader may consult Ref. [17].

D. APPLICATION TO SATURN Al:Mg DATA

To gain insight into the issues raised above we now consider the time-resolved data obtained from the Z-pinch experiment on the Saturn accelerator at Sandia National Laboratories. Saturn is a 20 TW generator, the world's second most powerful Z-pinch driver (the Z accelerator, also at Sandia, is now the most powerful at 50 TW). Saturn and its initial radiation performance are described in Ref. [5], and more recent experiments and their interpretation are covered in Refs [18]-[21]. The present experiments consist of two shots with identical loads, an array of 30 wires, composed of an alloy of 99% Al and 1% Mg. The diameter of the array is 24 mm, each wire of diameter 25.4 μm, corresponding to a total mass load of 410 μg/cm. As was the case for the experiments described in Refs. [20] and [21], the data were well correlated, and we will treat these two shots as a single experiment, with the mean of each measured quantity from the individual shots considered to be the data that the model must match. The diagnostics deployed included time-integrating and time-resolving x-ray crystal spectrometers, filtered calorimeters and photoconducting detectors (PCD's), time-resolving and time-integrating x-ray pinhole cameras, and the usual complement of current monitors [19].

The peak load current was measured to be 6.6 MA, with an implosion time of 71 ns. The total radiation yield was 215 kJ, of which 50 kJ were from the K shells of Al and Mg. The measured times of peak power for total and K shell x-rays coincided within 2 ns. The pinch diameter in kilovolt x-rays at peak x-ray power was 3.25 mm. Placing the entire mass load uniformly within a cylinder of that diameter would produce an ion density of 1.1×10^{20} cm^{-3}.

Two additional time-resolved data points were obtained: the peak K shell power was measured as 0.7 TW/cm by a filtered PCD, and the time-resolving spectrometer recorded the ratio of Al Ly β to He β as 1.66 at the time of peak x-ray power. This line ratio is predominantly temperature-sensitive, and its time-integrated value was 1.09. This is another confirmation of the conventional wisdom that peaking of the x-ray power is in part the result of a maximum or near maximum in the pinch's electron temperature [21]. Unfortunately, no other reliable time-resolved line ratios could be obtained. The He α line was diffracted too close to the crystal edge, and the much weaker γ

lines produced noisy data. Though unfortunate in one sense, the limited nature of the available time-resolved information represents precisely the kind of practical situation where knowledge of what can be inferred from such data is most important. However, one other important piece of information was available. From time-integrated data the ratio of the sum of the α lines from Mg to the sum of those from Al is used below to delineate between two possible interpretations of the time-resolved data.

For our initial analysis of the above data set, we apply our model to calculate Al Ly β to He β line ratios and total K shell powers as a function of electron temperature profile and ion density. In each case, the diameter of the pinch is set at the observed 3.25 mm. The Al ion density ranges from 10^{18} to 10^{20} cm^{-3}, which corresponds to mass participations ranging from about 1% to 90%. The ion temperature (which affects the line opacities) is taken as a factor of 10 greater than the electron temperature, based on the line width measurements of Ref. [19]. The ratios and powers are plotted as isocontours in the temperature-density plane, which conveniently displays their functional dependences over a wide range of possible pinch conditions. In effect, this method facilitates a graphical solution, or at least some insight, into the uniqueness and self-consistency of the solution.

The present investigation considers uniform density cylindrical pinches which have a wide variety of temperature profiles. Consideration of density gradients would increase the number of needed calculations by an order of magnitude and is reserved for future work. Two basic types of (electron) temperature profile are considered: uniform temperature, and profiles in which, in accord with the previous discussion, the temperature decreases from the axis (r=0) to the outer edge of the pinch (r=R). For such decreasing temperature profiles, we assume a temperature distribution given by

$$T_e(r) = T_e(0) - [T_e(0) - T_e(R)] \left(\frac{r}{R}\right)^n \qquad (2)$$

where, in Eq. (2), n is positive but not necessarily an integer. The properties of the temperature distributions encompassed by Eq. (2) are illustrated in Fig. 1, where the axial and outer electron temperatures are taken as 1200 eV and 100 eV, respectively. For n=1, we obviously have a linear decrease of temperature from the axis to the outer edge of the pinch. When n increases above 1, the temperature remains close to its axial value for a greater fraction of the pinch volume and then sharply drops to its outer edge value. For n < 1, the electron temperature is more sharply peaked

near the axis. As discussed above, and as is evident from the fact that the L shell yield exceeds that of the K shell by a factor of 3, there is abundant cool plasma present in these pinches. For Al, plasma cooler than about 100 eV has no effect on the K shell, hence in the present investigation, the outer edge temperature is fixed at 100 eV. Diagnosis of any cooler plasma region requires detailed L shell spectroscopy. The temperature on axis is varied as a free parameter, from 400 to 2400 eV.

Initial insight into the uniqueness of fit is obtained by considering uniform pinches. Figs. 2a and 2b plot the calculated isocontours of the Al Ly β/He β ratio and K shell power, respectively, as a function of ion density and electron temperature. These and the succeeding figures include exact contours for the observed line ratio of 1.66 at the time when the K shell power peaked at 0.7 TW/cm. Note from Fig. 2a that the line ratio is mostly temperature dependent, but as the ion density increases above 10^{19} cm^{-3}, ionization from excited states and photoexcitation of those states results in some density dependence. A given value of this line ratio occurs at lower temperatures for higher ion density due to these pumping effects which become more pronounced. By contrast, Fig. 2b shows that above about 600 eV, the K shell power is mostly density dependent. Below this temperature, the rapid decrease of collisional excitation of the radiating levels has the effect of requiring higher density to obtain a given power, hence the contours sweep toward higher ion densities. Overlaying these two figures demonstrates that the mostly horizontal 1.66 ratio contour of Fig. 2a intersects the mostly vertical 0.7 power contour (Fig. 2b) at an ion density of 2.5 x 10^{19} cm^{-3} and electron temperature of 1300 eV. Therefore, given the assumption of a uniform pinch, the time-resolved pinch size, K shell power, and β line ratio determine a unique temperature and density. This also shows that these data, considered alone, are consistent with the existence of a uniform plasma. We now consider whether these data are also consistent with other temperature profiles.

Figs. 3a and 3b present the same ratio and power contours for the case n=0.5, in which the temperature is sharply peaked near the axis (see Fig. 1). In these and other figures in which non-uniform temperature profiles are considered, the core (i.e., r=0) temperature is plotted on the vertical axis. Note from Fig. 3b that the power contours are qualitatively similar to those of the uniform case shown in Fig. 2b, predominantly density dependent. However, the line ratio contours exhibit much less temperature dependence, much more density dependence, than those of the uniform case of Fig. 2a. The explanation for this phenomenon is straightforward. A large fraction

of the outer pinch is much cooler than the core, and it absorbs and reradiates the core spectrum with intensities more characteristic of the cooler regions. Thus, the ratio is quite insensitive to the core temperature. The 1.66 contour for the beta line ratio is virtually the same shape as the 0.7 contour for the K shell power, except that they are offset in such a fashion that they do not intersect. Therefore, this limited time-resolved data set is nonetheless sufficient to rule out the temperature profile of Eq. (2) with n=0.5 as the characteristic exponent. The absorption effect also results in the non-intersection of the line ratio and power contours for the cases n=1, 2, and 4. A large class of temperature profiles can therefore be ruled out by a small amount of data.

A contrasting but equally interesting result arises when considering temperature profiles with n=8. As shown in Fig. 1, this case is characterized by a relatively sharp transition near the "surface" of the pinch from the hot core plasma to the cooler halo. Since the halo region is not as extensive, absorption is less pronounced and the contours once again intersect as in the uniform case. However, as evident from the corresponding plots of Figs. 4a and 4b, the 1.66 line ratio and 0.7 power contours virtually coincide for the entire region of core temperatures from 800 to 400 eV. In the region of coincidence of the contours, the ion density correspondingly varies from 2.7 to 5.7 x 10^{19} cm^{-3}. The n=8 temperature profile necessitates a considerably lower average pinch temperature than arises from the assumption of uniform plasma. The density must be higher than derived in the uniform case in order to maintain the observed K shell power. A principal question emerging from this result is: how can such a cooler pinch produce the same Ly β/He β ratio as the 1300 eV uniform plasma?

The resolution of this apparent paradox lies in the spatial differences in self-absorption of the H-like compared to the He-like lines. In the case of the uniform, 1300 eV pinch, the populations of the H-like and He-like ground states are nearly uniform as a function of radius, constituting fractions of 0.20 and 0.06, respectively, of all the ions. Thus, the self-absorption of the 1-3 β lines is also spatially uniform. By contrast, a pinch with an electron temperature profile which decreases from 800 eV in the core to 100 eV or less in the halo, would have H-like fractions of 0.35 in the core, but only 0.05 in the cool outer zone. The corresponding He-like ground state fractions are 0.15 and 0.83 for the axis and outer surface, respectively. In this case, the Ly β emission from the hotter core passes through the cool outer region with little self-absorption, while the He β emission is dominated by absorption and re-emission in the halo. The effective radiating temperature of Ly

β is therefore much greater than that of He β, leading to a line ratio comparable to that achieved at much higher temperatures in a uniform pinch. Within the constraints of our uniform density assumption, we are left at this point with two possible solutions to the temperature profile in the Al:Mg Saturn pinch: a uniform, 1300 eV plasma or a decreasing temperature profile in which the average temperature is half or less that of the uniform pinch. The diagnosed density for the uniform temperature plasma implies that 23% of the load participated in the K shell radiation, whereas the required higher density range for the pinch with decreasing temperature profile leads to mass participations of 25-52%. Further data from the Mg emissions can, however, be brought to bear to resolve this lack of uniqueness.

Time-integrated spectra are generally less valuable than time-resolved ones because the uncertainties introduced into the diagnosed conditions by averaging in time cannot be independently assessed in the absence of time-resolution. However, such data can be used to compare shots taken under different load and/or current conditions, and time-integrated data can sometimes be very useful in the establishment of upper or lower limits. In the present Saturn Al:Mg alloy shots, the time-integrated ratio of the sum of the Mg α resonance lines (including the He intercombination line) to those of Al was measured at 0.02. The fact that the Mg radiates twice as copiously in proportion to its 1% presence in the pinch is due to its much lower opacity, and is the basis of other experiments [13] which have demonstrated yield increases using larger fractions of Mg. Figs. 5a and 5b display contours of this measured Mg to Al line ratio for the two cases of uniform and n=8 decreasing electron temperature profiles. Note from Fig. 5a that to match the measured 0.02 the uniform case requires much lower temperatures than the 1300 eV diagnosed from the time-resolved Al data. More importantly, except for temperatures below 500 eV, the density required is higher than that attained at peak power. For uniform temperatures below 500 eV, the Al Ly β/He β ratio is less than half of the measured time-integrated value of 1.09. Finally, at 1300 eV and 2.5 x 10^{19} cm^{-3} (diagnosed from the Al data assuming a uniform plasma), the calculated Mg to Al alpha line ratio is only 0.007, thus to attain a time-integrated ratio of 0.02 would require instantaneous ratios far exceeding 0.02 at some time during the pulse, which implies densities well in excess of those achieved at peak total and K shell power. A uniform pinch is thus effectively ruled out by the time-integrated Mg data. In contrast, overlaying Fig. 5b with either 4a or 4b demonstrates that the n=8 decreasing temperature profile fits the available data from both elements at a core

temperature of 700 eV and ion density of 3 x 10^{19} cm^{-3}. The much lower opacity of the lines of Mg, constituting only 1% of the pinch plasma, as well as the different temperature sensitivity of a lower atomic number element, provides the additional experimental discrimination needed to resolve the temperature profile.

E. SUMMARY AND CONCLUSIONS

The value of using spectroscopic data to diagnose Z-pinch plasmas hinges on the practical question: how tightly constrained are the properties of a pinch by a given selection of data? In the case of the K shell, the number of underlying variables determining the intensity of the lines well exceeds the number of lines which usually can be recorded accurately. Due to the highly nonlinear and nonlocal dependences of emitted line power on these variables, analytic approaches to demonstrating the requirements for acquiring a detailed and possibly unique interpretation are not promising. The present work uses a case study approach with data from a Z-pinch created on the Saturn generator at Sandia National Laboratories by imploding an array of Al:Mg alloy wires. We find that the time-resolved, but limited Al data can be fitted by either a uniform temperature profile, or one in which the temperature peaks on axis, drops slowly until near the plasma surface, and then drops sharply. The decreasing temperature profile necessitates densities up to twice as great to match the observed K shell power, meaning that up to half the load could have participated in the K shell radiation rather that just one-quarter. The principal Mg lines were responsible for 2% of the line radiation, twice the 1% proportion of this element in the alloy. Their lower opacity, thus different sensitivity to temperature gradients is responsible for the fact that only the decreasing temperature profile is able to fit both the Al and Mg data. Obviously, had there been no Mg in the pinch, this information, and the resulting ability to discriminate among temperature profiles, would not have existed. The addition of another element provided an expanded range of opacity and temperature sensitivity which in the present case enabled this selection to be made. ***The increased diagnostic information which such multielement experiments provide can only enrich our understanding of Z-pinches in the future, as well as provide enhanced yields for DSWA applications***.

REFERENCES

[1] P. Burkhalter, J. Davis, J. Rauch, W. Clark, G. Dahlbacka, and R. Schneider, "X-ray line spectra from exploded-wire arrays," *J. Appl. Phys.*, vol. 50, pp. 705-711, 1979.

[2] S. Maxon and T. Wainwright, "Radiation spectra from an imploding argon gas puff," *Phys. Fluids,* vol. 27, pp. 2535-2544, 1984.

[3] M. Gersten *et al.,* "Scaling of plasma temperature, density, size, and x-ray emission above 1 keV with array diameter and mass for aluminum imploding-wire plasmas," *Phys. Rev. A.,* vol. 33, pp. 477-484, 1986.

[4] F. C. Young, S. J. Stephanakis, and V. E. Scherrer, "Filtered x-ray diodes for imploding plasma experiments," *Rev. Sci. Instrum.,* vol. 57, pp. 2174-2176, 1986.

[5] R. B. Spielman *et al.,* "Z-pinch experiments on Saturn at 30 TW," *AIP Conf. Proc.,* vol. 195, pp. 3-16, 1989.

[6] K. G. Whitney, J. W. Thornhill, J. P. Apruzese, and J. Davis, "Basic considerations for scaling Z-pinch x-ray emission with atomic number," *J. Appl. Phys.,* vol. 67, pp. 1725-1735, 1990.

[7] M. C. Coulter, K. G. Whitney, and J. W. Thornhill, "A new procedure for analyzing x-ray spectra from laboratory plasmas," *J. Quant. Spectrosc. Radiat. Transfer,* vol. 44, pp. 443-456, 1990.

[8] C. Deeney *et al.*, "Role of the implosion kinetic energy in determining the kilovolt x-ray emission from aluminum-wire-array implosions," *Phys. Rev. A,* vol. 44, pp. 6762-6775, 1991.

[9] C. Deeney *et al.*, "Neon gas puff implosions on a high-current microsecond generator with and without a plasma opening switch," *J. Appl. Phys.,* vol. 72, pp. 1297-1305, 1992.

[10] N. Qi, D. A. Hammer, D. H. Kalantar, and K. C. Mittal, "Fluorescence in Mg IX emission at 48.340 A from Mg pinch plasmas photopumped by Al XI line radiation at 48.338 A," *Phys. Rev. A,* vol. 47, pp. 2253-2263, 1993.

[11] C. Deeney *et al.*, "Radius and current scaling of argon K-shell radiation," *J. Appl. Phys.*, vol. 75, pp. 2781-2788, 1994.

[12] M. E. Foord, Y. Maron, G. Davara, L. Gregorian, and A. Fisher, "Particle velocity distributions and ionization processes in a gas-puff Z-pinch," *Phys. Rev. Lett.*, vol. 72, pp. 3827-3830, 1994.

[13] C. Deeney *et al.*, "Increased kilo-electron-volt yields from Z-pinch plasmas by mixing elements of similar atomic numbers," *Phys. Rev. E,* vol. 51, pp. 4823-4832, 1995.

[14] K. G. Whitney *et al.*, "Optimization of x-ray emission in Z-pinch implosions: theory vs. experiment," *Phys. Plasmas,* vol. 2, pp. 2590-2596, 1995.

[15] N. R. Pereira and J. Davis, "X rays from Z-pinches on relativistic electron-beam generators," *J. Appl. Phys.*, vol. 64, pp. R1-R27, 1988.

[16] J. W. Thornhill, K. G. Whitney, J. Davis, and J. P. Apruzese, "Investigation of K-shell emission from moderate-Z, low-η (-velocity), Z-pinch implosions," *J. Appl. Phys.*, vol. 80, pp. 710-718, 1995.

[17] J. P. Apruzese, K. G. Whitney, J. Davis, and P. C. Kepple, "K-shell line ratios and powers for diagnosing cylindrical plasmas of neon, aluminum, argon, and titanium," *J. Quant. Spectrosc. Radiat. Transfer,* vol. 57, pp. 41-61, 1997.

[18] T. W. L. Sanford *et al.*, "Improved symmetry greatly increases x-ray power from wire-array Z-pinches," *Phys. Rev. Lett.*, vol. 77, pp. 5063-5066, 1996.

[19] T. W. L. Sanford *et al.*, "Dynamics of a high-power aluminum-wire array Z-pinch implosion," *Phys. Plasmas,* vol. 4, pp. 2188-2203, 1997.

[20] T. W. L. Sanford *et al.*, "Time-dependent electron temperature diagnostics for high-power, aluminum z-pinch plasmas," *Rev. Sci. Instrum.*, vol. 68, pp. 852-857, 1997.

[21] K. G. Whitney *et al.*, "Analyzing time-resolved spectroscopic data from an azimuthally symmetric, aluminum-wire array, Z-pinch implosion," *Phys. Rev. E,* vol. 56, pp. 3540-3557, 1997.

FIGURE CAPTIONS

Fig. 1. Properties of the electron temperature profiles which were assumed in attempts to fit the Saturn Al:Mg pinch data, as given by Eq. (2). The outer temperature is fixed at 100 eV, but the core (on-axis) temperature is a free parameter. For the specific case illustrated, the core temperature is is 1200 eV.

Fig. 2. In (a), calculated Al Ly β to He β line ratio contours are plotted for a uniform plasma of the measured Saturn pinch diameter 3.25 mm, as a function of ion density and electron temperature. The observed value is 1.66. In (b), contours of the K shell power are shown, the observed value being 0.7 TW/cm.

Fig. 3. As in Figs. 2, except that the temperature profile is given by Eq. (2) with n=0.5 as the exponent (see Fig. 1) , and the core electron temperature is plotted along the vertical axis.

Fig. 4. As in Figs. 3, except that the characteristic exponent describing the temperature profile is n=8.

Fig. 5. Calculated contours of the ratio of the sum of the Mg α resonance lines to those of Al, including the He-like intercombination line. The plasma is 1% Mg. In (a) the electron temperature profile is assumed uniform, in (b), the the temperature decreases with characteristic profile exponent of 8 (see Fig. 1).

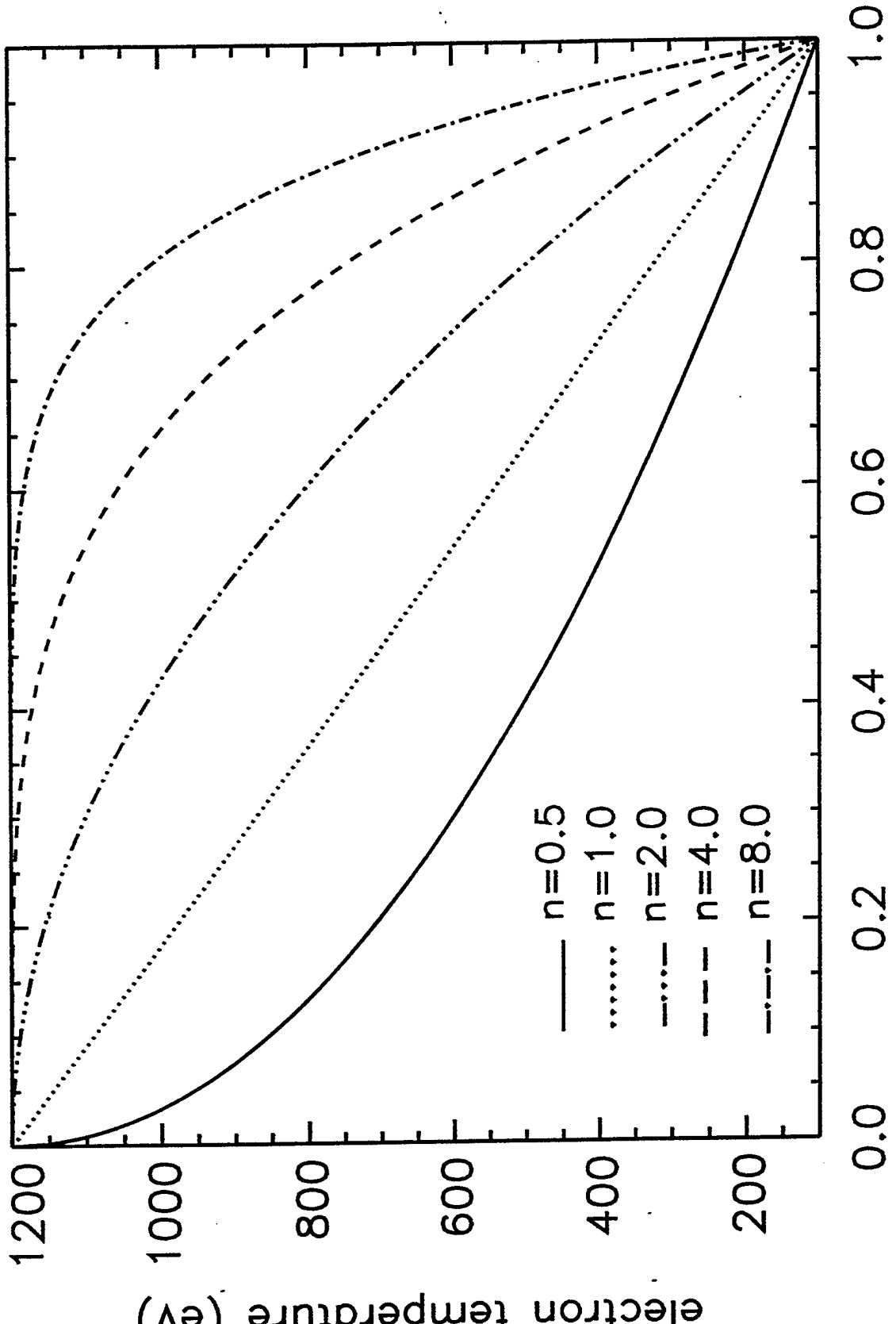
electron temperature (eV)
1200
1000
800
600
400
200
0.0
0.2
0.4
0.6
0.8
1.0
r/R
n=0.5
n=1.0
n=2.0
n=4.0
n=8.0

FIG. 1

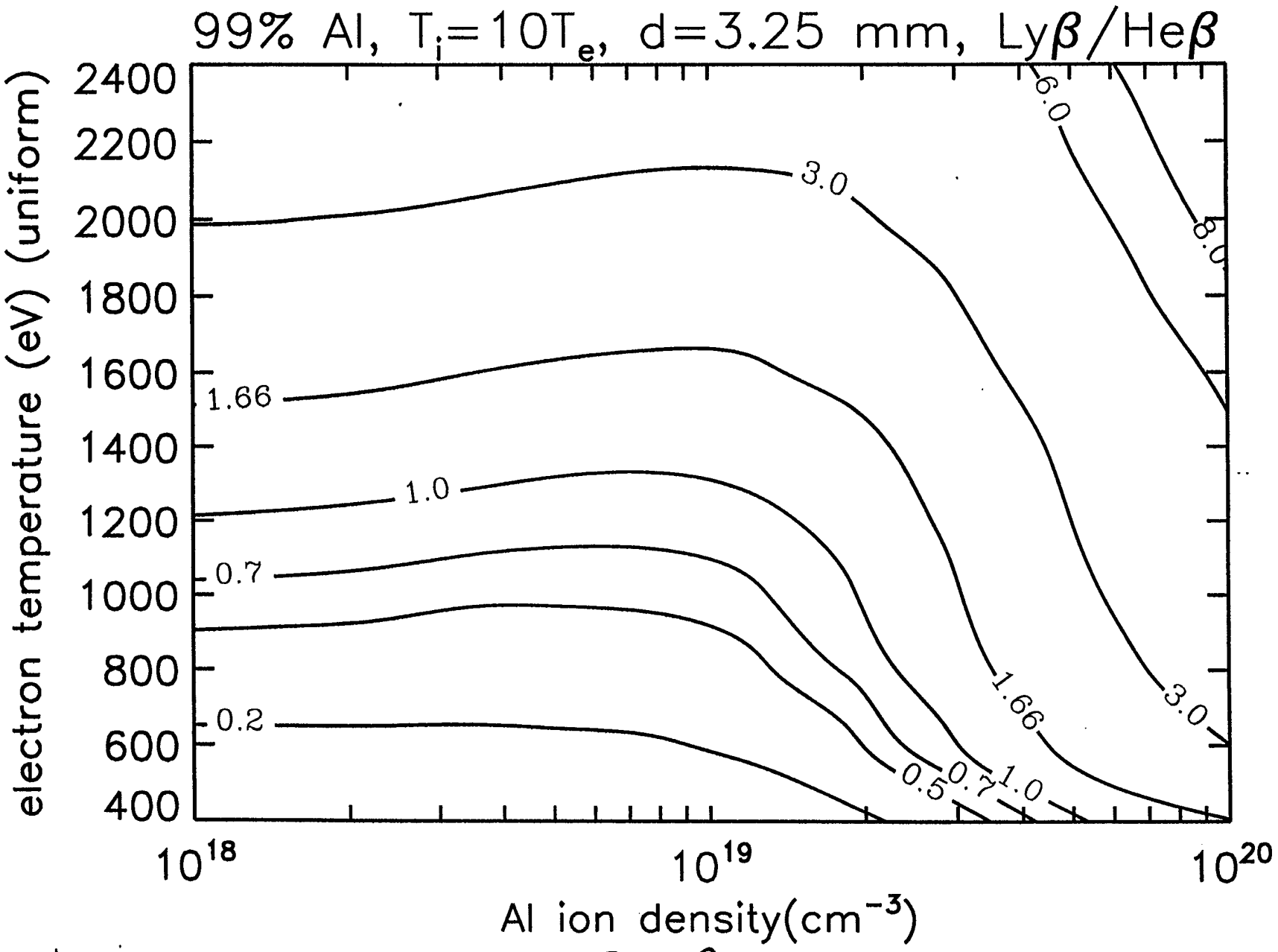
99% Al, $T_i = 10T_e$, d=3.25 mm, Lyβ/Heβ
electron temperature (eV) (uniform)
2400
2200
2000
1800
1600
1400
1200
1000
800
600
400
10^{18}
10^{19}
10^{20}
Al ion density(cm^{-3})
6.0
3.0
1.66
1.0
0.7
0.2
0.5

FIG. 2a

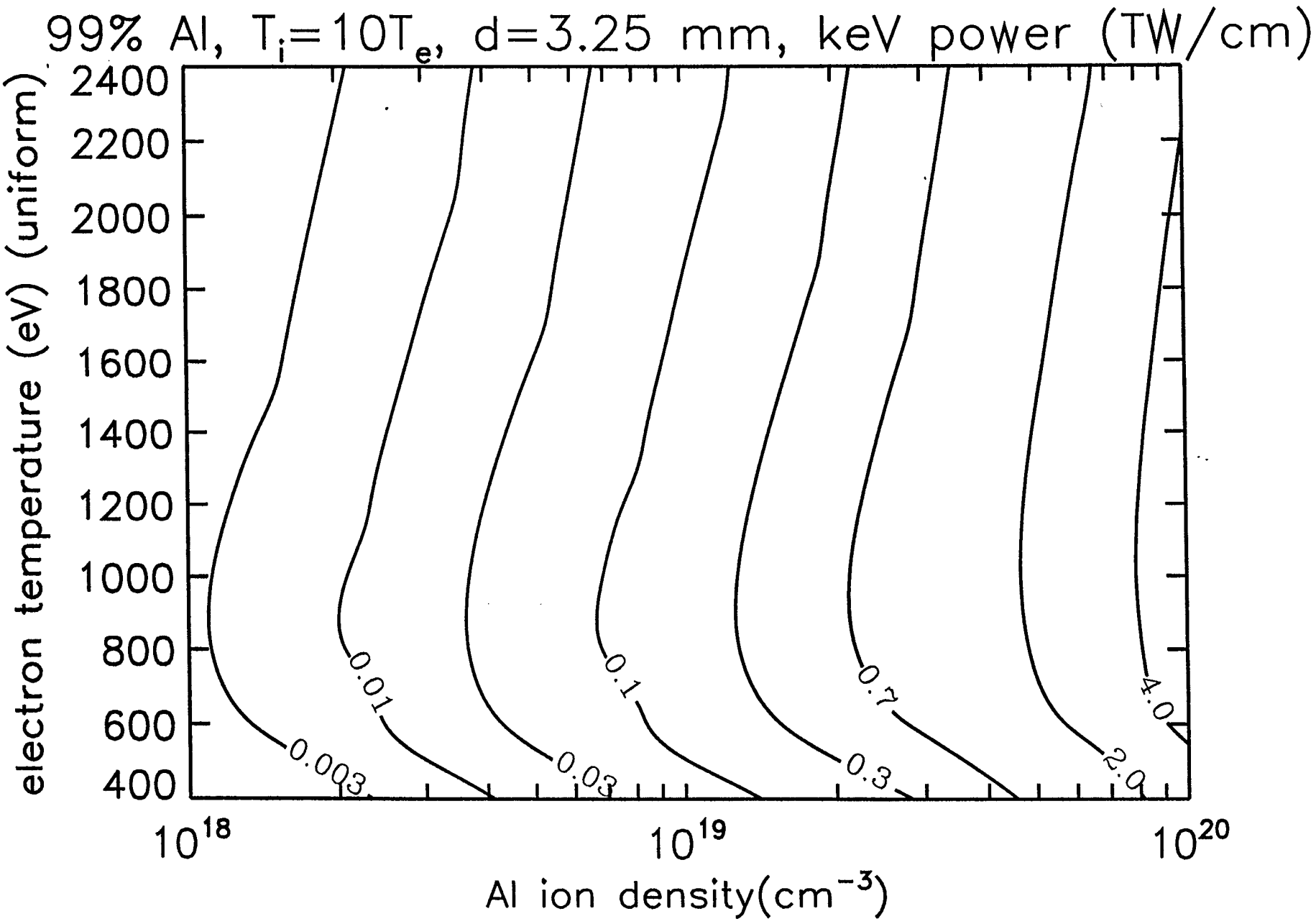
99% Al, $T_i = 10T_e$, d=3.25 mm, keV power (TW/cm)
electron temperature (eV) (uniform)
2400
2200
2000
1800
1600
1400
1200
1000
800
600
400
0.003
0.01
0.03
0.1
0.3
0.7
2.0
4.0
10^{18}
10^{19}
10^{20}
Al ion density(cm^{-3})

FIG. 2b

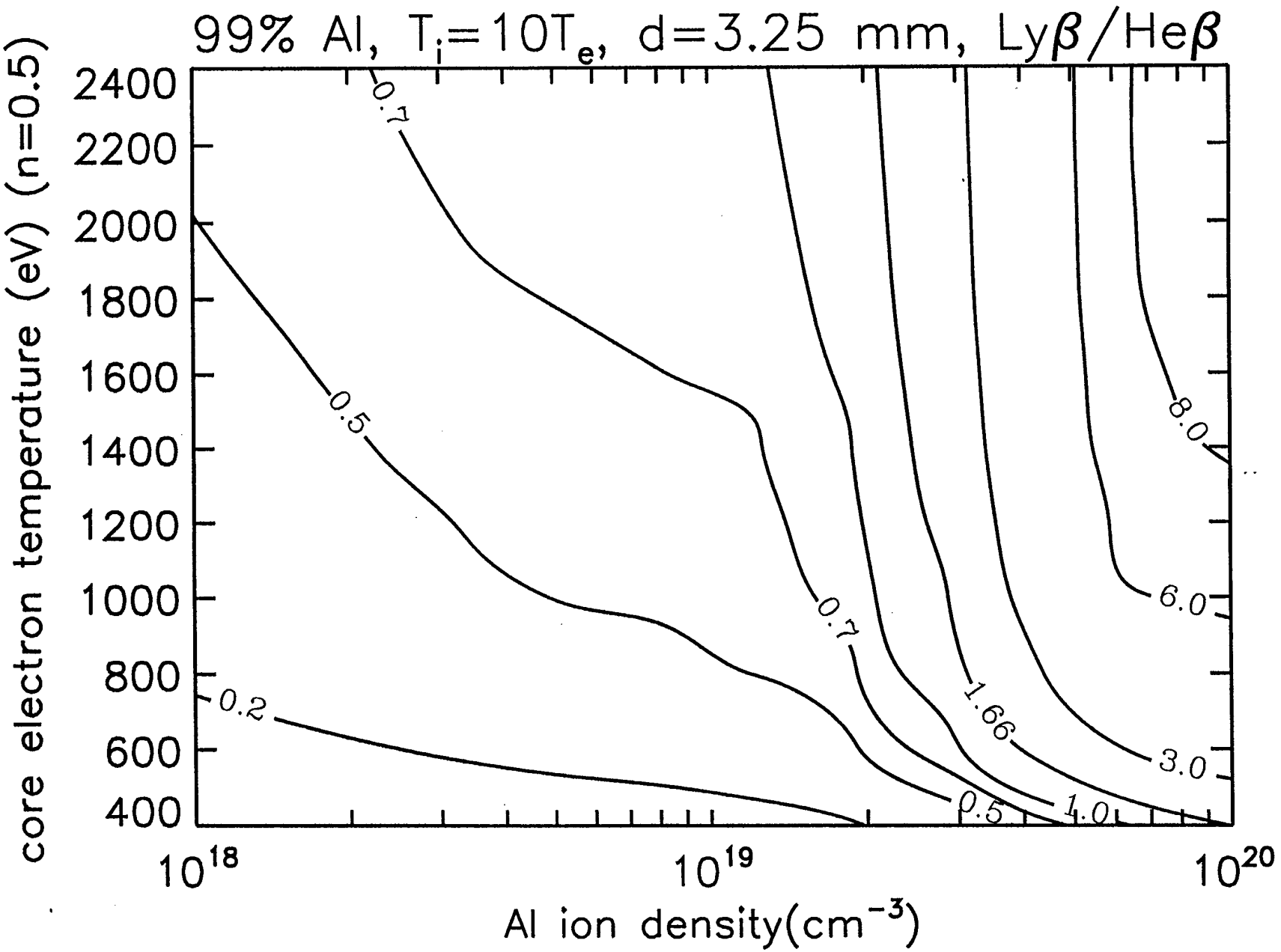
99% Al, $T_i = 10T_e$, d=3.25 mm, Lyβ/Heβ
core electron temperature (eV) (n=0.5)
2400
2200
2000
1800
1600
1400
1200
1000
800
600
400
10^{18}
10^{19}
10^{20}
Al ion density(cm^{-3})
0.1
0.5
0.7
0.2
1.66
0.5
1.0
3.0
6.0
8.0

FIG. 3a

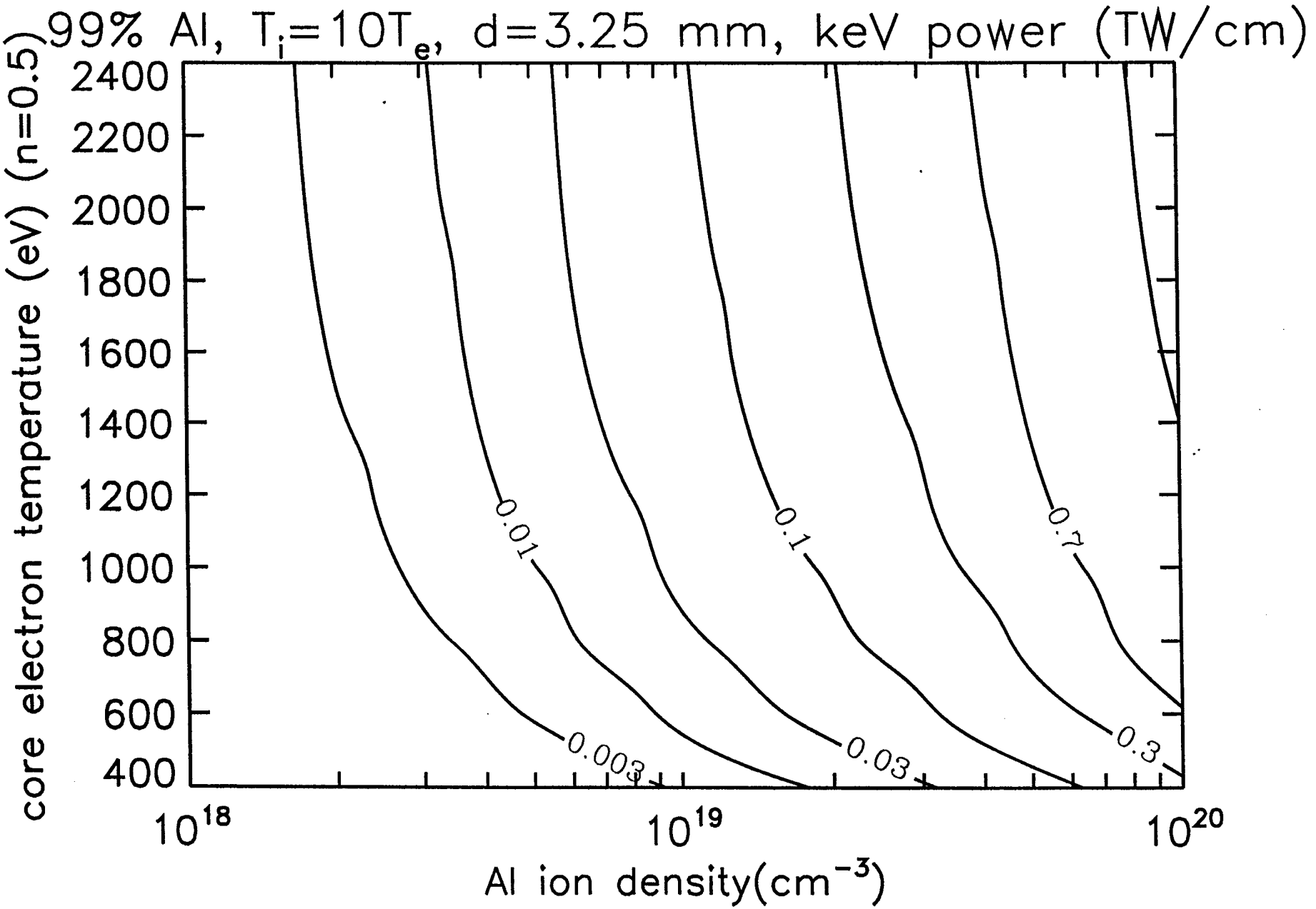
99% Al, $T_i = 10T_e$, d=3.25 mm, keV power (TW/cm)
core electron temperature (eV) (n=0.5)
2400
2200
2000
1800
1600
1400
1200
1000
800
600
400
0.01
0.1
0.7
0.003
0.03
0.3
10^{18}
10^{19}
10^{20}
Al ion density(cm^{-3})

FIG. 3b

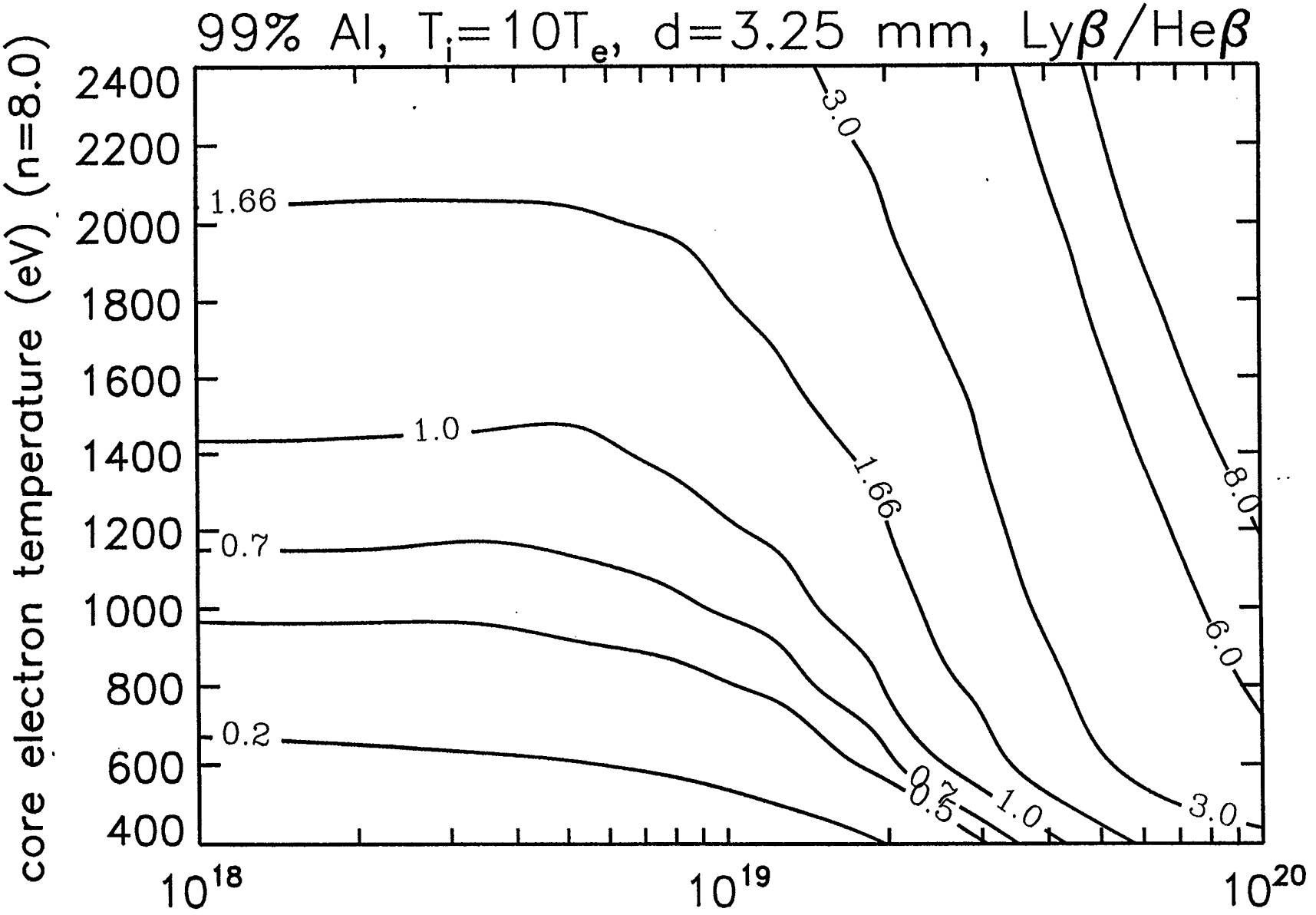
99% Al, $T_i = 10T_e$, d=3.25 mm, Lyβ/Heβ
core electron temperature (eV) (n=8.0)
2400
2200
2000
1800
1600
1400
1200
1000
800
600
400
10^{18}
10^{19}
10^{20}
Al ion density(cm^{-3})
1.66
1.0
0.7
0.2
3.0
1.66
1.0
0.7
0.5
8.0
6.0
3.0

FIG. 4a

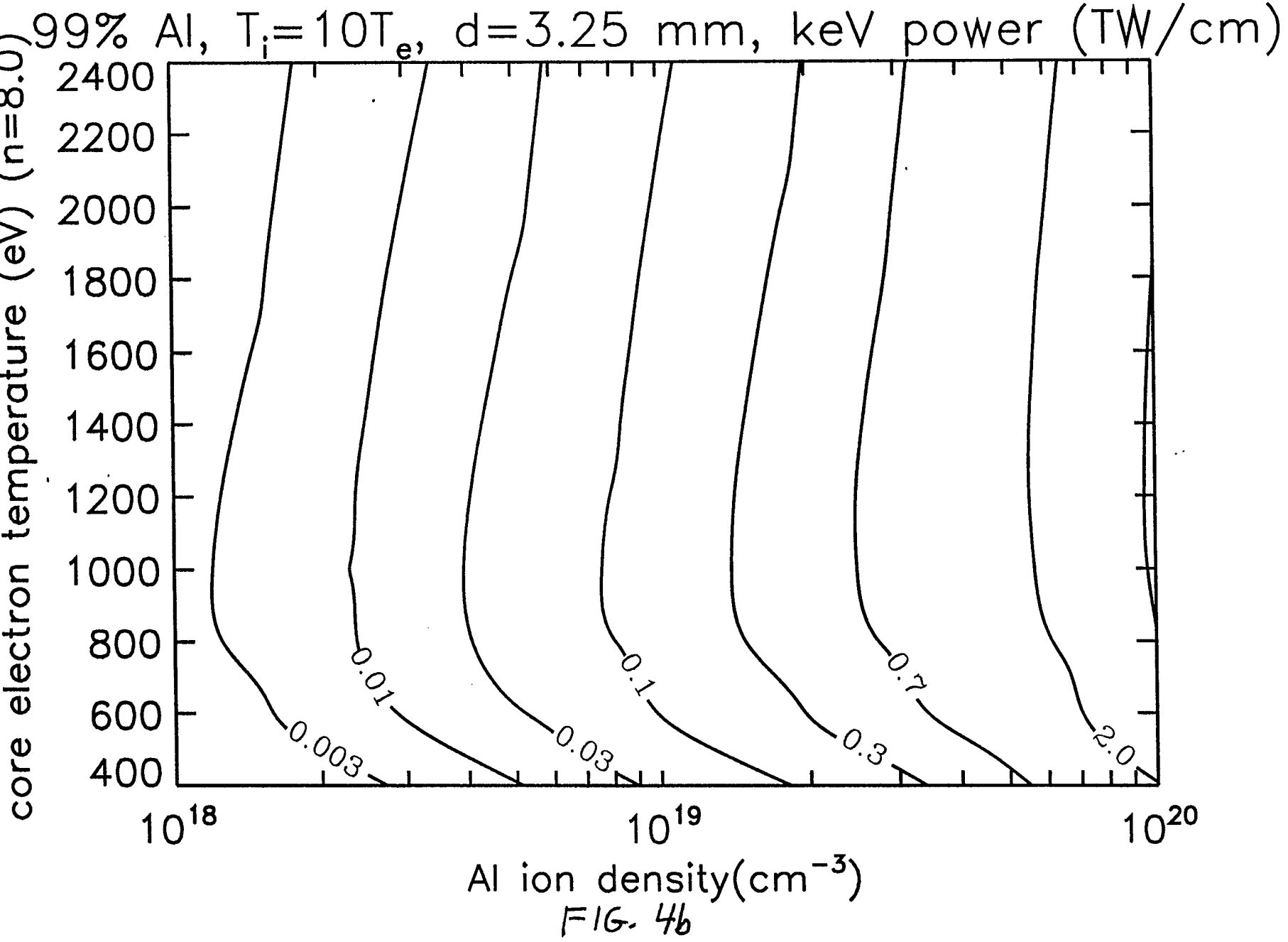
99% Al, $T_i = 10T_e$, d=3.25 mm, keV power (TW/cm)
core electron temperature (eV) (n=8.0)
2400
2200
2000
1800
1600
1400
1200
1000
800
600
400
0.003
0.01
0.03
0.1
0.3
0.7
2.0
10^{18}
10^{19}
10^{20}
Al ion density(cm^{-3})

FIG. 4b

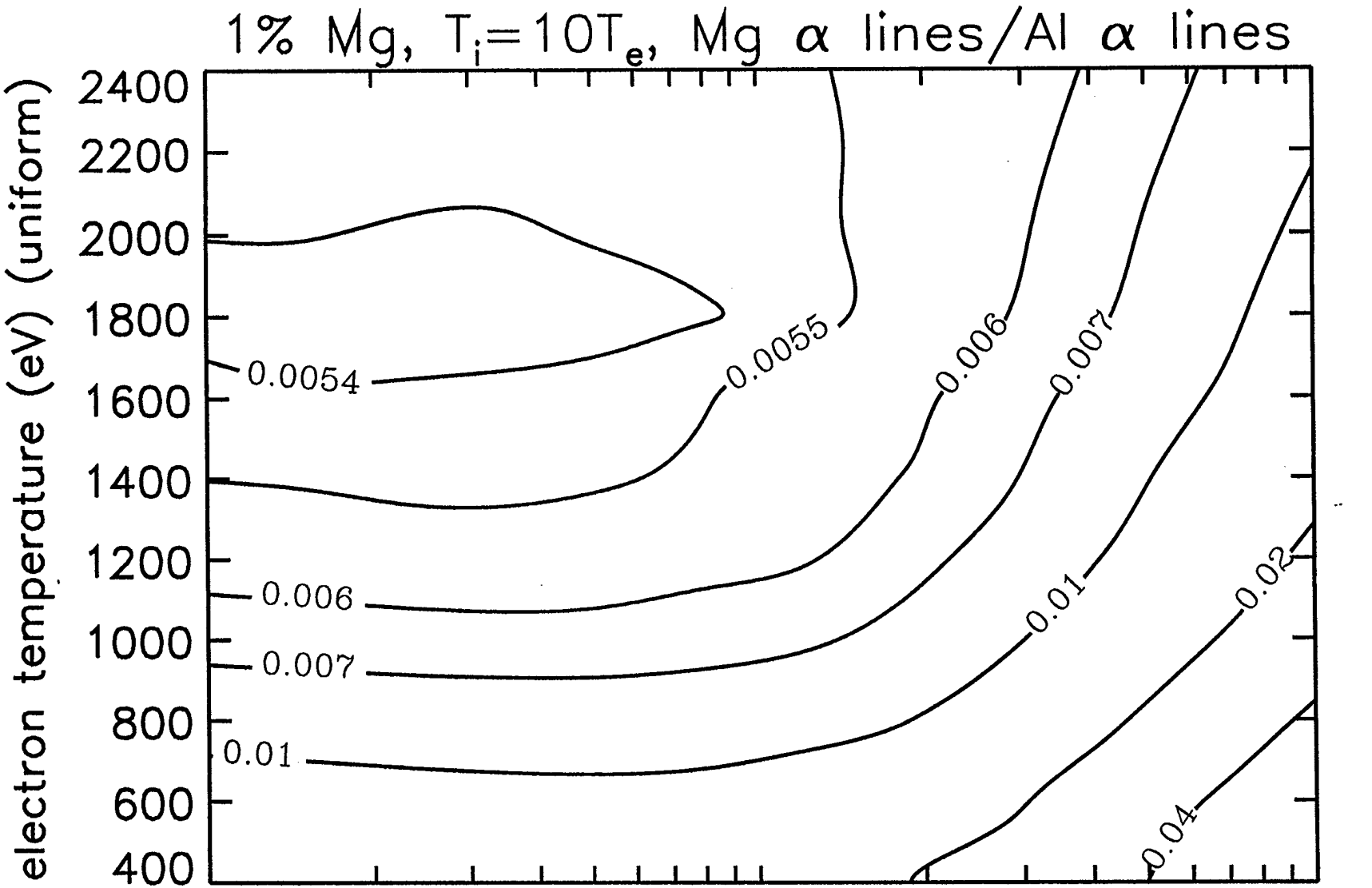
1% Mg, $T_i = 10T_e$, Mg α lines/Al α lines
electron temperature (eV) (uniform)
2400
2200
2000
1800
1600
1400
1200
1000
800
600
400
0.0054
0.0055
0.006
0.007
0.01
0.02
0.04
0.006
0.007
0.01
10^{18}
10^{19}
10^{20}
aluminum ion density(cm^{-3})

FIG. 5a

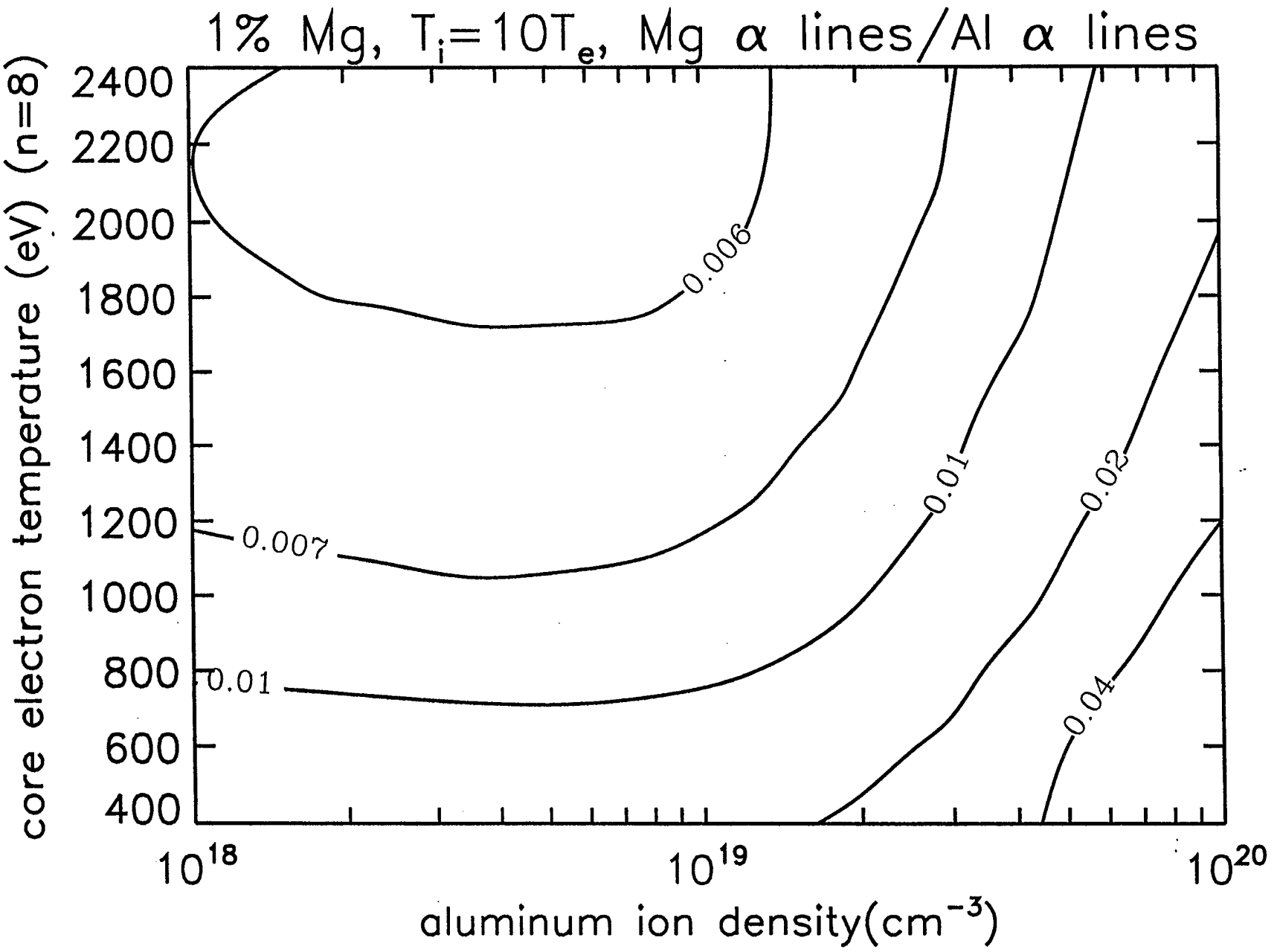
1% Mg, $T_i = 10T_e$, Mg α lines/Al α lines
core electron temperature (eV) (n=8)
2400
2200
2000
1800
1600
1400
1200
1000
800
600
400
0.006
0.007
0.01
0.01
0.02
0.04
10^{18}
10^{19}
10^{20}
aluminum ion density(cm^{-3})

FIG. 5b

II. DETERMINING THE ROLE OF TEMPERATURE AND DENSITY GRADIENTS IN PRS K-SHELL YIELD PERFORMANCE

A. Introduction

The problem of determining the effect of temperature and density gradients on z-pinch x-ray performance has only recently begun to be addressed and evaluated. For low atomic number elements, like aluminum, these gradients can negatively impact K-shell yields by reducing the amount of array mass participating in this emission. For higher atomic number loads, such as titanium, these gradients can have a positive impact by creating the high temperature inner core regions of the pinch that are necessary to achieve ionization into the titanium K-shell and 4-5 keV, high energy photon emission.

The issue of gradients arises when experimental spectral data is analyzed or when any serious attempt is made to compare calculated x-ray output with measured output. It was first noted, for example, that 1-dimensional radiative magnetohydrodynamic (1-D RMHD) calculations produced higher densities, sharper temperature and density gradients, higher x-ray powers, and tighter pinches than were being observed experimentally. These observations were made in the analysis of aluminum wire array and argon gas puff z-pinch data.[1,2] The calculations employed only the perpendicular components of Braginskii transport coefficients.[3] In them, however, one could obtain much better agreement between calculated and measured x-ray output by an ad hoc increase in the size of the three coefficients of heat conductivity, electrical resistivity, and viscosity.

The analyses in Refs. 1 and 2 were performed using three pieces of time-integrated, K-shell, x-ray data: the pinhole pictures, the K-series spectra, and total yields, in conjunction with the time-resolved K-shell pulsewidths. From these data, average power outputs, electron temperatures, and ion densities of the K-shell emission region were inferred. The introduction of three adjustable multipliers of the transport coefficients was motivated by the desire to find better phenomenological fits to these three experimentally determined quantities.

Recently, a more detailed 1-D RMHD data analysis was carried out[4] using time-resolved x-ray data obtained from three 90-wire aluminum-array shots on the Saturn generator at Sandia National Laboratories. By combining the data from three reproducible shots into one dataset, an extensive set of time-resolved x-ray data was obtained that spanned a significant portion of the history of the plasma prior to assembly and during its confinement on axis. In the 1-D RMHD analysis of the data, it was again found that adjustments to the coefficients of heat conductivity and viscosity were needed in order to achieve the best temperature and density gradients that gave the best data matchup. In this analysis, the extensiveness of the data allowed a small amount of contouring of the multiplicative factors to be carried out unambiguously in order to improve upon the agreement between the calculated and measured data.

The physical justification for modifying the coefficients of heat conductivity, electrical resistivity, and viscosity in 1-D code calculations is that they do not otherwise account for some of the multi-dimensional effects of fluid turbulence. However, before such modifications can be attributed entirely to turbulence, one must be certain that the non-turbulent description of transport phenomena in a plasma is complete and adequately accounted for. For this reason,

we have investigated some of the effects that the lambda component (with coefficient β_Λ) of the electrical conductivity has in determining the temperature gradients and current distribution within a 1-D modeled, z-pinch implosion, especially of the kind that are expected to be generated in DECADE or DECADE-quad. The lambda components of heat and electrical conductivity are commonly neglected in calculations where less than 5 MA of current are driven through a z-pinch load. In general, however, they produce sizable effects in surface and interior regions of a pinch whenever mega-ampere currents are flowing. We found, for example, for Saturn- and PBFAZ-sized load currents ($\sim$ 7 to 8 MA for Saturn and $\sim$ 16 to 17 MA for PBFAZ), that magnetic fields are sufficiently large for temperature-gradient induced currents to make significant nonlinear contributions to the diffusion of magnetic field into the plasma and to the determination of current and axial electric field distributions.

While the coefficients of heat and electrical conductivity depend on both the strength of the magnetic field and on the degree of plasma ionization, Z, (and thus on electron temperature) only the magnetic field dependence is given by formula in the literature. The Z dependence of these coefficients must be interpolated from data presented in tables.[3,5] This procedure is often inconvenient or potentially less accurate than working with a formula. Consequently, reasonably accurate formulas for these coefficients were derived this year that contain both dependences on an equal footing. With the aid of these formulas, the effect of the temperature-gradient-induced current on magnetic field diffusion in a 1-D RMHD code calculation was investigated. The distribution of current within the plasma and the severity of the temperature gradients were both found to be modified significantly by the inclusion of the β_Λ conductivity term, and increasingly so as the load current increases.

In this section, we will first describe an analysis of some Saturn data that was obtained in two sets of aluminum experiments in which the array mass and radius were held fixed and the array wire number was varied. Important trends were observed in the K-shell yield and power behavior in these experiments as a function of the initial spacing between wires. The analysis established correlations between this behavior and the plasma conditions that were generated at stagnation and assembly of the plasma on axis. We show that these correlations can be meaningfully interpreted in terms of the temperature gradients that are generated during stagnation. The discussion then shifts to two sets of calculations that were performed to evaluate the role of the β_Λ electrical conductivity in determining the temperature and density gradients that are generated on axis in both Saturn- and PBFAZ-sized implosions.

B. Fixed Mass, Variable Wire Number Experiments

Two sets of aluminum array experiments were carried out on the Saturn generator at Sandia National Laboratories two years ago. In one set, the initial array radius was fixed at 8.6 mm and the gap spacing between wires was varied by changing the number of wires in the array and simultaneously adjusting the size of the wires so as to maintain a fixed mass loading of approximately 615 μg. In the other set, the initial radius was fixed at 12 mm and gap spacing was varied for a fixed mass loading of 820 μg. The arrays were 2 cm in length. Because the gap spacing between wires and the wire size both decrease as a function of increased wire number in these experiments, they were expected to provide a first look at how K-shell yields are affected by the reduction in current per wire and/or by the difference in wire explosion and coalescence dynamics that accompanies the reduction in wire size and spacing.

The most dramatic behavior observed in these experiments was the x-ray pulse sharpening that took place as a function of reduced wire gap spacing. These sharpenings produced a corresponding increase in the peak x-ray power output, which is shown in Fig. (2.1). Two features of this power behavior are notable. One, both the 8.6 and 12 mm radius experiments exhibited the same power output as a function of gap spacing, i.e., this functional dependence was independent of the initial array radius. Two, a marked, and well pronounced, change in the rate of power increase occurred at a gap spacing of approximately 1.4 mm. This change has been interpreted as due to a change in the character of the implosion from one of discrete, individual, wire plasmas (which cannot be modeled) to one of a continous plasma shell[6] (which can be approximately modeled). In other words, the way the PRS discharge was initiated, and the way the wires exploded and coelesced, played an important role in the subsequent implosion and plasma assembly dynamics. As is indicated in Fig. (2.2), the increase in power output and decrease in x-ray pulsewidths were accompanied by a corresponding decrease in the observed size of the K-shell emission region. One needs to correlate these directly observable changes with changes occurring in the plasma properties, which cannot be observed directly.

In general, energetic z-pinch implosions, capable of generating tens or hundreds of kilojoules of kilovolt x rays, generate sharp gradients in temperature and density on axis. Progress was recently made[4,7] in inferring the magnitude and shape of these gradients from a complete-analysis of the time-resolved x-ray data taken in one of the 8.6 mm radius experiments (a 90-wire shot). However, for this shot, a uniquely large amount of time-resolved pinhole and spectrum data was taken and available for analysis. Similar datasets do not exist for the other shots in the variable wire number experiments. Thus, only a less extensive data analysis is possible for the full set of experiments, and only the space and time averaged plasma conditions for K-shell emission, which can be inferred from the time-integrated data, are discussed here.

The procedures described in two papers[8,9] were used to carry out the analysis. Table 2.1 contains its results. Two sets of average temperatures and densities for K-shell emission were inferred from the time-integrated pinhole pictures and spectra, the K-shell yields, and the pulsewidths of the main x-ray emission peaks. One set came from an analysis of the Lyman-α and He-α lines and the other from an analysis of the Lyman-β and He-β lines. The large differences between these two sets of numbers provide an indication of the large size of the temperature and density gradients that existed in the emission region, and these differences depend on plasma opacity as well. The average of the two sets of densities and temperatures are plotted in Figs. (2.3) and (4), respectively, as a function of wire gap spacing.

The rise in ion density with decreased gap spacing seen in Fig. (2.3) correlates well with the rise in x-ray power seen in Fig. (2.1) and the fall in the size of the emission region seen in Fig. (2.2). Since the size and average density of the emission region are known, one can combine these two pieces of information to obtain the average mass of this region. The ratio of this mass to the initial array mass, called the K-shell mass participation fraction, is plotted in Fig. (2.5). Note, the data analysis shows a trend toward slightly increased K-shell mass participation with decreased gap spacing. On the the other hand, the average temperatures at which the K-shell emission occurs (Fig. (2.4)) show no significant change with decreasing gap spacing below spacings of 2 to 3 mm. Thus, a picture emerges from this data analysis and from these three figures of a roughly fixed amount of plasma mass, radiating at a roughly fixed average temperature, being compressed to higher and higher densities as the wire number is increased and the initial wire size and wire spacing

is decreased, i.e., the dramatic rise in power output seen in Fig. (2.1) is primarily due to increased plasma compression.

The rise in temperature with increasing gap spacing beyond spacings of 3 mm, also seen in Fig. (2.4), can be interpreted as a manifestation of the density and temperature gradients that are present in the emission region (which the data analysis is not designed to pick out directly). If one considers a fixed mass cylinder of plasma (as suggested by Fig. (2.5)) with a cool front surface, a hot core, and a gradient in temperature connecting the two regions, and if one begins at a radius for which the cylinder is optically thin to K-shell emission, then emissions from the cylinder, in this situation, will come from all regions of the plasma, hot and cold. As one compresses the cylinder and line opacities are increased, the cylinder will become increasingly optically thick. In this situation, line emissions from the hotter core region will be absorbed and reemitted in the cooler outer regions of the plasma. Line ratios of the x-ray emission in this case will reflect a lower average temperature than in the optically thin case, which averages together emissions from both hot and cold regions. This interpretation of the temperature behavior shown in Fig. (2.4) is consistent with similar temporal temperature behavior that was inferred from the analysis of the 90-wire shot. In this case, the rise in temperature took place in time, as the radiating mass of plasma expanded and its opacity declined following peak compression.

Because the rise in K-shell power output with decreasing gap spacing is accompanied by a corresponding fall in the K-shell pulsewidth, the yield, which roughly depends on the product of these two quantities, varies much less dramatically with gap spacing than does the power. However, the yield is also determined by the impact of the x-ray loss rate on the plasma dynamics; namely, when the power output is high, the x-ray pulse has a well-defined main peak, followed by a much smaller secondary peak. At lower powers, the pinch is less well defined, the plasma bounce becomes undiscernible, and the two power peaks tend to merge into one broader, and less sharply defined, pulse. Thus, when plotted as a function of gap spacing (Fig. (2.6)), the K-shell yield appears to have a peak value in the vicinity of a 3 mm gap spacing, i.e., at the spacing where the inferred average temperatures begin to rise with gap spacing and the plasma opacity no longer completely hides the hot core. Slug model calculations predict kinetic energy inputs of roughly 280 kJ and 350 kJ for the 8.6 mm and 12 mm arrays respectively. Thus, the yield curve for the larger diameter arrays, which receives more input energy and can radiate more, lies above that of the smaller diameter arrays.

C. Magnetic Field Diffusion

The above data analysis is suggestive, but it is based on the assumption of a uniform plasma in collisional-radiative equilibrium. Nevertheless, its application has indicated the presence of gradients in the plasma, and these need to be properly calculated to better understand and interpret the data. These gradients depend on the strength of the transport coefficients used in hydrodynamic calculations, which, in turn, depend on the the degree of plasma ionization and on the strength of the magnetic field. The ionization dependence of transport coefficients is important in any description of a z-pinch's implosion dynamics since substantial ionization occurs during the course of the implosion. The tensor character of the electrical conductivity implies that axial currents are generated by radial temperature gradients in the presence of a z-pinch's magnetic field. These currents make contributions to the full current distribution that are comparable to the electric field generated currents. The effect of these temperature gradients on the full current distribution in

a 1-D z-pinch implosion should be calculated by using formulas for the electrical resistivity that contain both the magnetic field and charge state dependence of the resistivity coefficient.

To evaluate the effect of temperature gradients on magnetic field diffusion, we modeled an implosion similar to the one that was found (in an analysis of time-resolved x-ray data) to give a good representation of the temperature gradients generated in a 90-wire, aluminum shot on the Saturn generator at the Sandia National Laboratories.[4] Calculations showed that, on axis, gradient-driven currents limit total current flow near the front surface of the plasma, causing a much larger current to flow in the plasma interior than otherwise and reducing the temperature gradients that would be calculated in their absence. The gradient structure of the plasma is also changed because the modified current distribution produces a different set of $\mathbf{j} \times \mathbf{B}$ forces, which act on the plasma. These nonlinear magnetic field effects persist after peak compression during the plasma's expansion from the axis.

In the presence of a magnetic field, radial heat conduction can be driven by axial electrical currents and these axial currents can be driven by radial gradients in the temperature:

$$q_{er} = -\kappa_{\perp}\frac{n_e k T_e \tau_e}{m}\frac{\partial k T_e}{\partial r} - \beta_{\Lambda}\frac{k T_e}{e} j_z.$$

$$j_z = \frac{n_e e^2 \tau_e}{m \alpha_{\perp}}\left(E_z + \frac{v_f}{c}B - \beta_{\Lambda}\frac{k}{e}\frac{\partial T_e}{\partial r}\right),$$

When both $\alpha_{\perp}$ and β_{Λ} current terms are taken into account, the diffusion of azimuthal magnetic field into the plasma is described by the equation,

$$\frac{\partial B}{\partial t} + \frac{\partial (v_f B)}{\partial r} - \frac{\partial}{\partial r}\left\{\frac{\nu_m(n_e, T_e, B)}{r}\frac{\partial (rB)}{\partial r}\right\} = \frac{kc}{e}\frac{\partial}{\partial r}\left\{\beta_{\Lambda}(n_e, T_e, B)\frac{\partial T_e}{\partial r}\right\},$$

where $\nu_m(n_e, T_e, B) \equiv mc^2\alpha_{\perp}(n_e, T_e, B)/(4\pi n_e e^2 \tau_e)$ is the magnetic field diffusion coefficient and v_f is the radially directed fluid velocity. The solution to this equation yields the total current distribution by Ampere's law: $j_z = (c/4\pi)(1/r)\partial_r(rB)$. The influence of temperature gradients on the current distribution are manifested as a magnetic field source term.

D. Two RMHD Examples

To investigate the influence of the β_{Λ} conductivity on a z-pinch's implosion dynamics, we compare two RMHD calculations of a 1-D z-pinch implosion, one done without ($\beta_{\Lambda} = 0$) and the other with ($\beta_{\Lambda} \neq 0$) the magnetic field source term. In addition, we make this comparison for both DECADE-quad-sized and DECADE-sized generators using Saturn and PBFAZ circuit models. The main difference between the DECADE and Sandia machines is in their current risetimes, but risetime is not an issue here in the comparisons we make. The comparisons given in this section pertain mainly to how the effects of the β_{Λ} term will scale with current strength. Since changes in the current density change the $\mathbf{j} \times \mathbf{B}$ forces acting on the plasma, which, in turn, alter the temperature gradients, the influence of one on the other is mutual and must be calculated self-consistently. As mentioned above, in order to better evaluate the significance of the action of the current distribution and temperature gradients on one another, we chose a calculation similar to

one described in the literature[4] that relates closely to an actual z-pinch experiment. The temperature and density gradients that were generated in this calculation produced an x-ray output that gave a reasonable, though still imperfect, matchup with the experimental data from a 90-wire aluminum array implosion on the Saturn generator.

The calculations begin with a specified density profile, $\rho(r)$, designed to model some of the plasma features that the initial explosion of the 90 wires was expected to generate (Fig. (2.7)). Thus, as illustrated in Figs. (2.7) and (2.8), the bulk of the mass was concentrated around the initial wire array radius. Fig. (2.8) contains a plot of the mass/cm, m, contained within the radius r, $m(r) \equiv 2\pi \int_0^r dr' r' \rho(r')$, normalized to the total mass/cm, m_{total}, of the array, $m_{total} \equiv 2\pi \int_0^R dr' r' \rho(r')$, which, for the Saturn implosion, was equal to 308 μg/cm. Fig. (2.8) demonstrates that slightly more than 60% of the total mass is initially located in the outer shell of high density plasma shown in Fig. (2.7). There is a region of density falloff between points **A** and **B** in these figures, which contains slightly less than 20% of the mass. The remaining mass is distributed uniformly to the axis and represents, in a theoretically ideal way, a precursor plasma, whose presence has been detected, though not yet carefully measured, in z-pinch experiments.[4,10-12] A similar mass distribution (Fig. (2.9)) was used for the PBFAZ calculations; however, in this case, the imploded aluminum mass was 2.1 mg/cm and the initial radius for the shell mass was $\sim$ 19 mm. As in the Saturn calculations, two points, **A** and **B**, on either side of the density discontinuity are tracked in the calculations.

For each of the four calculations, the density profiles of Fig. (2.7) and (2.9) were broken into 100 roughly equally spaced zones and imploded using the Saturn or PBFAZ circuit equations. To reduce the computer time of the calculations, radiation losses were computed as if the plasmas were optically thin; however, the plasma emissivity was reduced by a factor of ten to compensate for the otherwise overly increased emission rates that are calculated when plasma opacity is ignored. In all other respects, the four calculations were similar to the one described in Ref. 4. However, because of the greater resolution used in these calculations (100 as opposed to 30 zones), tighter pinches were calculated than in Ref. 4 (which is in accord with experimental observations). Major differences in the trajectories of the zone boundaries were essentially undiscernable in each of the two sets of calculations, in which $\beta_\Lambda = 0$ and $\beta_\Lambda \neq 0$. A plot of the positions of these boundaries as a function of time in the 100 zone Saturn calculations is shown in Fig. (2.10). Peak compression occurs at approximately 81.7 ns, at which time the pinch diameter is less than 0.6 mm.

While the trajectories for implosion in which $\beta_\Lambda = 0$ closely followed those of the $\beta_\Lambda \neq 0$ implosion, differences in their temperature and density profiles are already present prior to plasma stagnation on axis. We illustrate this point in Figs. (2.11)-(2.14), which contain plots of these profiles at the six times that are indicated in Fig. (2.10) by six vertical dashes at the times, 74.3, 75.0, 75.75, 76.5, 77.2, and 77.9 ns. Figs. (2.11) and (2.13) pertain to the Saturn calculation for which $\beta_\Lambda = 0$ and Figs. (2.12) and (2.14) to the Saturn calculation in which $\beta_\Lambda \neq 0$. In both cases (Figs. (2.11) and (2.12)), the plasma shell implodes onto a low density plasma (Fig. (2.7)) creating a shock front ahead of the shell, which dissipates in time. The peak density of the shell is slightly larger when $\beta_\Lambda = 0$. During the same period of time, a heat front propagates ahead of the shock (Figs. (2.13) and (2.14)); however, when $\beta_\Lambda \neq 0$, the peak temperature, which lies inside the peak in density, rises more steeply in time, and the temperature gradient at the plasma surface is less pronounced and less severe than when $\beta_\Lambda = 0$.

When these Saturn plasmas stagnate on axis, they produce the temperature and density profiles

that are shown in Figs. (2.15) and (2.16), respectively, at the time of peak compression. The dashed lines in these figures are the profiles generated in the $\beta_\Lambda = 0$ calculation; the solid lines are from the $\beta_\Lambda \neq 0$ calculation. The currents generated by the temperature gradients have acted to produce a slightly more compact plasma with a higher core density and a core temperature approximately 1.7 keV cooler than when $\beta_\Lambda = 0$. Thus, the severity of the temperature gradients has been reduced somewhat by their action on the current. A similar set of curves are shown in Figs. (2.17) and (2.18) for the PBFAZ calculations. Note that the greater current flow in PBFAZ produces greater differences between the $\beta_\Lambda = 0$ and $\beta_\Lambda \neq 0$ temperature and density profiles than in the Saturn calculations. The temperature reduction in the core is more significant, which leads to more significant increases in the core density when the β_Λ term acts on the magnetic field.

This element of computational self-consistency between the strengths of the magnetic field and the temperature gradients is seen more dramatically in Fig. (2.19), where the contour of $x_b \equiv \omega_c \tau_e$ is plotted for the two Saturn calculations. Since $\omega_c \tau_e$ has a minimum where the density peaks and the temperature has its minimum, the peak in $\omega_c \tau_e$ occurs behind the compressed shell. However, when currents are distributed by the combined action of the magnetic field and the temperature gradients, the $\omega_c \tau_e$ peak is reduced significantly.

The above effects occur because the diffusion of magnetic field and current into the plasma is significantly changed by the β_Λ current. We illustrate this point in Figs. (2.20) and (2.21). In these figures, current profiles at the time of peak compression are drawn relative to the (rescaled) temperature and density profiles of Figs. (2.15) and (16). In both figures, we plot the current flowing in the plasma inside of the radius, r: $I(r) \equiv 2\pi \int_0^r dr' r' j_z(r')$, but normalized to the total current, I_{total}, flowing in the plasma: $I_{total} \equiv 2\pi \int_0^R dr' r' j_z(r')$. Fig. (2.20) refers to the $\beta_\Lambda = 0$ calculation, and Fig. (2.21) to the $\beta_\Lambda \neq 0$ calculation. The dashed, vertical lines that are drawn in these figures indicate that 80% of the current flows within an annulus of radii, 0.223 and 0.293 mm, when $\beta_\Lambda = 0$ (Fig. (2.20)) while, when $\beta_\Lambda \neq 0$ (Fig. (2.21)), 80% of the current flows between radii, 0.245 and 0.277 mm, i.e., the current is much more concentrated in the $\beta_\Lambda \neq 0$ case. Note also that significantly more current is calculated to flow in the surface regions of the plasma when the β_Λ current is ignored. A similar finding was made in Ref. 13.

A similar set of curves is drawn in Figs. (2.22) and (2.23) for the PBFAZ calculations. In this higher total current case, less current flows in the shell region of the plasma (Fig. (2.22)) even when $\beta_\Lambda = 0$ than in the Saturn calculation (Fig. (2.20)). This situation looks more like the $\beta_\Lambda \neq 0$ Saturn calculation (Fig. (2.21)). The reason for this $\beta_\Lambda = 0$ PBFAZ behavior is seen in the $\beta_\Lambda \neq 0$ PBFAZ calculation. Fig. (2.23) shows that, when $\beta_\Lambda \neq 0$, a negative current density is induced to flow in the surface regions of the PBFAZ plasma.

The **A** and **B** locations are also significantly different in the Saturn and PBFAZ calculations. This behavior suggests that we examine the distribution of current in the plasma, I/I_{total}, as a function of the distribution of mass, m/m_{total}, at the time of peak compression, which quantities are plotted in Figs. (2.24) and (2.25) for the two Saturn and PBFAZ calculations, respectively. As with the temperature and density profiles, more mass shifting occurs between the two β_Λ calculations for PBFAZ than for Saturn. Fig. (2.26) shows the distribution of current relative to the distribution of mass for the four calculations. It vividly illustrates some of the significant differences in the plasmas generated by each of the four calculations. These differences in the underlying plasmas produce, in turn, significant differences in K-shell power outputs; these are shown in Figs. (2.27) and (2.28).

Finally, the large differences in current distribution between the two calculations at the time of peak compression suggest that these differences should continue to persist and/or grow at later times during the bounce and recompression phase of the dynamics. Figs. (2.29) and (2.30) confirm this to be the case. They present comparisons of the temperature and density profiles, respectively, that were calculated in the two β_Λ cases at 95 ns in the Saturn calculations. At this time, the two plasmas have essentially the same size, but their temperature and density profiles are different. In the absence of the β_Λ term, the plasma has a steep temperature gradient at the front surface, a sharply peaked density spike behind the front surface, and a density bulge behind this spike.

E. Summary

One of the main purposes of modeling z-pinch implosions by means of 1-D RMHD computer calculations is to be able to predict the average gradient structure of the optically thick plasmas on axis and to relate this structure to the x-ray emission characteristics of the plasma. Because a z-pinch's hydrodynamics is significantly impacted by the radiation losses that occur throughout the pinch dynamics, and because the emission spectrum is, in turn, significantly impacted by the hydrodynamics, the main virtue of a 1-D calculation is that it can be designed to contain a self-consistent, detailed, and accurate description of the optically-thick radiation dynamics. The main drawback of such calculations is that, when experiments are conducted that contain a significant amount of 3-D fluid turbulence or instability, these multi-dimensional effects must be modeled in 1-D calculations in a somewhat ad hoc fashion at present if comparisons with these less than ideal experiments are necessary. However, even when such effects are minimized experimentally, one must still use the full power of the computer in order to adequately address a number of important, but difficult, nonlinear dynamical, 1-D z-pinch effects.

One such nonlinear problem was investigated this year: the penetration of the magnetic field into a plasma having a shell structure and carrying currents of 7 to 17 MA. Currents are then induced, which are dependent on the strength of the magnetic field and are proportional to the gradient in temperature. These currents act as a source term in the magnetic field equation. A significant redistribution of current density occurs. At peak compression, 80% of the current becomes concentrated in a region of plasma 1/2 or less the size of the region it would have occupied without the induced current, and surface currents are suppressed or reversed. These changes in the current produce corresponding changes in the temperature, which, in turn, produce changes in the ionization state and in the $\omega_c\tau_e$ values upon which the β_Λ coefficient depends.

The calculations that were described in this section utilized formulas for the electrical conductivity that were derived by doubling the number of terms in the Laguerre expansions of the anisotropic part of the electron distribution function that Braginskii had used. Both the $\omega_c\tau_e$ and the Z dependence of these coefficients was derived. By doubling the number of terms in the expansion, the accuracy of the formulas was found to be doubled. Thus, in the $\beta_\Lambda \neq 0$ Saturn calculation, for example, $\omega_c\tau_e$ ranged over values for which the formula for β_Λ had accuracies of 5% or better.

Another important nonlinear effect of the magnetic field is to induce a heat flow in the radial direction due to the current flow in the axial direction. However, because enhanced values were used for $\kappa_\perp$ in these calculations, the β_Λ influence on heat flow was not investigated in this work.

How these nonlinear B-field effects scale to different atomic number loads also needs to be investigated, as does the sensitivity of these results to the initial density profile and to the zoning

used in the calculation. Experiments on the Magpie generator at Imperial College in London[14] are currently ongoing to characterize the low density plasma that blows off early in time from wire loads. Its influence on the modeling of z-pinch implosions has yet to be even partially understood and quantified. If one is to attribute, with some certainty, a portion of z-pinch phenomena to 2-D effects, then one must have identified and understood, with equal certainty, all of the important 1-D effects.

REFERENCES

1. C. Deeney, T. Nash, R. R. Prasad, L. Warren, K. G. Whitney, J. W. Thornhill, and M. C. Coulter, "Role of the Implosion Kinetic Energy in Determining the Kilovolt X-ray Emission from Aluminum-wire-array Implosions", Phys. Rev. A **44**, pp. 6762-6775, Nov. 1991.

2. J. W. Thornhill, K. G. Whitney, C. Deeney, and P. D. LePell, "Phenomenological Modeling of Turbulence in Z-pinch Implosions", Phys. Plasmas **1**, pp. 321-330, Feb. 1994.

3. S. I. Braginskii, "Transport Processes in a Plasma", in *Reviews of Plasma Physics*, edited by M.A. Leontovich, vol. 1, pp. 205-311, Consultants Bureau, N.Y. (1965).

4. K. G. Whitney, J. W. Thornhill, P. E. Pulsifer, J. P. Apruzese, T. W. L. Sanford, T. J. Nash, R. C. Mock, and R. B. Spielman, "Analyzing Time-resolved Spectroscopic Data from an Azimuthally Symmetric, Aluminum-wire Array, Z-pinch Implosion", Phys. Rev. E **56**, 3540, (1997).

5. E. M. Epperlein and M. G. Haines, "Plasma Transport Coefficients in a Magnetic Field by Direct Numerical Solution of the Fokker-Planck Equation", Phys. Fluids. **29**, pp. 1029 1041, Apr. 1986.

6. T. W. L. Sanford, G. O. Allshouse, B. M. Marder, T. J. Nash, R. C. Mock, R. B. Spielman, J. F. Seamen, J. S. McGurn, D. Jobe, T. L. Gilliland, M. Vargas, K. W. Struve, W. A. Stygar, M. R. Douglas, M. K. Matzen, J. H. Hammer, J. S. De Groot, J. L. Eddleman, D. L. Peterson, D. Mosher, K. G. Whitney, J. W. Thornhill, P. E. Pulsifer, and J. P. Apruzese, "Improved Azimuthal Symmetry Greatly Increases X-ray Power from Wire-array Z-pinches", Phys. Rev. Lett, **77**, 5063 (1996).

7. T. W. L. Sanford, T. J. Nash, R. C. Mock, R. B. Spielman, J. F. Seamen, J. S. McGurn, T. L. Gilliland, M. Vargas, K. G. Whitney, J. W. Thornhill, P. E. Pulsifer, and J. P. Apruzese, "Time-dependent Electron Temperature Diagnostics for High-power, Aluminum Z-pinch Plasmas", Rev. Sci. Instrum., **68**, 852 (1997).

8. M.C. Coulter, K.G. Whitney and J.W.Thornhill, J. Quant. Spectrosc. Radiat. Transfer **44**, 443 (1990).

9. J. P. Apruzese, K. G. Whitney, J. Davis, and P. C. Kepple, "K-shell Line Ratios and Powers for Diagnosing Cylindrical Plasmas of Neon, Aluminum, Argon, and Titanium", J. Quant. Spectrosc. Radiat. Transfer, **57**, 41 (1997)).

10. C. Deeney, P. D. Lepell, B. H. Failor, S. L. Wong, J. P. Apruzese, K. G. Whitney, J. W. Thornhill, J. Davis, E. Yadlowsky, R. C. Hazelton, J. J. Moschella, T. Nash, and N. Loter, "Increased Kilo-electron-volt X-ray Yields from Z-pinch Plasmas by Mixing Elements of Similar Atomic Numbers", Phys. Rev. E **51**, pp. 4823-4832, May 1995.

11. E. J. Yadlowsky, J. J. Moschella, R. C. Hazelton, T. B. Settersten, G. G. Spanjers, C. Deeney, B. H. Failor, P. D. Lepell, J. Davis, J. P. Apruzese, K. G. Whitney, and J. W. Thornhill, Phys. Plasmas **3**, 1745 (1996).

12. T. W. L. Sanford, T. J. Nash, R. C. Mock, R. B. Spielman, K. W. Struve, J. H. Hammer, J. S. De Groot, K. G. Whitney, and J. P. Apruzese, "Dynamics of a High Power Aluminum-wire Z-pinch Implosion", Phys. of Plasmas, **4**, pp. 2188-2203, Jun. 1997.

13. F. S. Felber, M. A. Liberman, and A. L. Velikovich, "Magnetic Flux Compression by Dynamic Plasmas. I. Subsonic Self-similar Compression of a Magnetized Plasma-filled Liner", Phys. Fluids **31**, pp. 3675-3682, Dec. 1988.

14. C. Deeney, private communication.

Aluminum wire number scan: Data Summary

SHOT	N	Wire (mil)	Yield (kJ)	Pulsewidth (ns)	Avg/Peak PCD215 (TW)	Pinch dia (mm)	Ly α/ (He α+IC)	Ly β/ He β	n_i (cm^{-3})	T_e (eV)
2080	38	0.8	50.0	11.20	0.73 2.92					
2081	48	0.7	42.8	8.80	0.76 3.09	1.0	1.40	1.32	9.39E19 1.16E20	565 423
2082	66	0.6	40.5	6.60	0.85 3.63	0.9	1.79	1.25	1.22E20 1.57E20	675 420
2083	16	1.2				1.8	1.16	0.90		
2084	10	1.5	42.4	64.00	0.25 0.66	1.8	1.59 1.54	1.62 1.60	1.67E19 1.87E19	1084 1389
2085	90	0.5	50.9	5.40	0.80 3.96	1.0	1.79	1.21	9.03E19 1.22E20	672 413
2086	16	1.2	67.8	39.40	0.45 1.46	1.4	1.45	1.71	3.72E19 4.41E19	745 574
2087	30	1.0	76.2	19.20	0.72 2.49	1.8	1.33	1.11	4.14E19 6.10E19	648 413
2088	46	0.8	59.2	13.20	0.56 2.56	0.8	1.42	1.11	9.94E19 1.29E20	571 404
2089	61	0.7	62.0	11.20	0.54 2.75	1.6	1.10	0.98	4.35E19 6.07E19	560 400
2090	83	0.6	49.8	8.60	0.72 3.25	1.1	1.46	1.17	8.90E19 1.16E20	588 408
2091	120	0.5	52.5	6.60	0.75 3.88	1.0	1.40	0.97	9.31E19 1.27E20	566 386
2092	20	1.2	74.6	27.60	0.78 2.01	1.4	1.25	1.13	6.60E19 8.55E19	550 405
2093	13	1.5	69.0	96.00	0.32 0.68	3.0	0.89	1.16	1.05E19 1.15E19	852 1253
2094	90	0.5	34.9	3.60	0.97 4.75	1.0	1.84	1.17	1.01E20 1.36E20	713 410
2095	90	0.5	51.0	5.20	0.86 4.33	0.6	1.61 1.46	1.21 1.17	1.76E20 2.13E20	580 422

Table 2.1

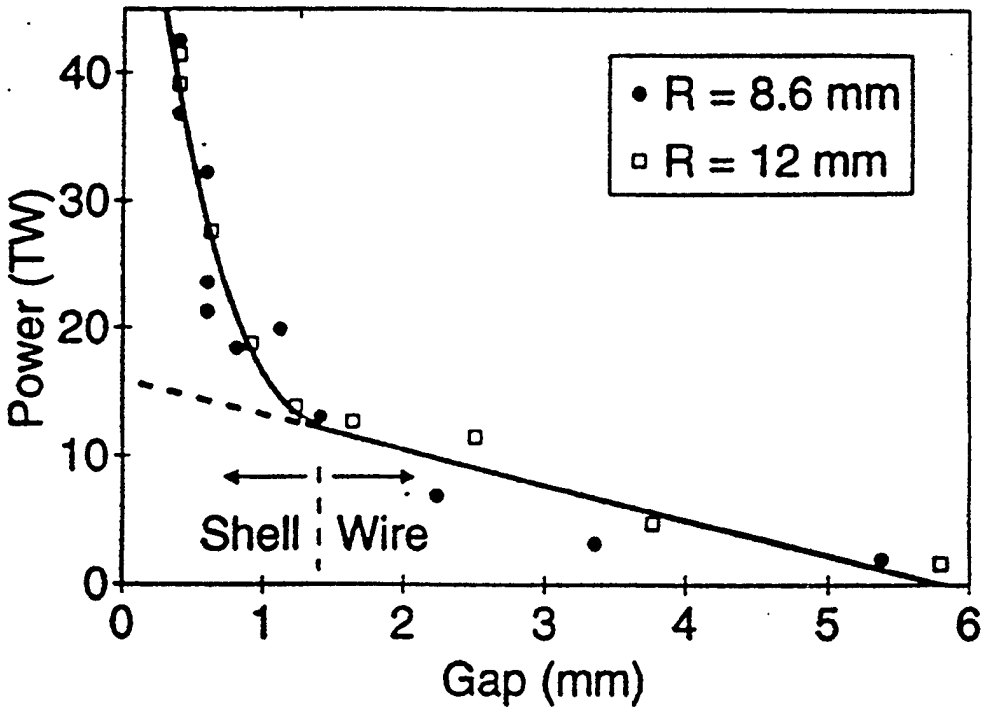

Figure 2.1

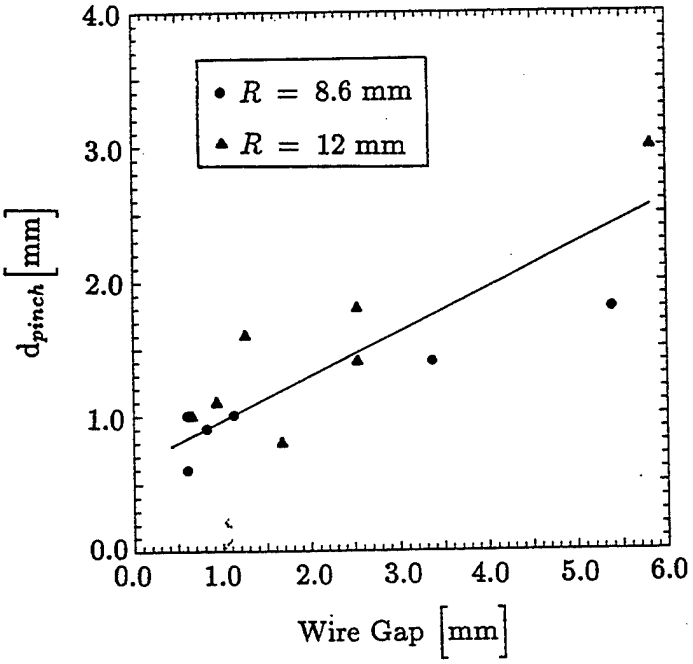

Figure 2.2

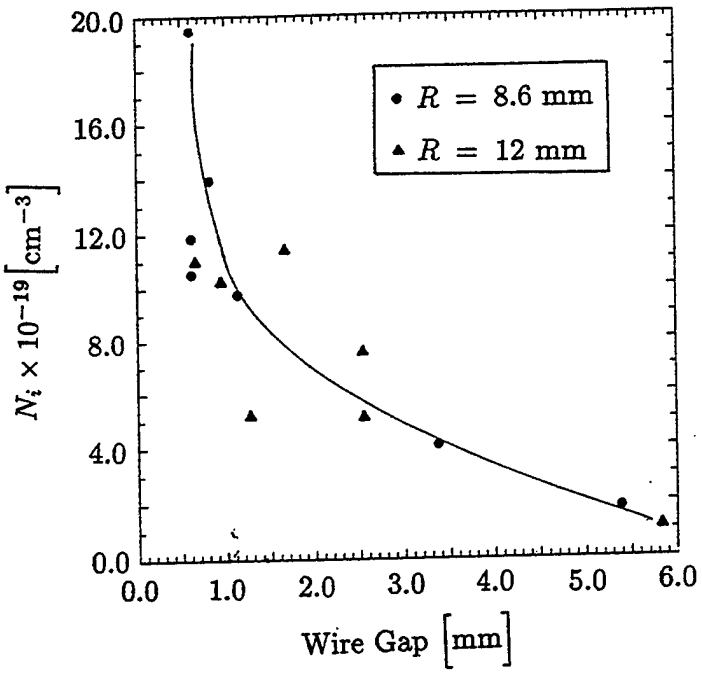

Figure 2.3

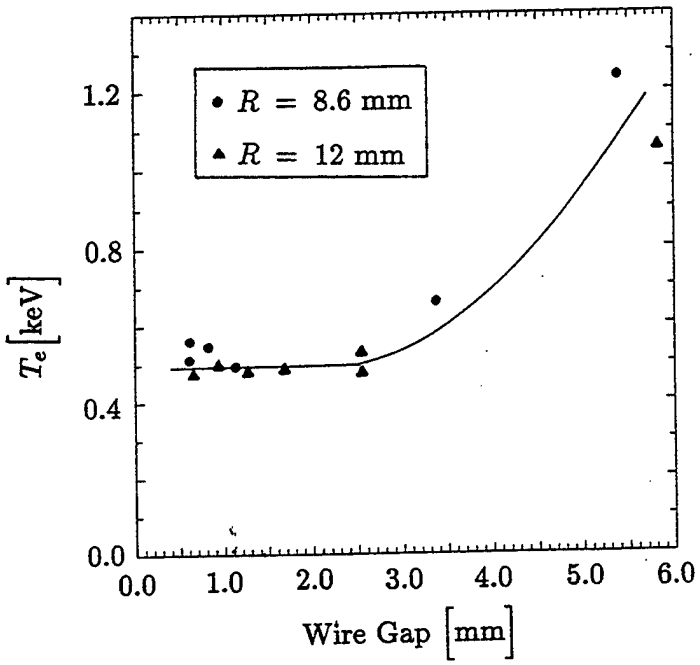

Figure 2.4

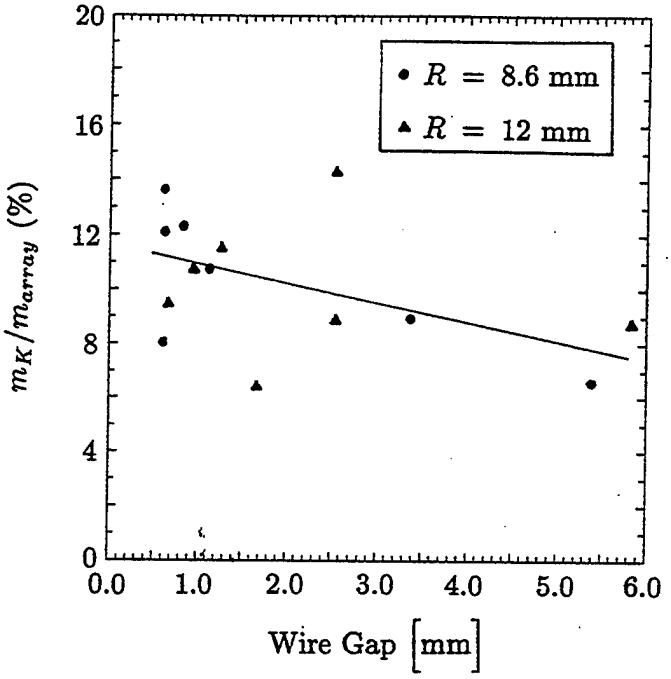

Figure 2.5

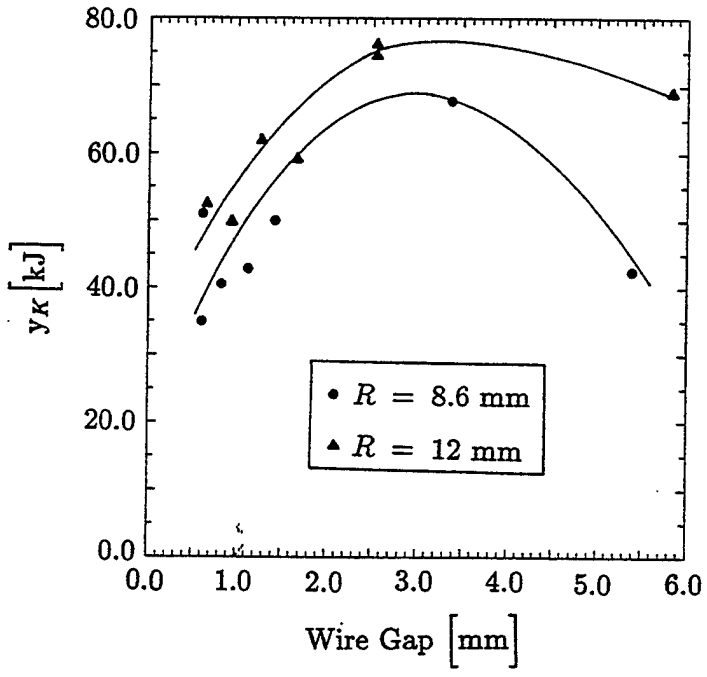

Figure 2.6

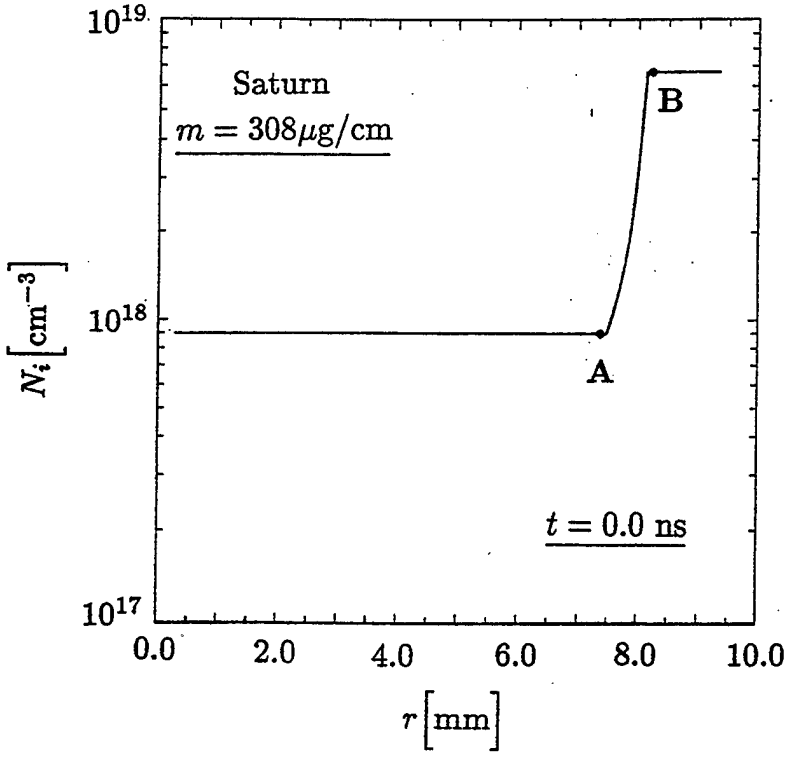

Figure 2.7

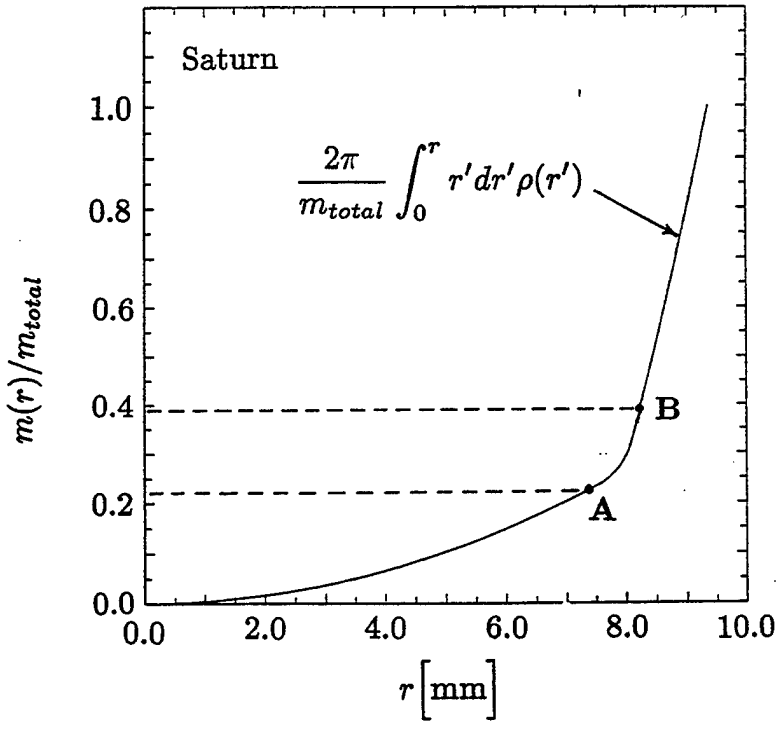

Figure 2.8

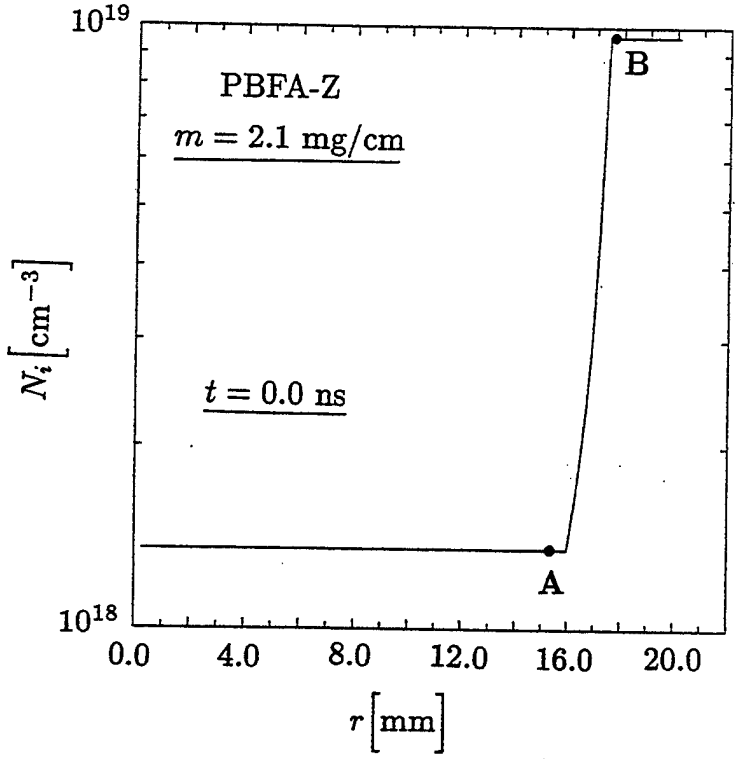

Figure 2.9

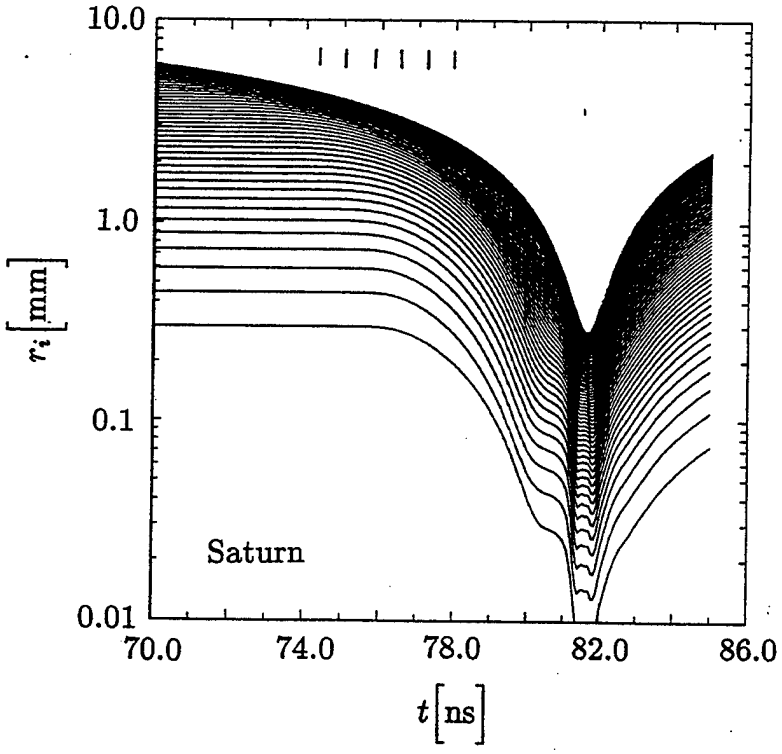

Figure 2.10

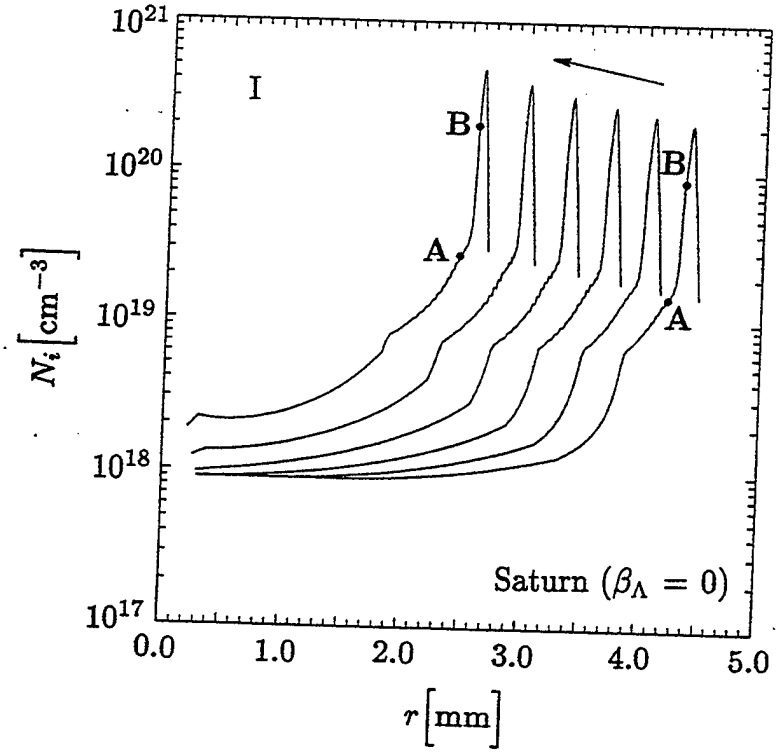

Figure 2.11

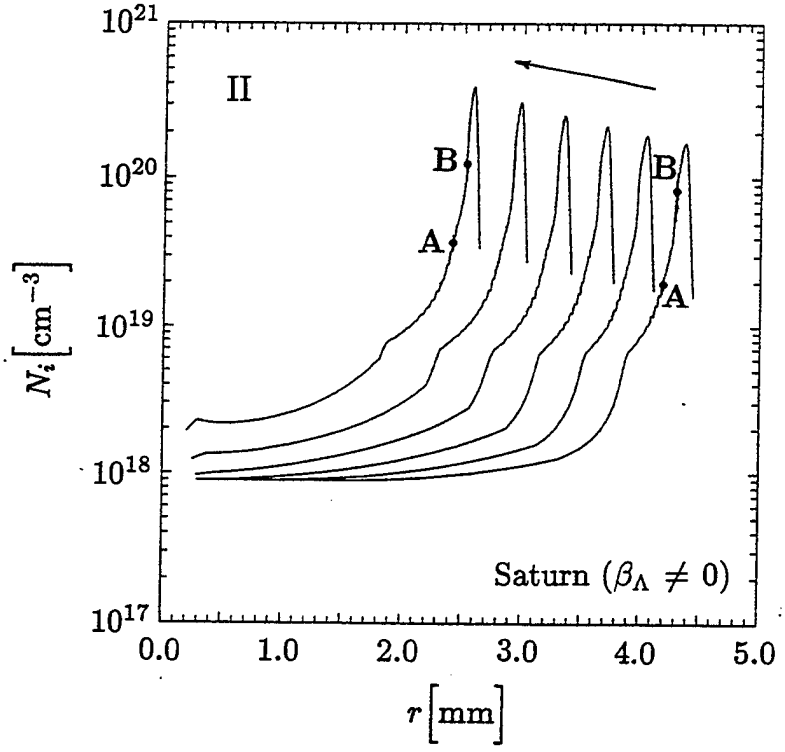

Figure 2.12

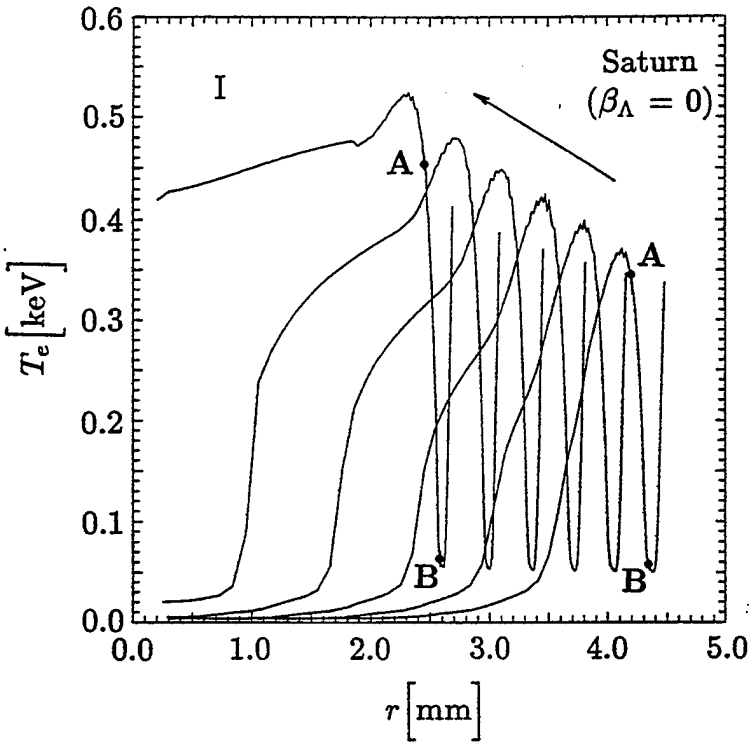

Figure 2.13

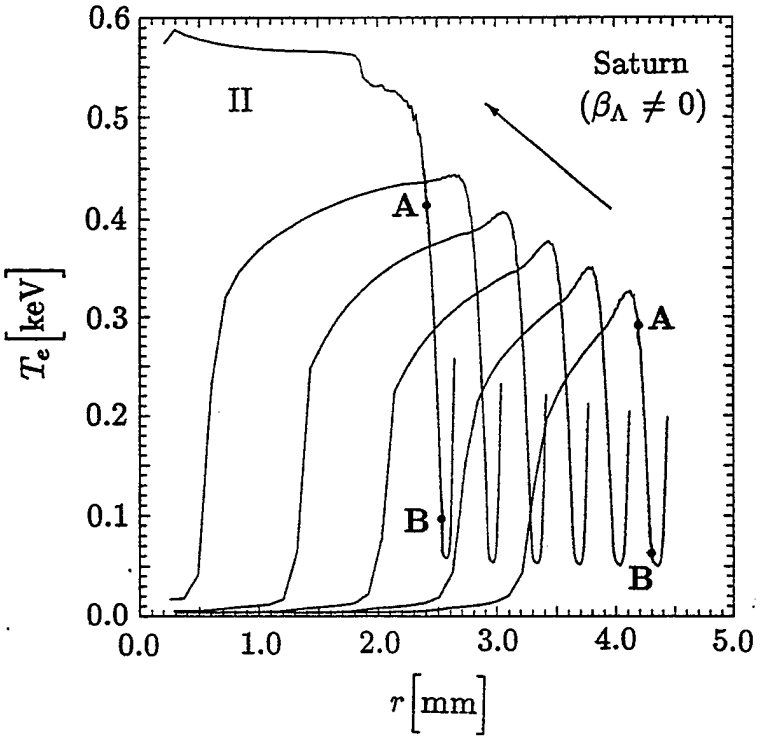

Figure 2.14

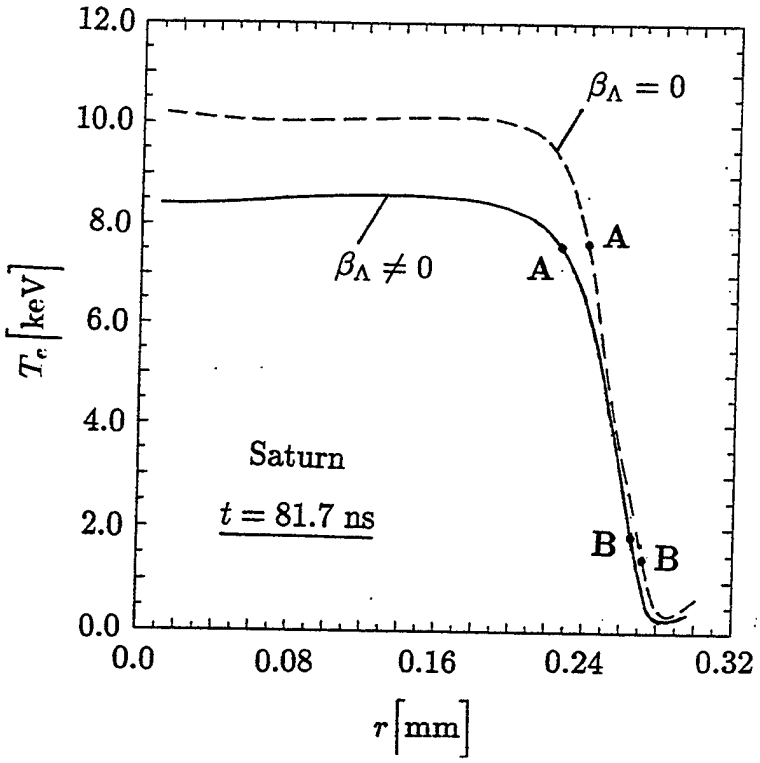

Figure 2.15

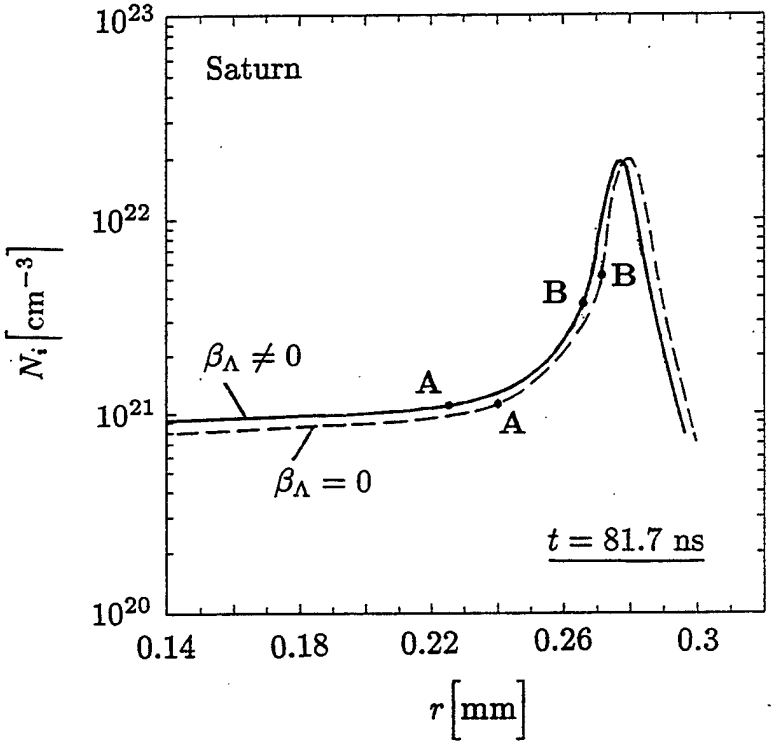

Figure 2.16

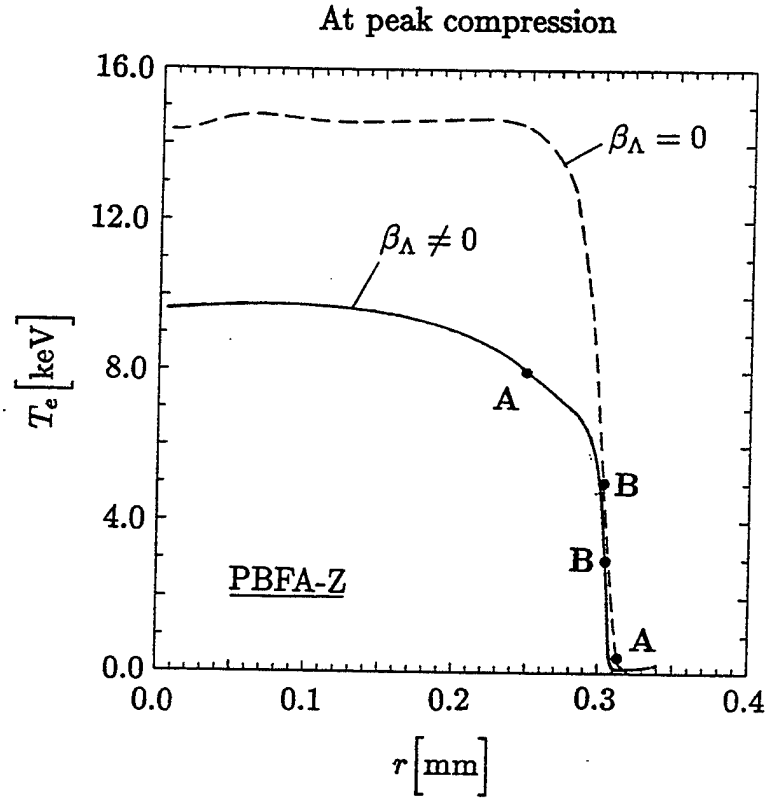

Figure 2.17

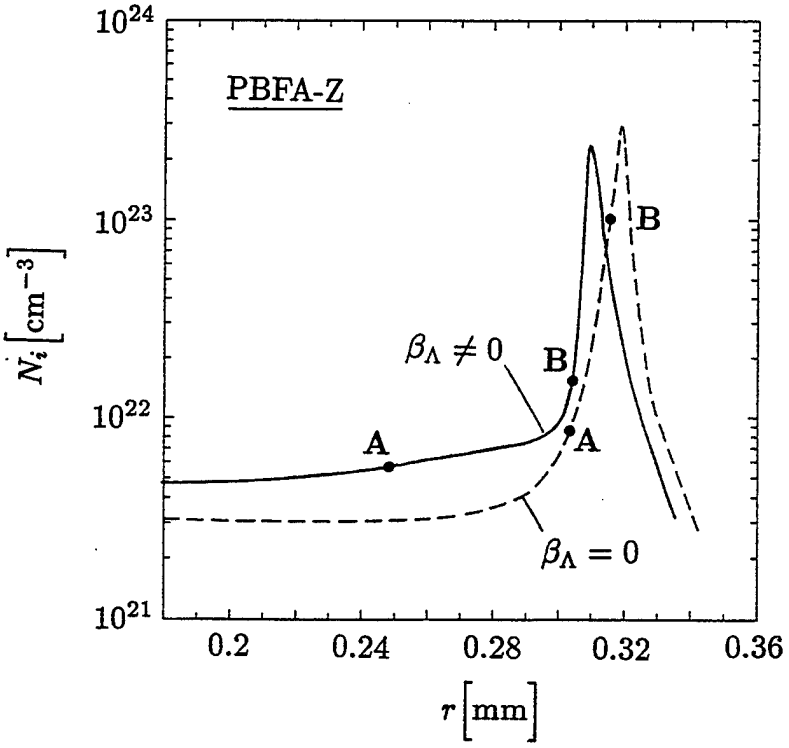

Figure 2.18

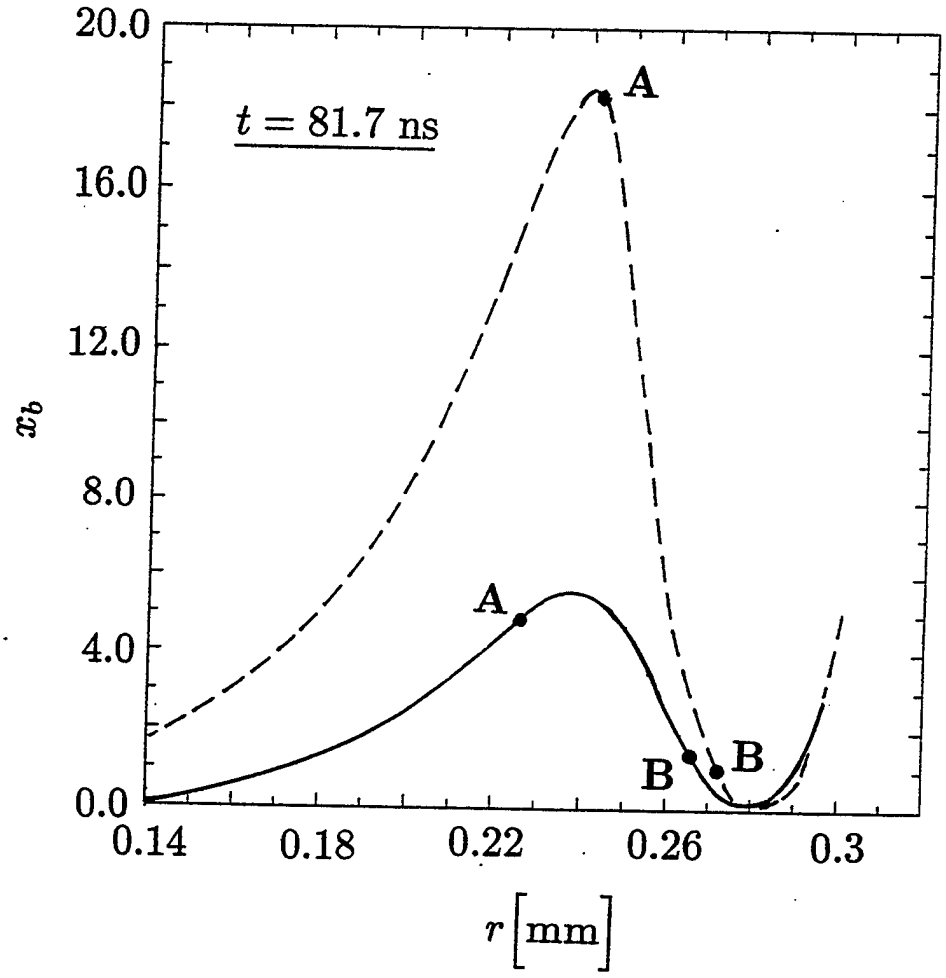
20.0
16.0
12.0
8.0
4.0
0.0
x_b
$t = 81.7$ ns
A
A
B
B
0.14
0.18
0.22
0.26
0.3
$r\left[\text{mm}\right]$

Figure 2.19

At peak compression

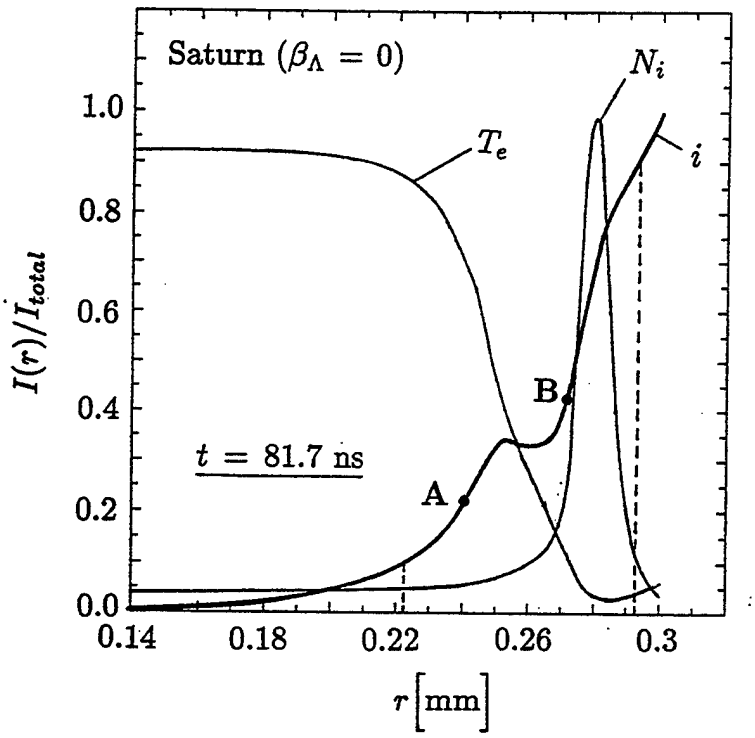

Figure 2.20

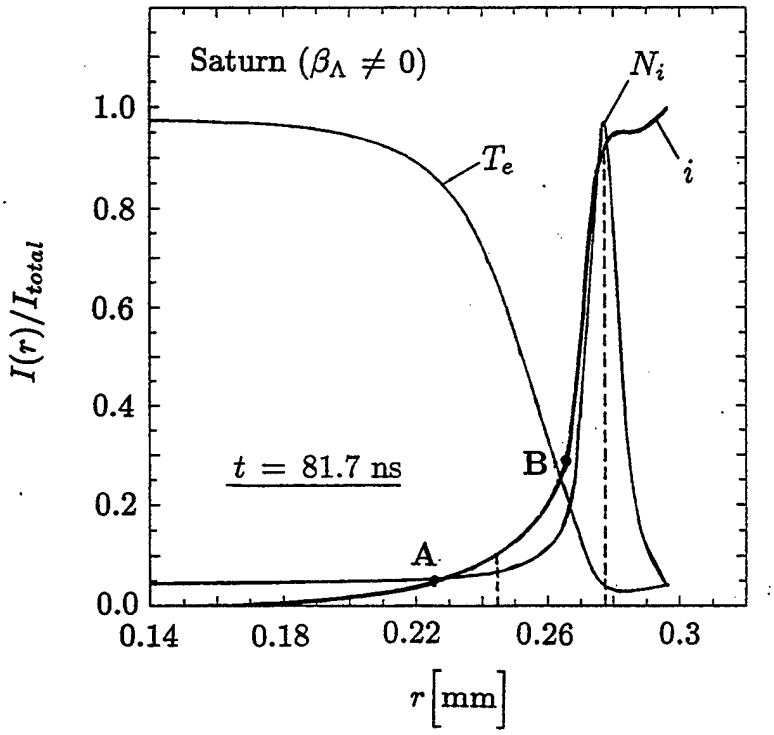

Figure 2.21

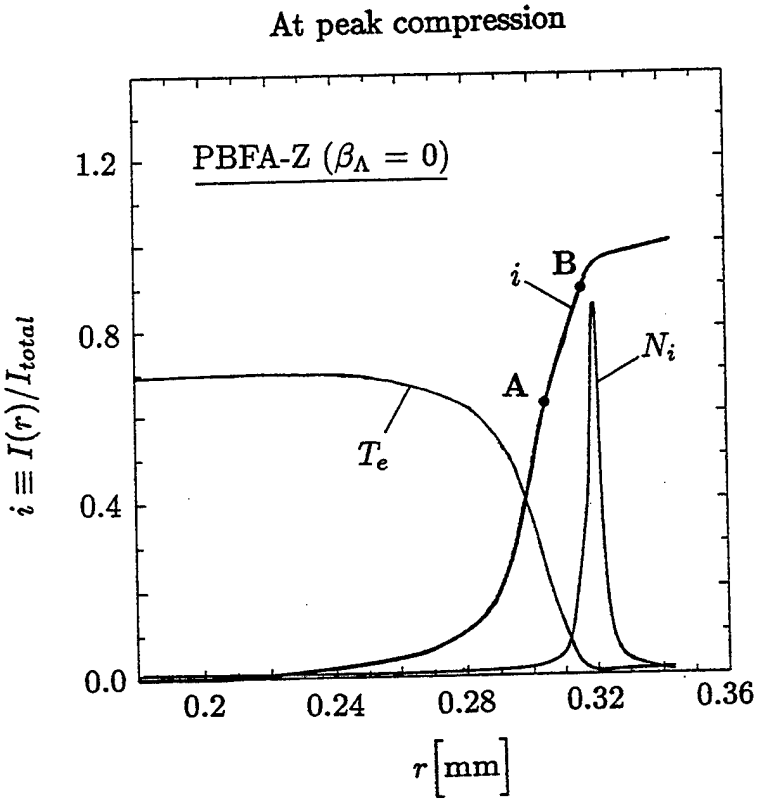

Figure 2.22

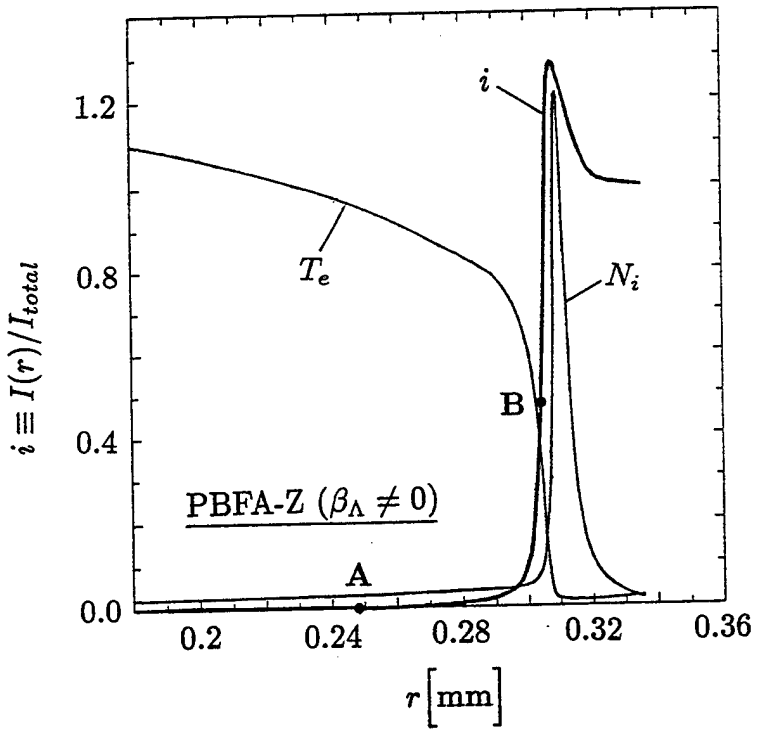

Figure 2.23

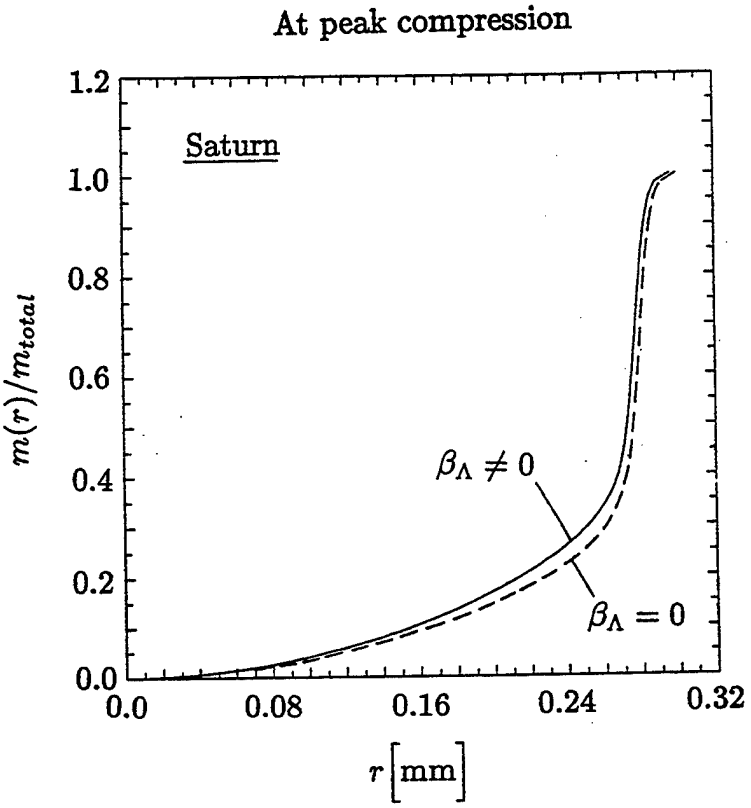

Figure 2.24

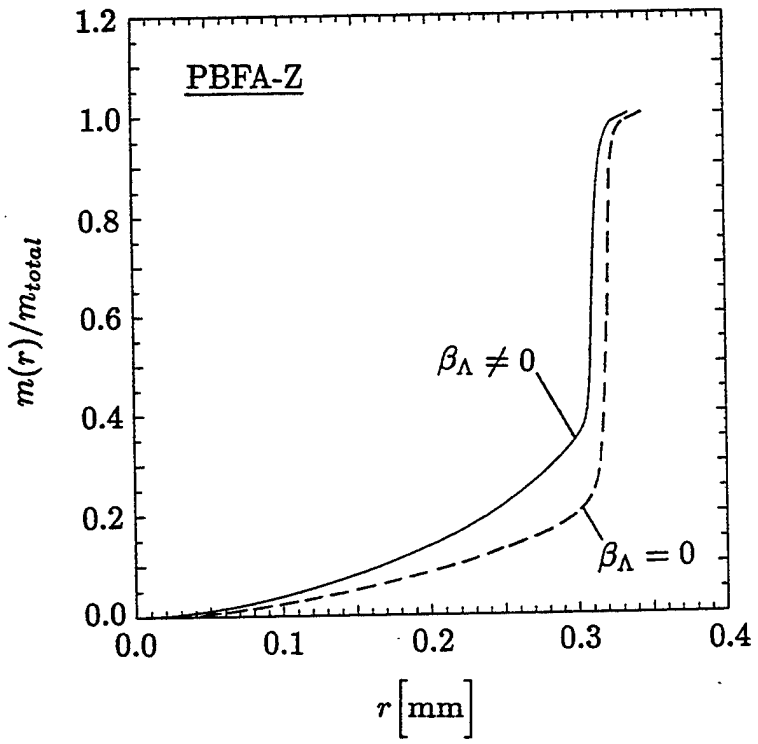

Figure 2.25

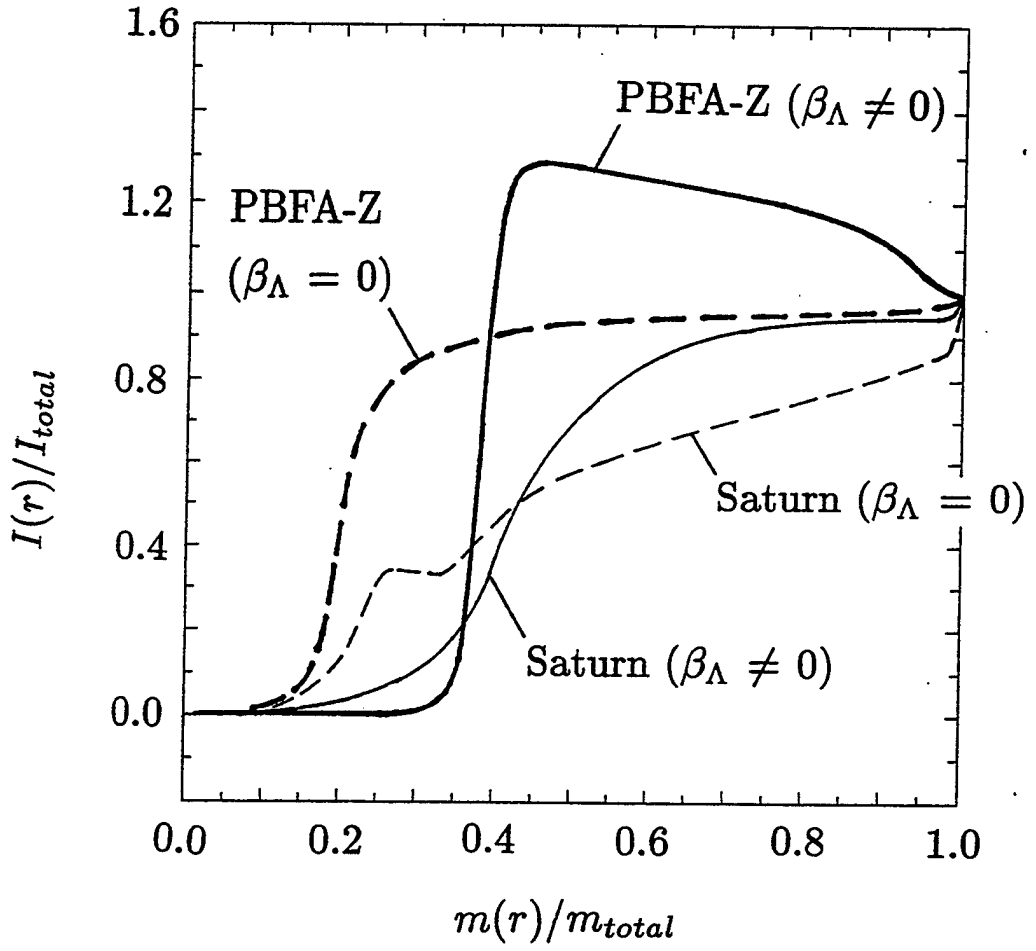
1.6
1.2
0.8
0.4
0.0
0.0
0.2
0.4
0.6
0.8
1.0
PBFA-Z ($\beta_\Lambda \neq 0$)
PBFA-Z
($\beta_\Lambda = 0$)
Saturn ($\beta_\Lambda = 0$)
Saturn ($\beta_\Lambda \neq 0$)
$I(r)/I_{total}$
$m(r)/m_{total}$

Figure 2.26

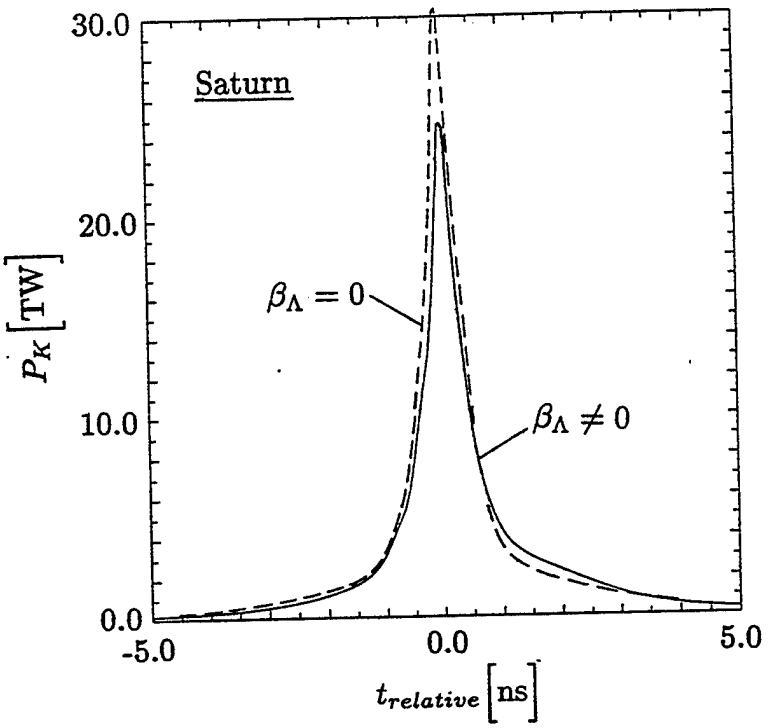

Figure 2.27

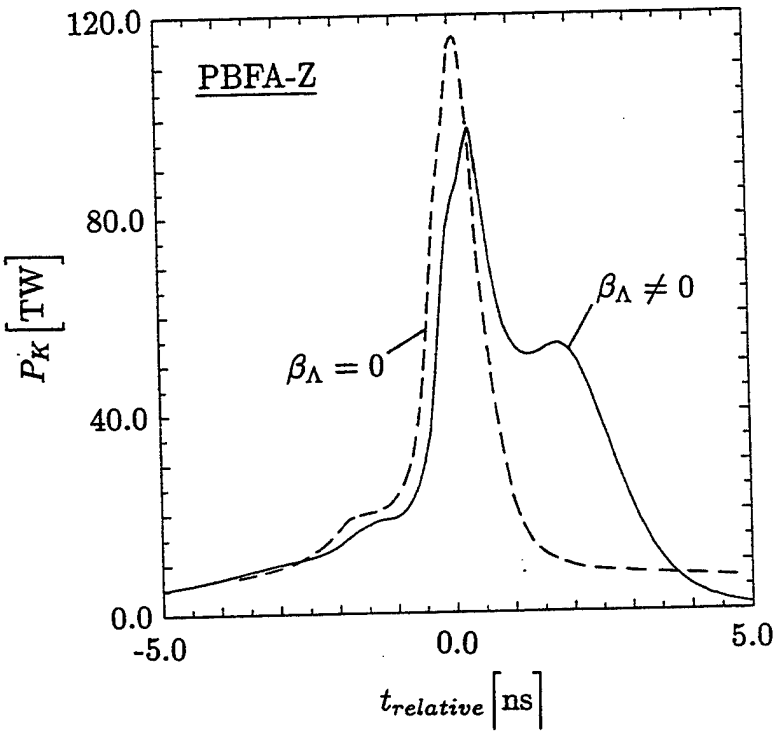

Figure 2.28

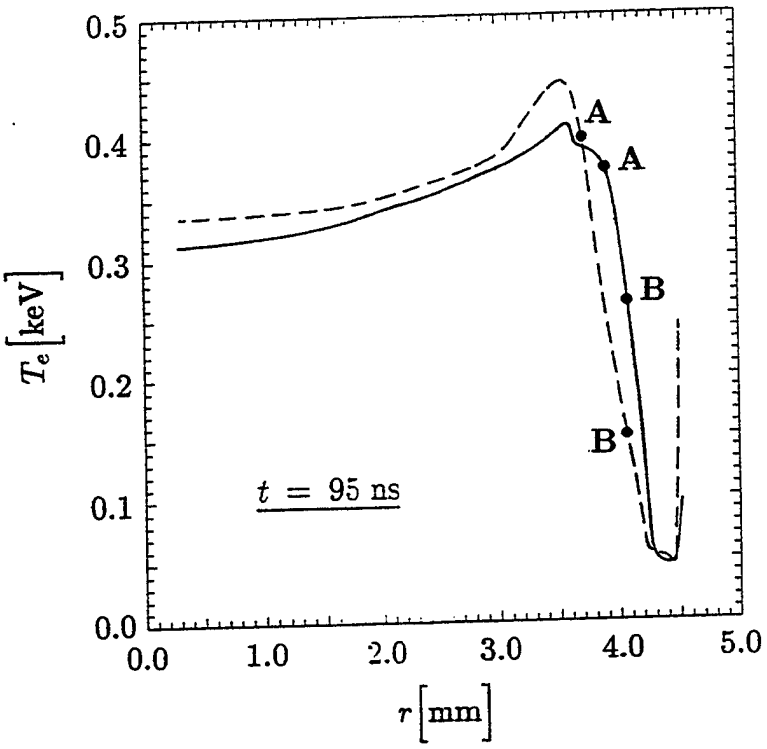

Figure 2.29

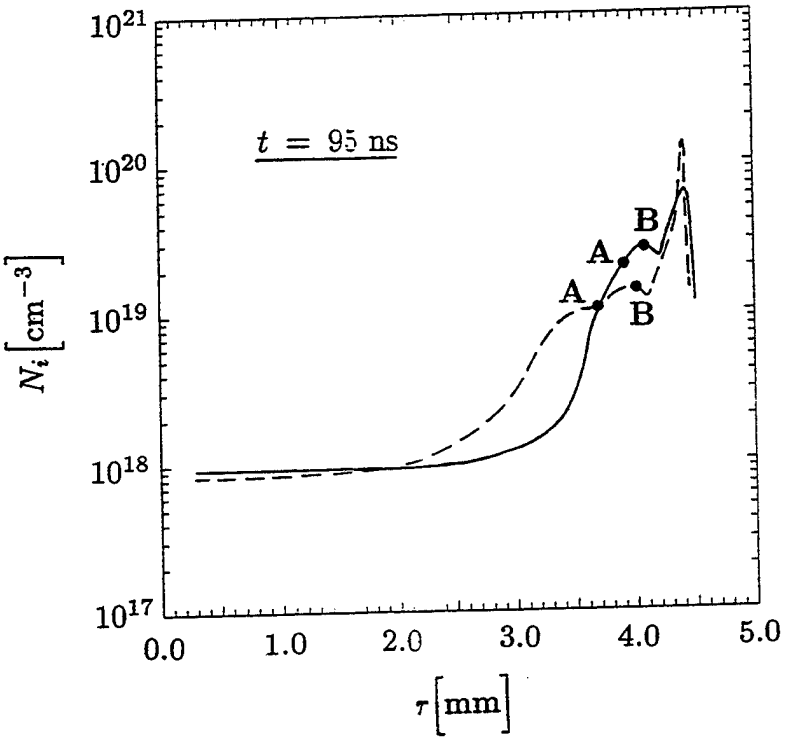

Figure 2.30

III. DECADE QUAD LOAD PERFORMANCE

A. Introduction

The performance of plasma radiation source (PRS) loads imploded by a long current pulse machine is investigated theoretically. The emission tolerant (with oil) Decade Quad design of Pulse Sciences Incorporated is an example of such a long current rise time machine. It has a peak short circuit current of 9 MA that is reached in 300 nanoseconds. Large radius loads must be employed for this type of machine in order to insure that high implosion velocities are reached and that the available energy is utilized. However, large radius implosions are known to be susceptible to the Rayleigh Taylor instability. The extent to which this instability affects the ability of an argon load to radiate K-shell photons is not known and is the subject of this model investigation.

One way to establish a theoretical relationship between the Rayleigh Taylor (RT) stability of an argon load and its ability to efficiently radiate K-shell photons would be to perform two-dimensional (2D) or three-dimensional (3D), time dependent, non-LTE, full radiation transport, MHD calculations. However, this capability does not fully exist in the Z-pinch community primarily because the computer requirements for performing the zone to zone coupling needed to transport radiation in a 2D or 3D plasma are prohibitive. Our 2D MHD model,[1,2] PRISM (which stands for plasma radiating imploding source model), assumes that either the plasma is transparent to radiation or that a local probability of escape model can be used to model some of the self-absorption physics. The LTE radiative diffusion model, used by the 2D Z-pinch community, is also inadequate for modeling the radiation physics of PRS loads designed for K-shell emission because neither the diffusion approximation nor the LTE assumption are valid for this type of plasma. Given these model limitations, we have used the following approach to analyze the K-shell emission capabilities of large radius loads[3]: (1) the pinch is initialized with a density perturbation to seed the RT instability, (2) the PRISM code calculates the evolution of the pinch to the point where radiation effects begin to dominate, and then (3) K-shell scaling relations are employed to assess K-shell emission from each axial slice of the 2D load profile. These scaling relations are based on past experimental results and on 1D MHD calculations.[4,5] The probability of escape radiation

transport and collisional radiative ionization dynamics models[6] used in the 1D calculations are more appropriate for approximating the radiation physics of K-shell PRS loads than what is used in a typical 2D calculation. This approach is applied to examining stability and its effect on K-shell yield performance on DECADE QUAD loads that are initially 3.6 cm in radius, and of uniform density.

B. Model

PRISM is a 2D MHD code that models the plasma under the assumptions that its ionization dynamics is in collisional radiative equilibrium. Opacity is not taken into account so the plasma is not photo excited. This treatment simplifies the calculation of the evolution of the RT instability during the runin phase of the implosion. It is probably most valid in situations where the radiative powers are substantially less than the time rate of change of kinetic energy into internal energy during the stagnation phase of the implosion. The 2D portion of the calculation is terminated at the end of the runin phase of the implosion when the change of inductance due to the imploding load is the same as that achieved by a 10:1 compression in a one-dimensional calculation. The choice of cutoff condition is not that critical for the purposes of this investigation since inductance depends logarithmically on radius and many Z-pinch experiments have exhibited similar compressions. The initial perturbation wavelength λ is chosen to be 0.5 cm, which is a typical disruptive wavelength. It is a non-compressible perturbation characterized by: (1) $\rho' = \rho_o \times (0.25) \times cos(2\pi z/\lambda)$; where the mass density ρ equals ρ_o (initial mass density) $+\rho'$ and (2) $u' = -u_o \times (0.25) \times cos(2\pi z/\lambda)$; where the radial velocity u equals u_o (initial radial velocity) + u'. The perturbation is turned on 40 ns after the start of the current pulse and it is limited to zones near the outer radius because it is only applied when $|u| > 0.1 \times |u_{max}|$. The $J \times B$ force that implodes the PRS load is calculated self-consistently in PRISM by solving a lumped circuit equation for the DECADE QUAD current.

Once the 2D portion of the calculation is terminated, K-shell yield scaling relations (see Appendix) are applied to the plasma to determine the K-shell emission from each axial slice of the 2D pinch. These scaling relations express the K-shell yield per unit axial length as a function of the mass per unit length and energy (kinetic + internal) per unit length. These quantities are obtained for each axial slice of the pinch by adding all the radial contributions (orthogonal grid) and dividing

by the length of each axial slice. In essence this approach segments the 2D load profile into a series of 1D profiles.

C. Results

As the RT instability grows it moves mass and energy out of the "bubble" regions and transfers it to the "spike" regions of the plasma. This process is illustrated in Fig. 1 where the mass per unit length of the spike and bubble regions are shown as a function of time. In this example, the 10:1 effective compression is achieved at 240 ns at which time the mass per unit length in the bubble regions is approximately 1/3 that in the spike regions. This feature of the RT instability produces deviations in calculated K-shell yield from 1D behavior due to local deviations in either the mass per unit length and/or the energy per unit length of the plasma. The effect these local deviations have on K-shell emission is shown in Fig. 2 where 0D and 2D scaled argon K-shell yields as a function of initial mass are compared. The reasons for the emission behavior shown in Fig. 2 can be found in the following observations obtained for this load configuration at stagnation: 1) the energy contained in the spike regions is nearly the same as the energy contained in the bubble regions, 2) the spike regions subtends about the same length of the axis as the bubble regions, 3) the spike to bubble mass ratio is approximately 3:1, and 4) the implosion time and peak current are 10 percent lower in the 2D calculation than in the 0D calculation. This latter effect occurs because the effective 10:1 change in inductance is achieved earlier in time in the 2D implosion as a consequence of the earlier arrival on axis of the bubble region of the plasma. The first three of these observations imply that an initially uniform 500 $\mu g/cm$ load evolves into 250 $\mu g/cm$ bubble regions and 750 $\mu g/cm$ spike regions at stagnation. Because of their additional mass the spike regions are not predicted to emit much K-shell emission because their specific energy as characterized by η^* (see Appendix) is too low. The K-shell emission comes almost exclusively from the bubble regions for initial mass loads greater than 500 $\mu g/cm$. For most mass loads the 2D yields are reduced below the 0D yields for the reason just mentioned and also because the reduced current (10 percent) leads to a 20 percent reduction ($I^2 scaling$) in energy coupling to the 2D load. However, the 10 kJ/cm K-shell yield shown in Fig. 2 for the 800 $\mu g/cm$ initial mass load is much larger than the corresponding 0D yield. This yield is due to the larger energy that is coupled to the

larger initial mass loads (Fig. 3) and to the high specific energy in the bubble regions of the plasma. The 0D peak currents, η^*s and energies are shown in Fig. 3. Note, there is a large uncertainty in predicting K-shell emission from either scaling calculations or from past experiments whenever $\eta^* < 2$.

D. Conclusions

This model study suggests that the Rayleigh Taylor instability has the potential to substantially alter the amount of PRS K-shell emission from that which is expected from purely 1D behavior. As modeled this alteration is due mainly to the flow of mass from the bubble to the spike regions of the instability. The spike regions of the instability were 3 times more massive than the bubble regions for the 3.6 cm radius, uniform density profile, DECADE QUAD argon loads examined here. For optimal 2D loads, this limited the source of K-shell emission to the bubble region of the instability. Although, it was not described in this paper, we also modeled 2.25 cm radius, uniform density, argon Saturn loads. In this case, the spike to bubble mass ratio was approximately 2 and there was little difference in calculated K-shell yield between the 2D and 0D models. On the other hand, we also analyzed a 4.5 cm radius uniform density DECADE QUAD load that never imploded all the way to the axis because virtually all of the mass was pushed out of the bubble region.

Appendix: Z Scaling of K-shell Emission

$$\text{Energy (J/cm)} = (\text{kinetic energy} + \text{internal energy})\ \text{(J/cm)}$$

$$\eta^* = \text{Energy} \times 1.1 \times 10^{-5} \times Z^{-2.41}/\text{Mass (g/cm)}$$

$$\alpha = \frac{2.58 \times 10^{-12} \times Z^{5.96}}{e^{-20.6/Z^{0.9}}} \times \max(1.0, \frac{\eta^{*2}}{\eta^* + 12})$$

$$\beta = \min(0.3\ \text{Energy}, \frac{0.3 \times \text{Energy} \times \text{Mass}}{\alpha})$$

$$\text{K-shell yield (J/cm)} = \begin{cases} \beta, & \eta^* > 1.5; \\ \beta \times (\eta^* - 0.5), & 1.0 < \eta^* < 1.5; \\ \frac{1}{2}\beta \times (1 - [(1 - \eta^*)/0.25]^{0.5}), & 0.75 < \eta^* < 1.0; \\ 0, & \eta^* < 0.75 \end{cases}$$

Note, there is no accounting for innershell absorption effects in this scaling. Also, these scaling relations are based on CRE calculations, which do not account inherently for the time dependence of the ionization process. The uncertainty in this scaling is large for $\eta^* < 2$.

References

1. F. L. Cochran, J. Davis, and A. L. Velikovich, Phys. Plasmas 2, 2765 (1995).

2. A. L. Velikovich, F. L. Cochran, and J. Davis, Phys. Rev. Lett. 77, 853 (1996).

3. This approach was initiated by F. L. Cochran

4. K. G. Whitney, J. W. Thornhill, J. P. Apruzese, and J. Davis, J. Appl. Phys. 67, 1725 (1990).

5. J. W. Thornhill, K. G. Whitney, J. Davis, and J. P. Apruzese, J. Appl. Phys. 80, July 15, (1996).

6. J. P. Apruzese, J. Davis, D. Duston, and R. W. Clark, Phys. Rev. A29, 246 (1984).

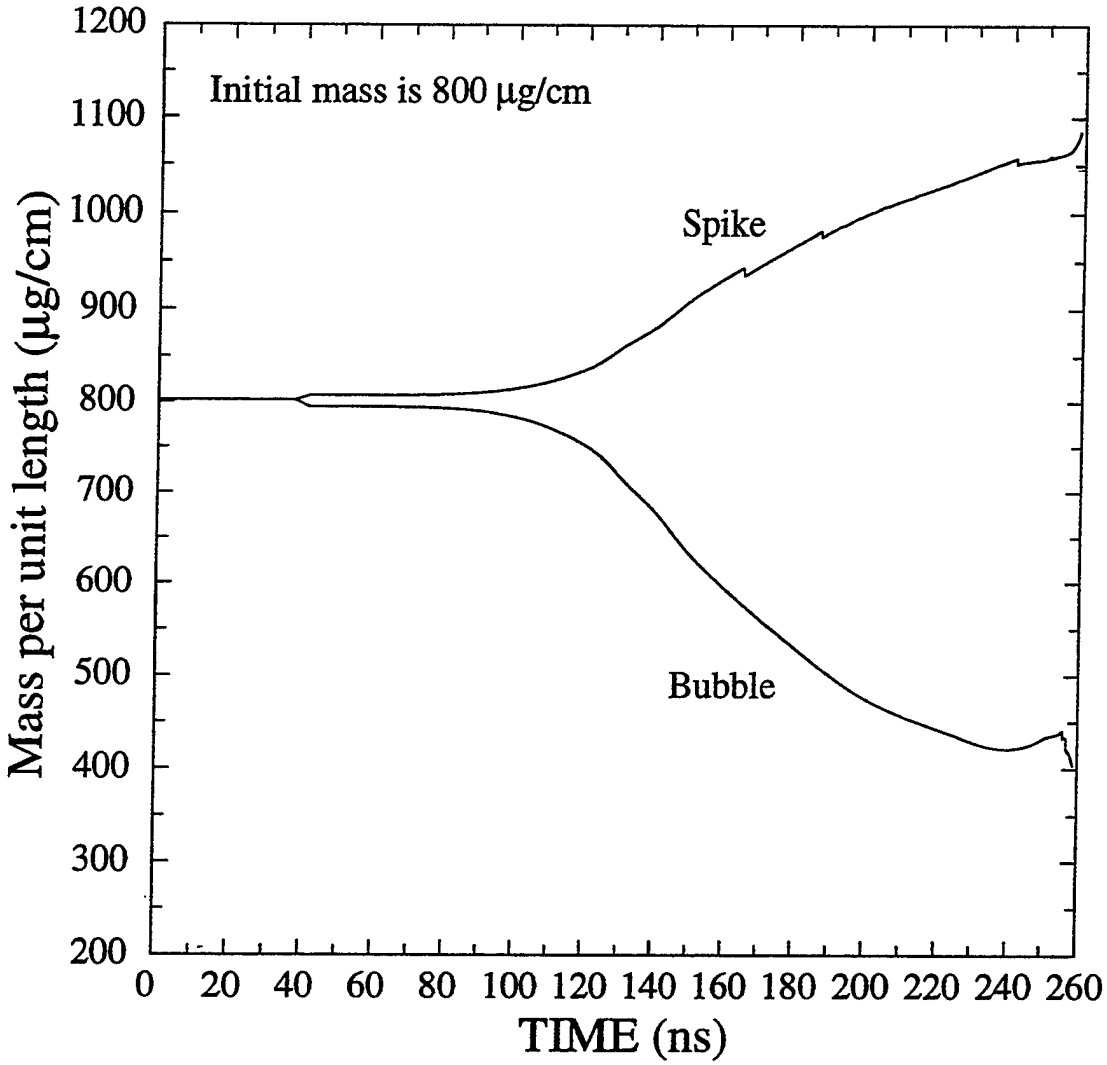

Figure 1. Mass per unit length as a function of time for the spike and bubble regions of the Rayleigh Taylor instability. This is an 800 μg/cm, 3.6 cm radius, uniform density profile load.

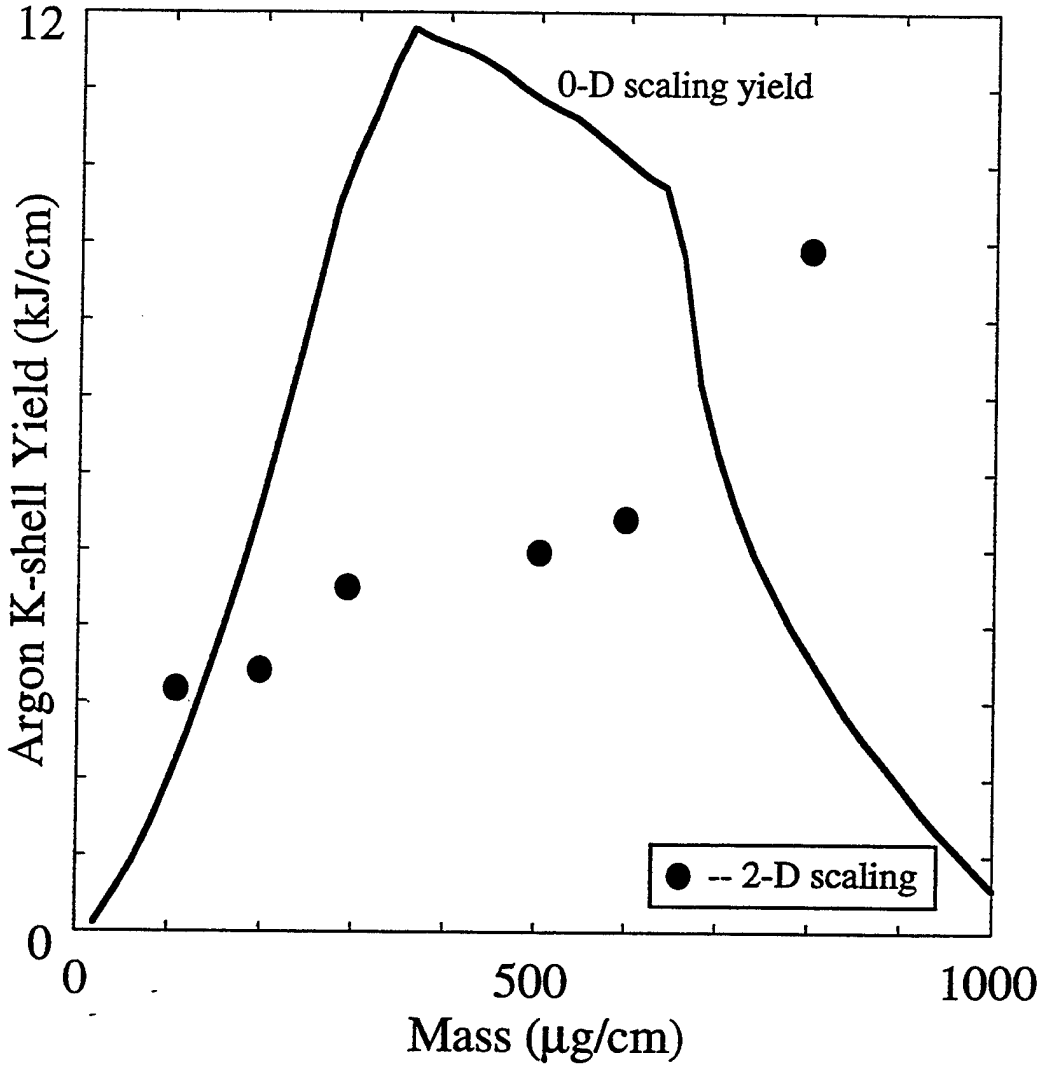

Figure 2. 0D and 2D Argon K-shell yields as a function of mass for a 3.6 cm radius, uniform density profile load that is driven by the Decade Quad emission tolerant design, with oil.

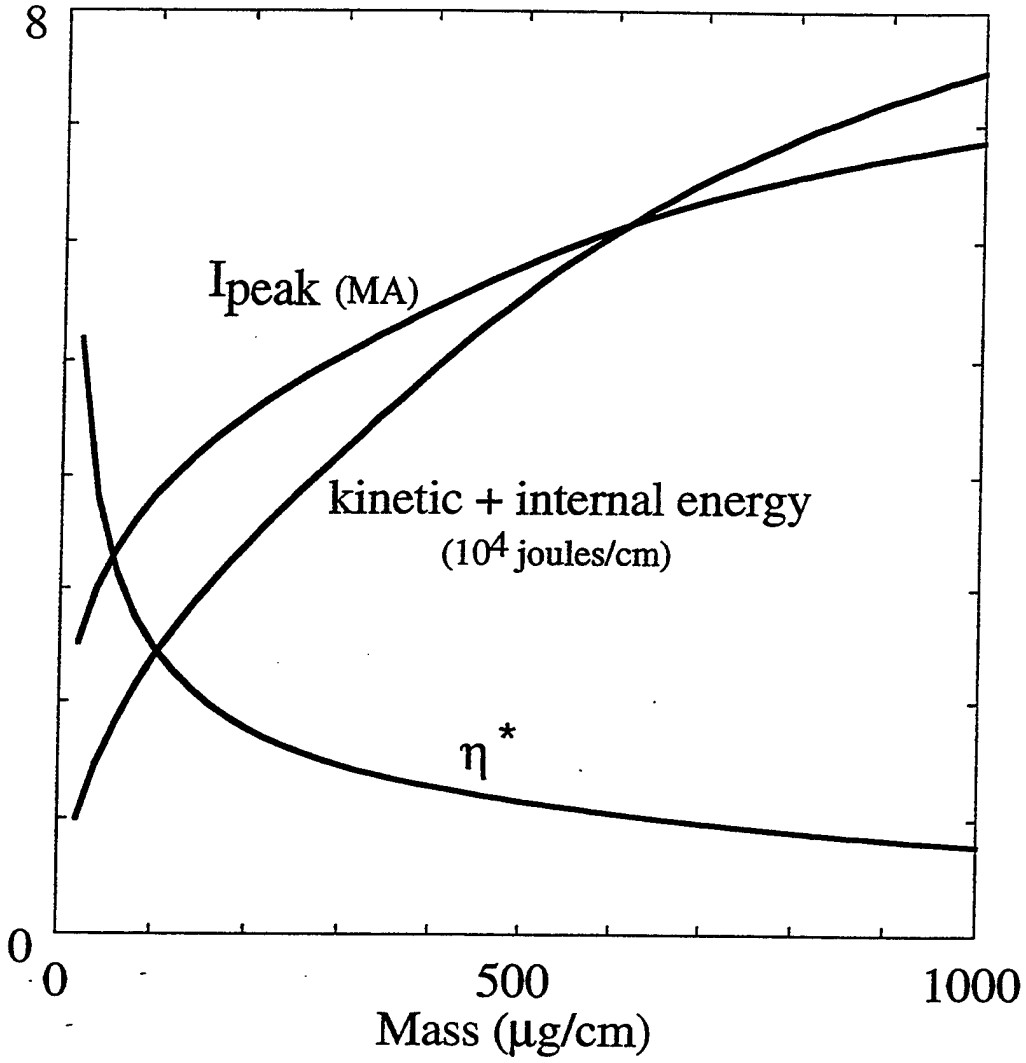

Figure 3. The η^*, energy, and peak currents as a function of mass load. These paramters are calculated from a 0D snowplow model of the 3.6 cm radius, uniform density profile, Decade Quad PRS load.

IV. STABILITY ISSUES OF DECADE QUAD LOADS

We have modeled several DQ (Decade Quad) circuit models to assess the importance of the Rayleigh-Taylor instability (RT) on the performance of two generic loads. The simulated loads were solid fill gas -puffs with an outer radius of 3.6 cm and gas- puff shells with a radius of 2.5 cm. These load radii were chosen such that they have similar implosion times for a given linear mass density. Our purpose in this study was to look at RT stability constraints which are imposed on these loads.

In evaluating the 2-D behavior of these loads, we looked at the projected output which would be predicted with a scaling model applied in 2-D and compare that to the output predicted in a 0-D calculation. In the past, it has been found that 0-D models which use scaling to estimate K-shell radiation output compare well with full radiation 1-D modeling. In large part, this has been due to the fact that the scaling was only obtained after comparison with a large number of detailed 1-D calculations[1]. Because of the low computational cost, 0-D simulations are very useful for making wide ranging parameter studies. In this investigation, we carried this philosophy over to 2-D simulations. The scaling law of Ref. 1, which is used here, estimates the K-shell yield based on kinetic energy, mass, and atomic number when the load radius reaches 1/10 of its initial value. Alternatively, the scaling can be applied when the load inductance reaches the value determined by the return current location and 1/10 the initial plasma radius. In 1-D, it is useful to do the same calculation based on total mass and kinetic energy and compare against the results obtained with full radiation transport. Good agreement is obtained but details of the radiation pulse are missed. In 2-D, we can use the same "cutoff" load inductance to determine when to measure the kinetic energy and apply the scaling law for the radiative yield. The extra dimension, however, also allows a so-called "slice-by-slice"

scaling (i.e., the scaling is applied at each zone or "slice" location along the z-direction) in order to study the effects of non-uniformities along the pinch column. The lumped overall mass and kinetic energy can also be used in the scaling law in order to compare directly to 0-D results for the same load configuration.

Our 2-D code PRISM was used in R-Z geometry. For these calculations, a remapping technique was employed so that the grid always remained orthogonal throughout the simulation. This is necessary in order to follow the distortions created by the RT instability. An equation of state is used and is based on a tabular lookup scheme. The tables were created using the atomic physics packages of the Radiation Hydrodynamics Branch at NRL. Finally, a perturbation was applied to the pinch prior to implosion to seed the RT instability.

Three simple load configurations are shown in Fig. 1. In addition to the shell and uniform fill, a "hollow" fill or fat shell is also shown. Note that for a given linear mass density, the volume mass density decreases from shell to hollow to fill. Figure 2 shows the results for the first DQ design that was studied. This is the DQ "post hole convolute" design with a lumped circuit inductance of 13 nH and an impedance of 0.25 Ohms. Figures 2 (a) and 2(b) show the results for solid fill and hollow shell loads, respectively. The solid lines are the 0-D results for the Argon K-shell yield (Y), peak current (I), and implosion time as a function of load mass.. The open and filled circles represent 2-D simulations which were scaled "slice-by-slice", that is, along individual cuts in z, and as well as with the total mass averaged across the column. Since the "slice-by-slice" scaling tends to emphasize the hottest regions along z, this is also referred to as hot spot scaling. Notice that the mass averaged scaling tends to follow the general form of the 0-D results but at a lower value, while the "slice-by-slice" scaling results remain relatively constant at a lower level and even decline somewhat with masses greater than 300 ugm/cm. In the hollow fill case (Fig. 2(b)), both scaling measures show increased yield with increasing mass, although the "slice-by-slice" scaling only increases slightly after a mass of 300

ugm/cm is reached. For comparison purposes, the 0-D K-shell yield result is shown for a shell load.

A second set of improved Decade Quad (DQ) designs were also simulated with the 2-D code. The circuits for these designs are shown in Fig. 3. These are labeled as the Shlitt conservative design, the emission tolerant with oil, and the emission tolerant without oil. The inductance decreases quite substantially between these designs with the most aggressive/optimistic design, the emission tolerant design without oil, having an inductance of only 11.68 nH. All three designs had a impedance of 0.15 Ohms. Figure 4 shows the results for uniform fill loads where the peak current and K-shell yield are plotted as a function of linear mass density for several 0-D calculations. The number labels correspond to the circuits shown in Fig. 3. It can be seen that there is a dramatic increase in yield between the first two circuits (i.e., design 1 and design 2) and a more modest gain in yield for the last two circuits. The filled circles represent the mass averaged results obtained from the 2-D simulation data. There is an increase in yield from circuit 1 to circuit 3 but the result is not quite so dramatic as in the 0-D results.

Figure 5 shows the results for the 2.5 cm radius shell simulations. As in the previous case, the yield is significantly improved between the three circuit designs. In this case however, the 2-D mass averaged results are not as depressed from the 0-D results as was the case for the solid fill results. All of the yields are above 10 kJ/cm in K-shell yield although they do not approach the near 20 kJ/cm 0-D result of the most aggressive DQ circuit.

All of the results are summarized in Fig. 6, where the K-shell yields are plotted against the peak current reached in the calculation. Also shown for comparison are results from two 2.25 cm fill cases. These were included because the RT instability effects should be lower for smaller radius loads. The tradeoff is that the peak current which can be achieved during the implosion is also diminished. The yields for the shell loads are seen to be almost double that of the fill loads. In the solid fill loads, however, both circuits 2 and 3

reach peak values greater than 5 MA while only circuit 3 is above the 5 MA peak current value level for the shell load implosions. It is apparent that even when 2-D motion is considered, the shell loads are still better radiators, at least at these radii where the RT instability does not completely destroy the plasma column.

The effects of the instability on the two loads are illustrated in Fig. 7. The contours of the uniform fill load near stagnation imply a relatively uniform profile in the z-direction for the first 0.5 cm. At z = 0.5 cm, a spike is evident and then a smaller uniform area up to z = 1.0 cm. The density profile for the shell load shows more disruption but there are still small uniform regions which are good radiators and the ratio of axial to radial kinetic energy is small. The spike region is also less expansive so that the region from 0.5 cm to 1.0 cm is very uniform. This profile has enough uniformity that the scaling predicts a yield which is twice that of the uniform fill load (see Fig. 6).

Table I shows the implosion times for the various simulations compared with the implosion times of 0D/1D implosions. Also shown are the 0D/1D K-shell yields. The time differences for the 2-D fill implosions compared to the 0D scaling runs are roughly 20 ns for all of the designs. This increases to a time difference of about 25 ns to 30 ns for the shell implosions. Note that the initial radii for the shell and fill loads were chosen such that the implosion times for a given circuit would be equal. This ensured that both loads had roughly the same driving current during the implosion. The implosion time results for the smaller radii (i.e., 2.25 cm) uniform fill loads are also shown in the Table.

As expected, these results show that two-dimensional effects limit the yield when compared to the 0-D/1-D results. The effect appears to be more important for larger diameter loads, i.e. the 3.6 cm radius uniform fill loads. The tradeoffs between stability, load radius, and load design appear to favor the 2.5 cm shell loads. These implosions produced about twice as much as the 3.6 cm uniform fill loads. Previous results[2,3] have shown that the inner surface of the load needs to be within about 2 - 2 1/2 cm. Therefore, the results reported on here appear to be consistent with the earlier results.

Figure 8 shows the density contours for a calculation which was initialized with a more realistic density profile provided by Hylton Murphy (Fig. 8a) of Maxwell Laboratories, Inc. The DQ circuit was the Schlitt conservative design. The perturbation is initialized with four bubble and spike regions along a 1 cm length in the z-direction. Instability growth can be seen in the regular bubble and spike formation in the second plot. This growth continues until the outside of the pinch reaches the initial point of maximum density at a radius 2.25 cm. After this point, the instability develops more rapidly and subsequently the pinch column is disrupted. This behavior is consistent with the fact that plasma is accumulated in the shell during the initial phase of the implosion before the location of peak density is reached. This process reduces the acceleration and lowers the RT growth rate. After the peak density has been reached, the acceleration increases rapidly as less and less additional mass is accreted onto the shell. The increased acceleration results in a larger RT growth rate which is followed by a rapid disruption of the pinch as is seen in the profile of Fig. 8(c). The same calculation was also done with a random perturbation seed rather than a single mode perturbation. The density profiles from this run are shown in Fig. 9. The same behavior is evident in that the instability rapidly breaks up the shell after the radial point of maximum density has been reached. The maximum and minimum line densities are also plotted as a function of time. From about 100 ns to 150 ns the growth is exponential as evidenced by the linear portion of the maximum density curve (note that the density scale is logarithmic). After 170 ns, the rapid decrease in the minimum density and rapid increase in maximum density signify that the pinch has broken apart. These simulations demonstrate the danger of using shell loads at a large diameter. The instability growth is tolerable before the shell is fully formed because of the deceleration effect of mass accumulation. After all of the mass has been accumulated and the shell begins the high acceleration implosion phase, the RT instability will destroy the shell if the runin radius is large enough. Previously, we have shown that shell radii greater than 2 cm

for fast rising currents are prone to disruption. This criteria on radius is increased for broader profiles (i.e., uniform fills)

FIGURES

TABLE

REFERENCES

1. J. W. Thornhill, K. G. Whitney, J. Davis, and J. P. Apruzese, J. Appl. Phys. **80**, 14 (1996).
2. F. L. Cochran, J . Davis, and A. L. Velikovich, Phys. Plasmas **2**, 2765 (1995).
3 A. L. Velikovich, F. L. Cochran, and J. Davis, Phys. Rev. Lett .**77**, 853 (1996).

Simple Load Designs

$\rho_S > \rho_H > \rho_F$

SHELL

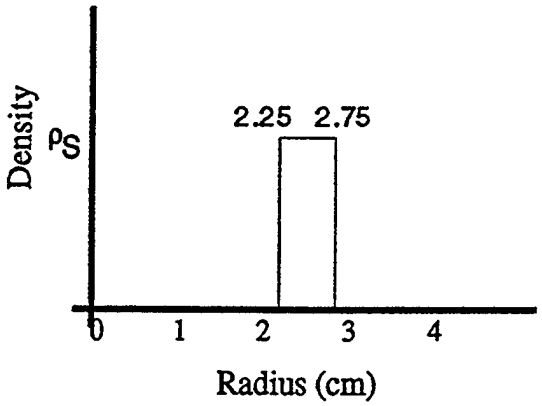

HOLLOW FILL

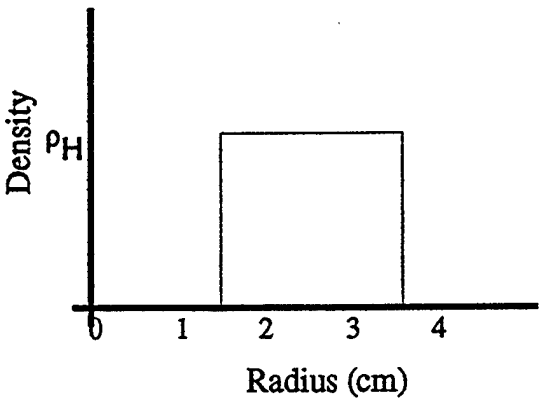

SOLID FILL

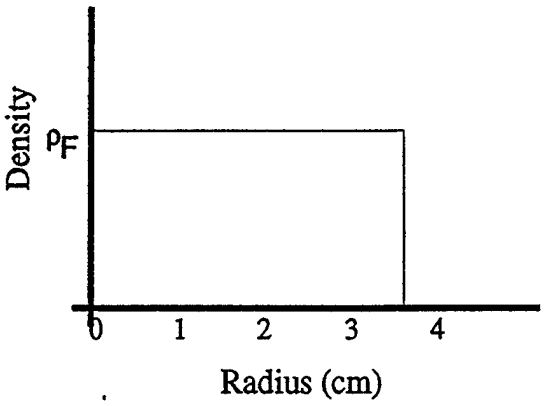

Figure 1

DQ Post Hole Convolute Design

Solid Fill Loads

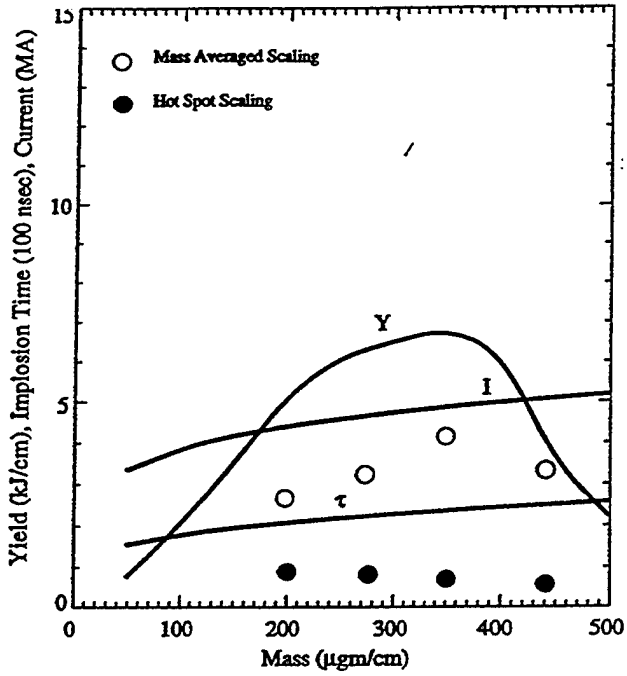

(a)

Hollow Fill Loads

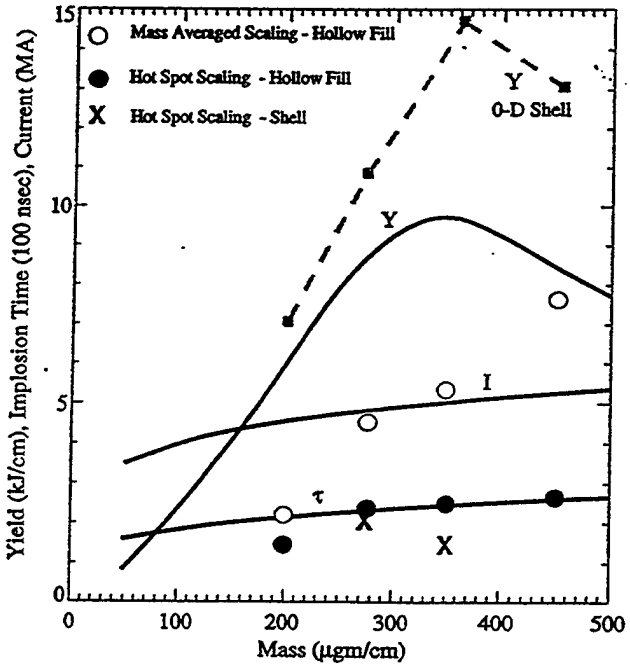

(b)

Figure 2

Decade Quad Equivalent Circuit

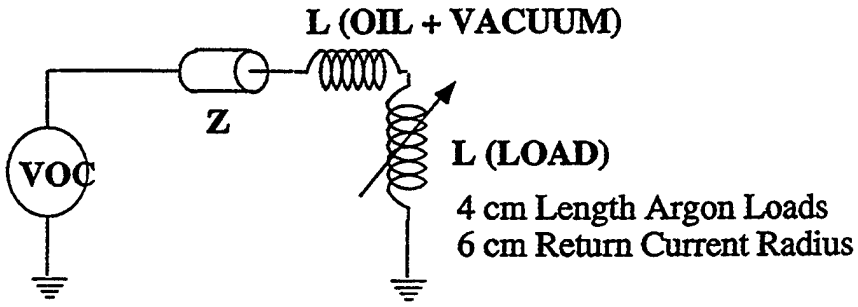

Circuit 1: L = 36.0 nH R = 0.15 ohms Schlitt Conservative Design

Circuit 2: L = 22.97 nH R = 0.15 ohms Emission Tolerant Triplates With Oil

Circuit 3: L = 11.68 nH R = 0.15 ohms Emission Tolerant Triplates Without Oil

Figure 3

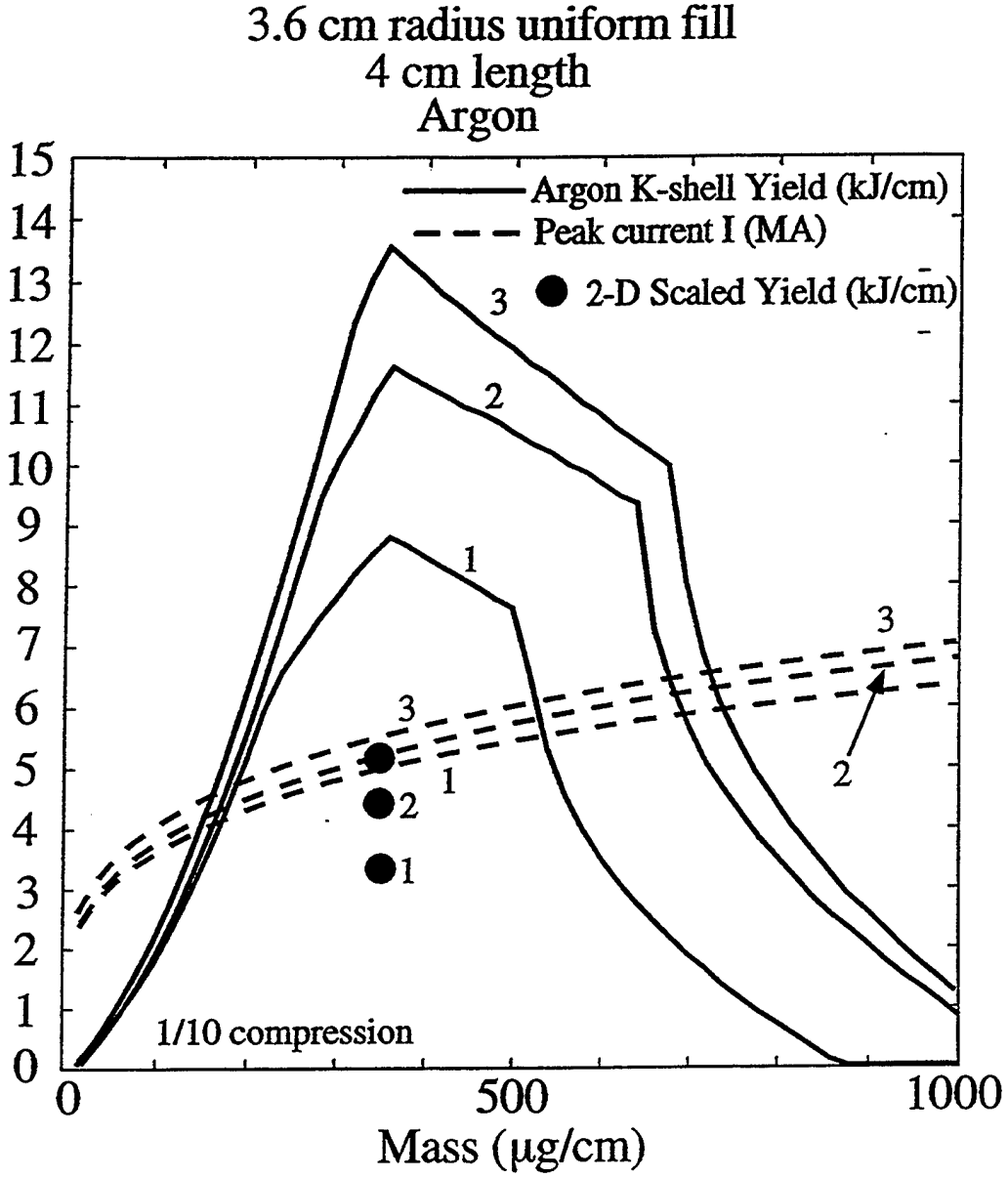
3.6 cm radius uniform fill
4 cm length
Argon
Argon K-shell Yield (kJ/cm)
Peak current I (MA)
2-D Scaled Yield (kJ/cm)
1/10 compression
Mass (μg/cm)
0
500
1000
15
14
13
12
11
10
9
8
7
6
5
4
3
2
1
0

Figure 4

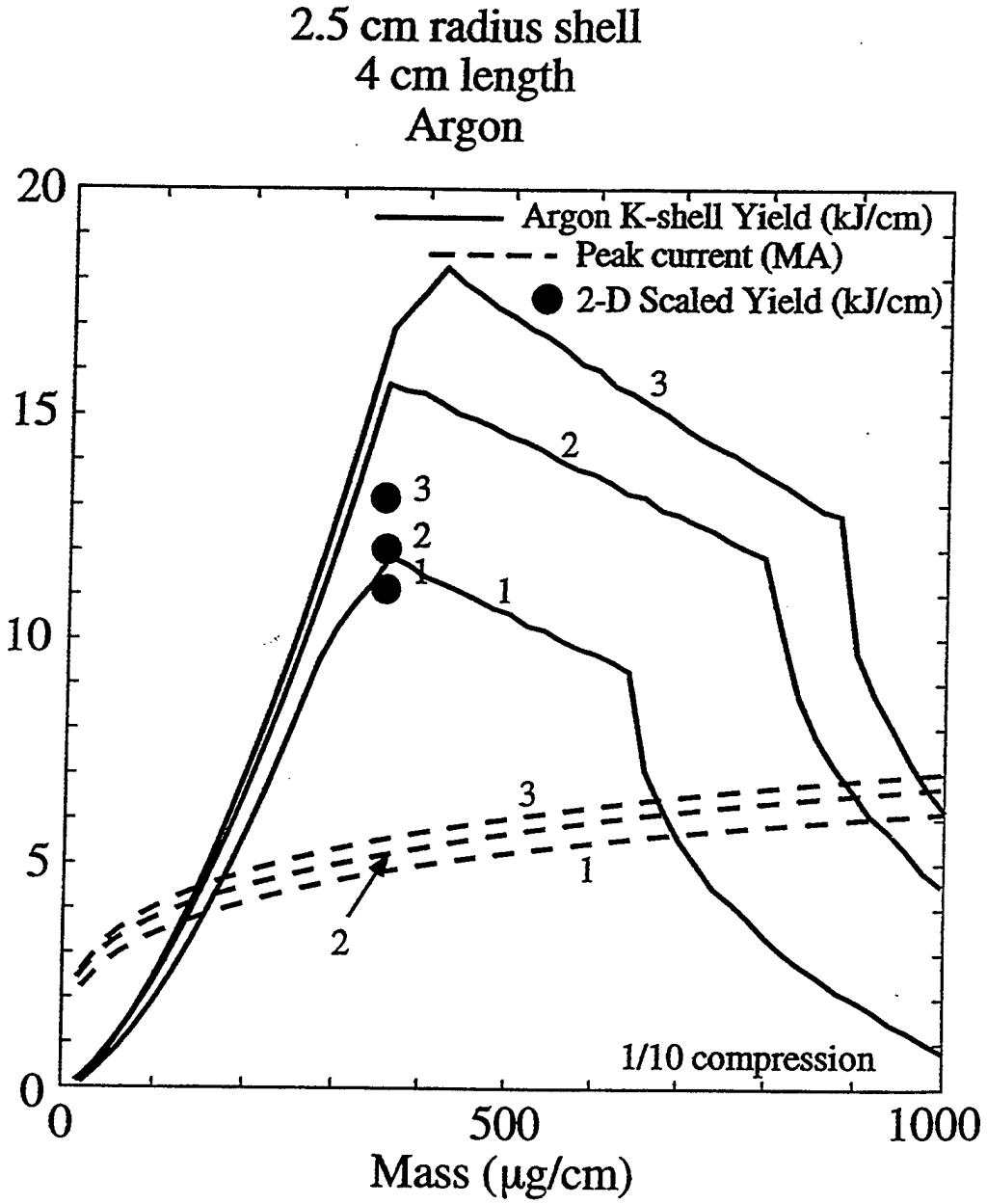
2.5 cm radius shell
4 cm length
Argon
Argon K-shell Yield (kJ/cm)
Peak current (MA)
2-D Scaled Yield (kJ/cm)
20
15
10
5
0
0
500
1000
Mass (μg/cm)
1/10 compression
1
2
3

Figure 5

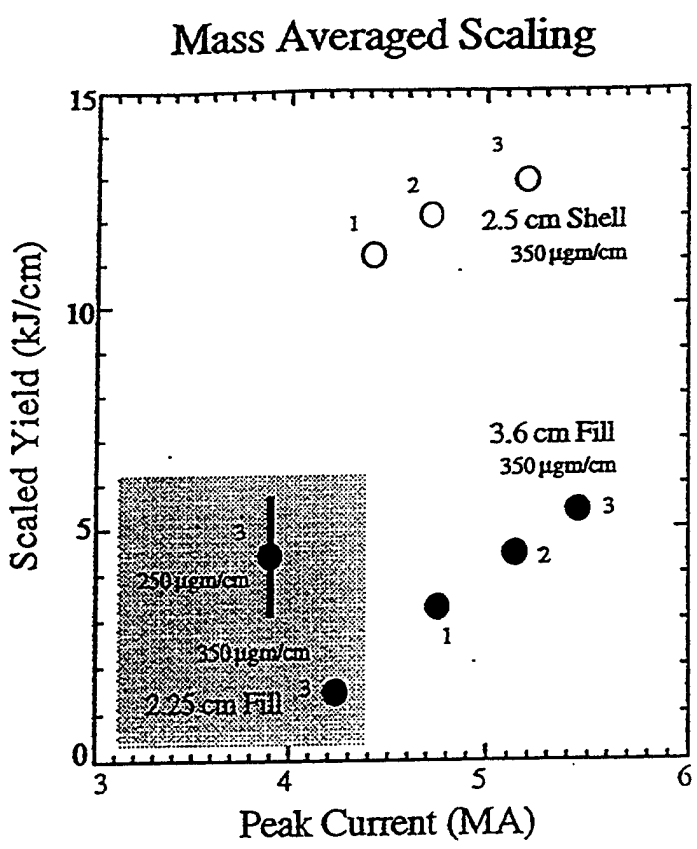
Mass Averaged Scaling
Scaled Yield (kJ/cm)
Peak Current (MA)
2.5 cm Shell
350 µgm/cm
3.6 cm Fill
350 µgm/cm
250 µgm/cm
350 µgm/cm
2.25 cm Fill

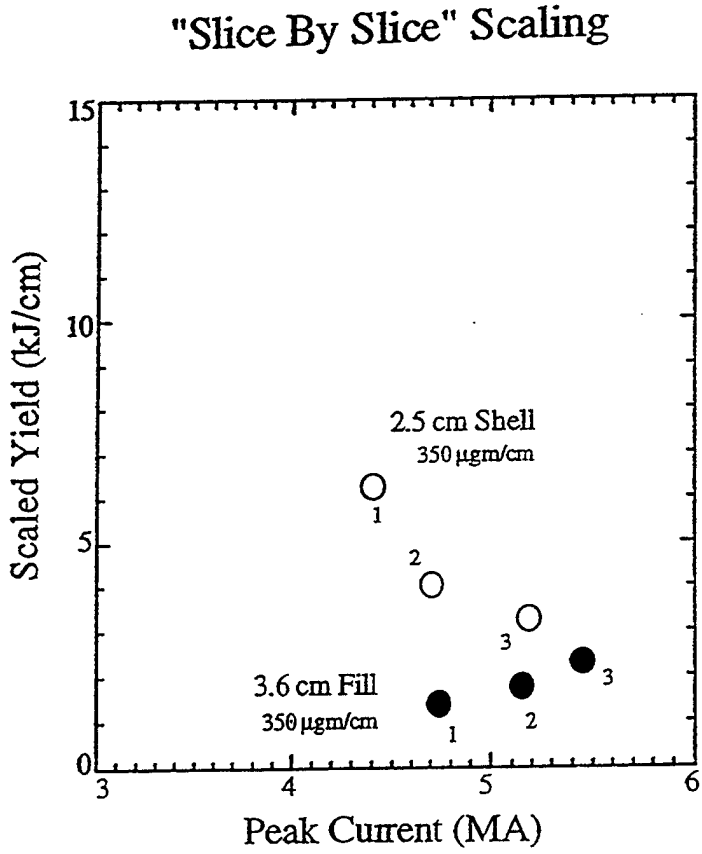
"Slice By Slice" Scaling
Scaled Yield (kJ/cm)
Peak Current (MA)
2.5 cm Shell
350 µgm/cm
3.6 cm Fill
350 µgm/cm

Figure 6

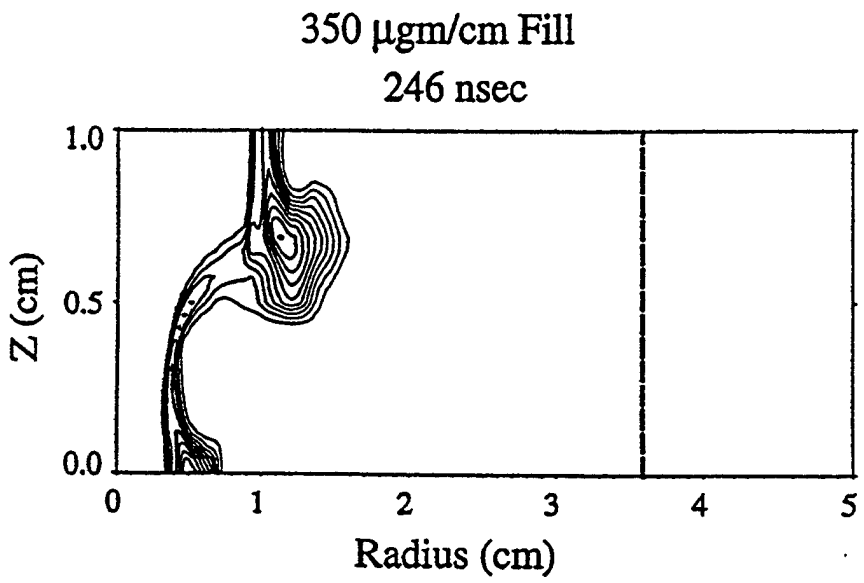
350 µgm/cm Fill
246 nsec
1.0
0.5
0.0
Z (cm)
0
1
2
3
4
5
Radius (cm)

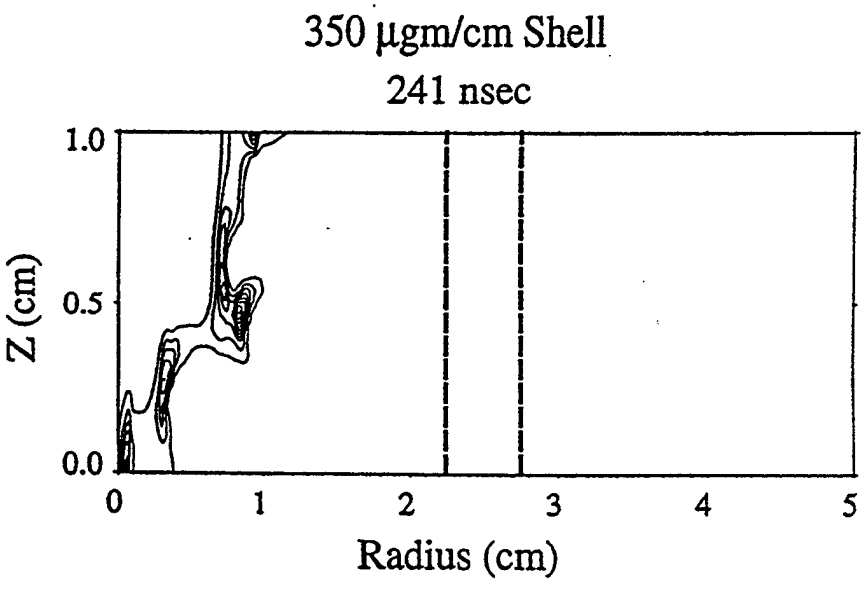
350 µgm/cm Shell
241 nsec
1.0
0.5
0.0
Z (cm)
0
1
2
3
4
5
Radius (cm)

Figure 7

Density Contours

Single Wavelength Perturbation

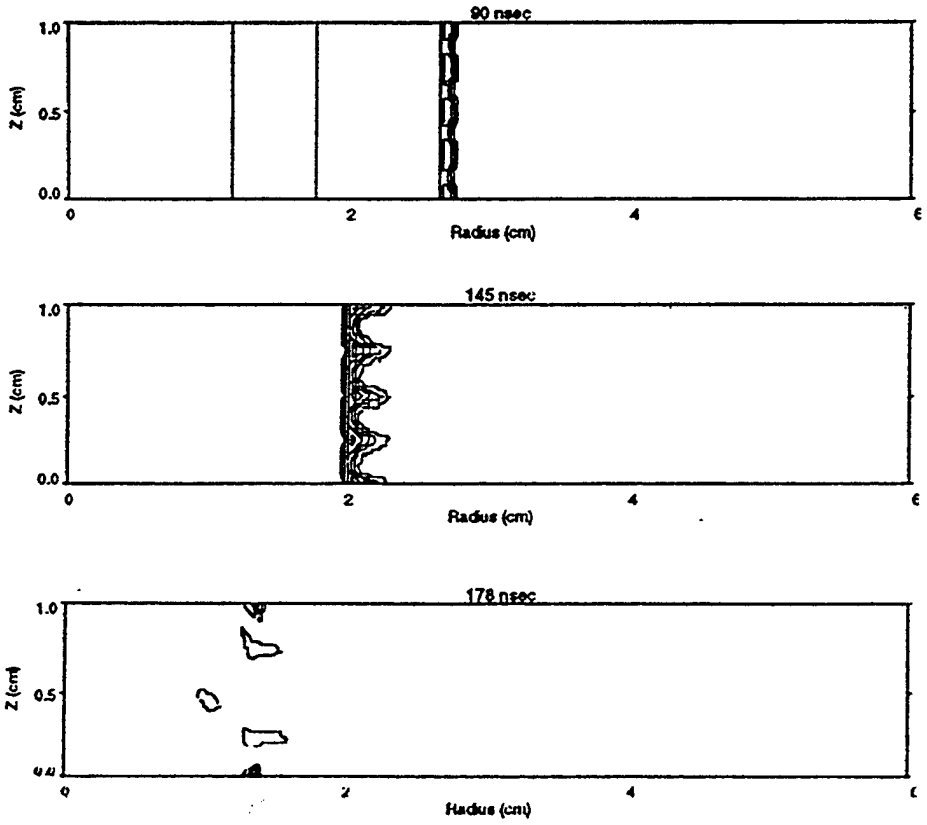

Initial Density Profile

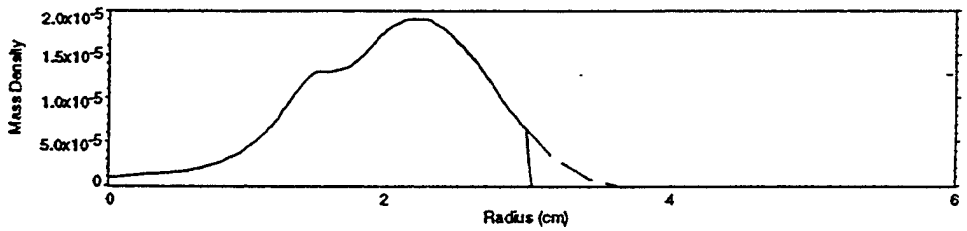

Figure 8

Density Contours

Random Perturbation

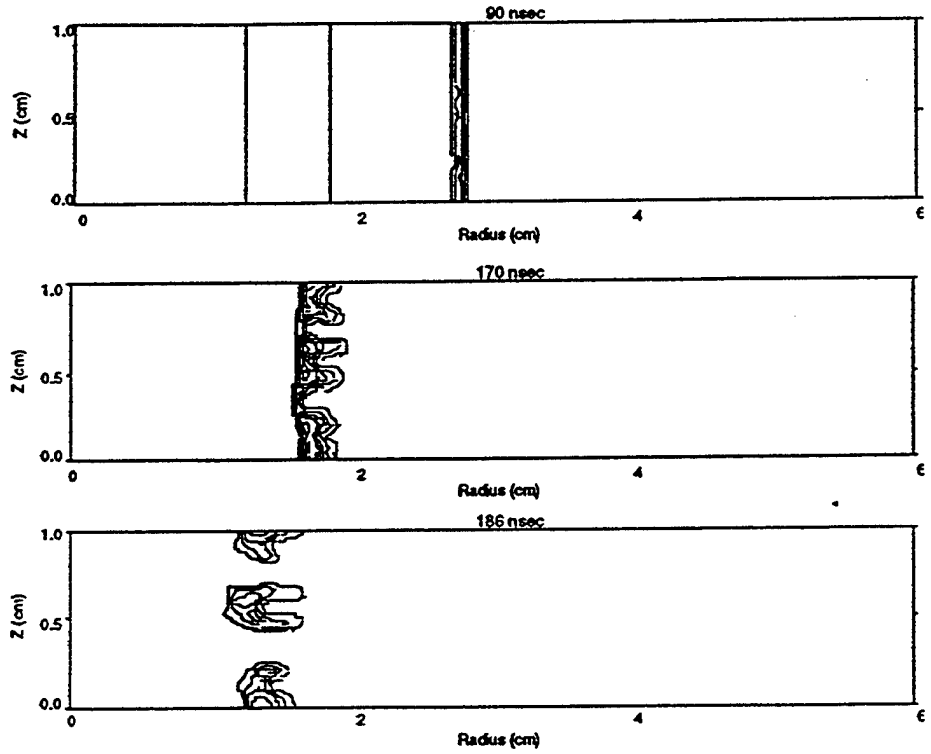

Line Densities

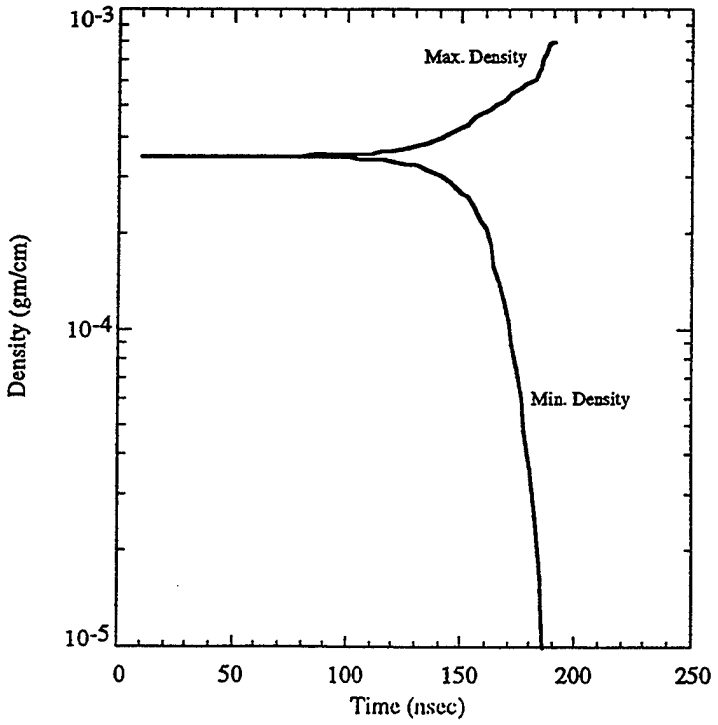

Figure 9

Initial Mass μgm/cm	Load Type	2D * Implosion Time (nsec)	0D/1D Implosion Time (nsec)	0D/1D Yields (kJ/cm)
350	Fill Circuit 1	214	235	8.9
350	Fill Circuit 2	189	219	11.5
350	Fill Circuit 3	173	195	13.5
350	Shell Circuit 1	209	232	13
350	Shell Circuit 2	175	217	15.5
350	Shell Circuit 3	165	197	16.5
250	Fill Circuit 3 - 2.25 cm	144	152	2.8 - ?
350	Fill Circuit 3 - 2.25 cm	152	164	1.45 - ?

* 2D implosion time based on inductance of 1/10 radius as measured in 1-D. Adjusted to match 0-D intital time by subtracting 34 nsec.

Table I

V. STABILIZED Z-PINCH LOADS WITH TAILORED DENSITY PROFILES

Stabilization of imploding PRS Z-Pinch loads against the Rayleigh-Taylor (RT) instability is particularly important for long implosions from large radii. The number of e-foldings during the runin phase is known to be proportional to the square root of the pinch radius. The RT instability was not an important issue for implosions from 1-2 cm radii such as those on Double Eagle. However, this instability becomes increasingly detrimental for load configurations which have increased initial radii requirements in order to satisfy the optimal matching of the pinch to a given pulsed power driver. The most powerful drivers are more often than not best matched to longer implosions. For example, the optimal radius of the uniform fill load to produce argon K-shell radiation on the Z device at Sandia is about 4 cm.

To keep the RT instability under control, some of the energy must be sacrificed which otherwise could be made available for conversion into usable radiation. The initial pinch radius can be smaller than the optimal value or the current pulse can be shortened. In either case, some kinetic energy has to be traded for better stability.

We have studied an alternative way of mitigating the RT instability, which has the potential of providing a better trade-off between stability and efficiency. Our goal is to stabilize long implosions from large radii. One method which we have suggested to achieve this goal is to tailor the initial Z-pinch density profiles in both the radial and axial directions. The hydrodynamic mechanisms that provide stabilization are features of the structured shock-magnetic piston flow, as opposed to a uniform acceleration of an imploding plasma shell by the pressure of a magnetic field. This stabilizing effect, like any other, comes at a price. The presence of a converging shock wave generally decreases the

magnetic-to-kinetic energy conversion efficiency. A thin cylindrical shell imploded by magnetic pressure provides efficiency close to 100%. For a cylindrically converging shock wave, this value is decreased, being lowest at early times and then increasing to 85-90% at higher compression ratios. Axial density tailoring tends to further reduce the efficiency, involving some mass loss issues in the course of implosion. The benefit, however, is that the radius and implosion time can be better made to match the parameter of the pulsed power driver. If the next generation of pulsed power facilities require larger radii and longer implosions, this might be the only way to achieve this match. Fortunately, higher power translates into the ability to drive larger masses, and therefore provides more opportunities for load density tailoring. Target manufacturing constraints may also be reduced because low density foams and gels may be used.

In our earlier work[1] we studied the role of radial density tailoring in a cylindrical Z-pinch. We demonstrated that the RT instability growth is suppressed and a nearly uniform annular shell can be assembled on axis while the current is still increasing. Stabilization is caused by the fact that the acceleration of the magnetic field/plasma interface is inverted while the converging shock wave slows down and is being driven into increased density. The interface feels deceleration, and the small perturbations in its vicinity tend to oscillate rather than grow exponentially.

A radially tailored density profile operates as a current switching device. Without it, the load would either implode too early or be greatly distorted in flight . Once the uniform annular shell is formed and starts to implode, it experiences a regular RT instability. This places an upper limit on the initial radius. Practically, the annular shell could not be safely imploded from a radius exceeding 2 cm, so that the initial center-of-mass radius of the radially tailored load could hardly be larger than 4 cm. This, in turn, limits the current pulse duration at the level of 300 ns. Additional schemes which might lead to enhanced stability are needed if larger initial radius loads and longer implosion times are to be considered.. One attractive opportunity is provided by axial density tailoring.

Mitigation of the RT instability by axial density tailoring was discovered at Sandia[2]. It was demonstrated that hourglass-shaped uniform fills turn out to have a remarkable mitigating effect on the RT instability. This effect was shown to be related to the sheared axial mass flow along the outer edge of the load. It appears that this stabilizing mechanism is a rather unexpected manifestation of an effect which is well-established in hydrodynamics. As known since the 1950s, the development of a single-mode RT instability produces a smooth bubble rising at a constant speed and a sharp spike falling with a constant acceleration. The bubble evolves to a steady state and becomes stable due to the lateral flow of the fluid along the bubble surface. There is no exponential instability of either the bubble surface or rise velocity, both of which are little changed during this process[3].

The RT instability develops in the fluid which flows past the bubble interface and is subsequently dumped to the spike before any appreciable growth can take place. For a subsonic, uniformly accelerated plasma shell, the stable bubble is simply a hole punched in the shell, destroying its integrity. A different situation is realized with supersonically accelerated uniform fill Z-pinch loads. Here, a shock wave is driven ahead of the rising bubble and, consequently, there is a relatively uniform and stable layer of accelerated plasma between the interface and the shock front. This layer flows along the interface (which keeps it stable) and is constantly replaced by new plasma entering the flow through the shock front. The penalty for maintaining stability during acceleration is the mass loss due to the plasma flow through the accelerated layer. The above considerations might open an attractive opportunity for designing instability-free large radius gas-puff or foam Z-pinch loads. The goal of this design would be to produce a stable large-scale bubble with an appropriately curved shape from the very start of the implosion, thus avoiding competition between small-scale bubbles which generate undesirable localized non-uniformities which can degrade the quality of the implosion.

A simple numerical study of such a load configuration is illustrated by Fig. 1. The initial uniform fill Ar load has a parabolic outer boundary extending from r = 8 cm to 11 cm, its line mass, 5 mg/cm, corresponding to an implosion time of about 500 ns for a constant current I = 5 MA. Figure 2 shows the density contours at four different times. At about t = 200 ns, the accelerated bubble appears to break up near the tip. Due to the intrinsic stability of the large-radius bubble, this produces essentially the same bubble, with appreciable mass dumped into the spike (see the density contours for t = 300 and 350 ns). Finally, at t = 435 ns, the mass which accelerated in a stable way near the tip of the bubble stagnates at the axis. This mass does not consist of the plasma that was initially accelerated (this portion of the load is long gone into the spike), but the acceleration of the remaining plasma is nevertheless continuous throughout the implosion. The stagnated mass is a small fraction (less than 10%) of the total initial mass of the load. This is the price paid for the stable acceleration from 8 cm over 435 ns. Figure 3 shows the time histories of max-to-min line densities (a) and, radial and axial kinetic energies (b). The radial kinetic energy at all time remains much greater than the axial kinetic energy. In contrast with a load which only has radial density tailoring, the axial density tailoring could actually mitigate the RT instability (even suppress it completely, at the expense of accelerating a small fraction of the load mass) rather than delay its onset. In a trade-off between stability and performance, it would be natural to combine the two approaches. Radial density tailoring could be used to suppress perturbation growth in the lower-density outer layers of the load during the current risetime, whereas the axial density tailoring would help in slowing down the growth during the time when the load is accelerated by the peak current. To simulate a combined axial-radial density tailoring, we have chosen the Gaussian density profile, $\rho(r,z) \sim \exp[-r^2/R(z)^2]$, where the axial profile, R(z), is similar to that shown in Fig. 1 but shrunk by a factor of 2. For the same total mass as in the above example with a purely axial density tailoring, this choice of parameters effectively decreases the mass-averaged radius by a factor of 2, which means shortening the time of implosion

from 435 ns by $2^{1/2}$, that is, to about 300 ns. The results of this simulation are shown in Figs. 4 and 5. This data is presented in the same form as in Figs. 2 and 3, respectively. Comparing the density contours plotted in Fig. 4 to those of Fig. 2, a much smoother plasma flow can be seen. This simulation suggests the feasibility of this approach to stabilization. More research (in particular, more 2-D simulations with realistic circuit equations) is needed to evaluate the actual benefits provided by this load design in terms of producing useful radiation pulses.

FIGURES

REFERENCES

1. A. L. Velikovich, F. L. Cochran, and J. Davis, Phys. Rev. Lett .**77**, 853 (1996).
2. M. R. Douglas, C. Deeney, and N. F. Roderick, Phys. Rev. Lett. **8**, 4577 (1997).
3 A. Inogamov and A. V. Chekhov, Phys. Dokl. **38**, 32 (1993).

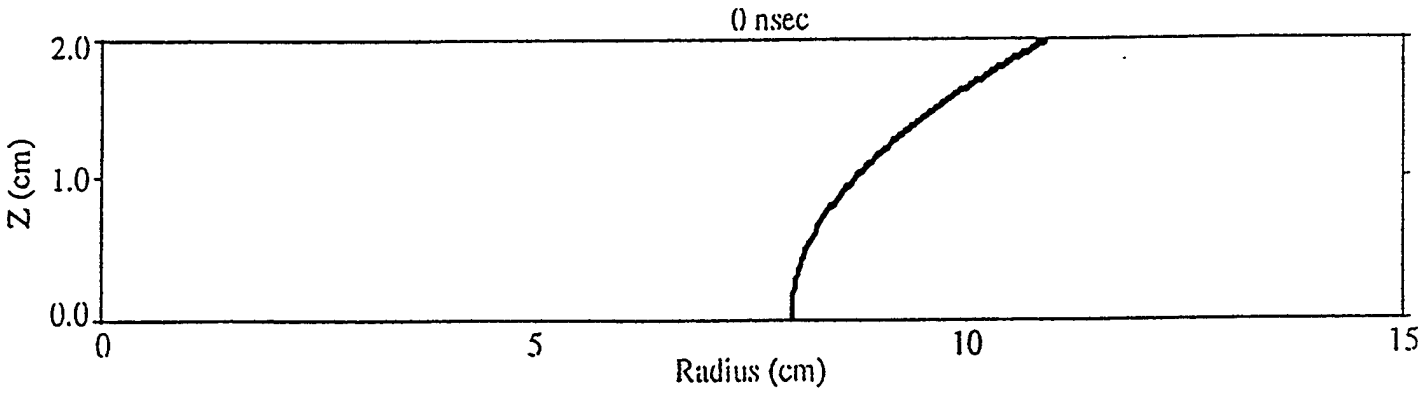

(a)

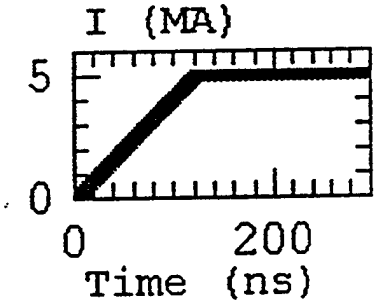

(b)

Figure 1

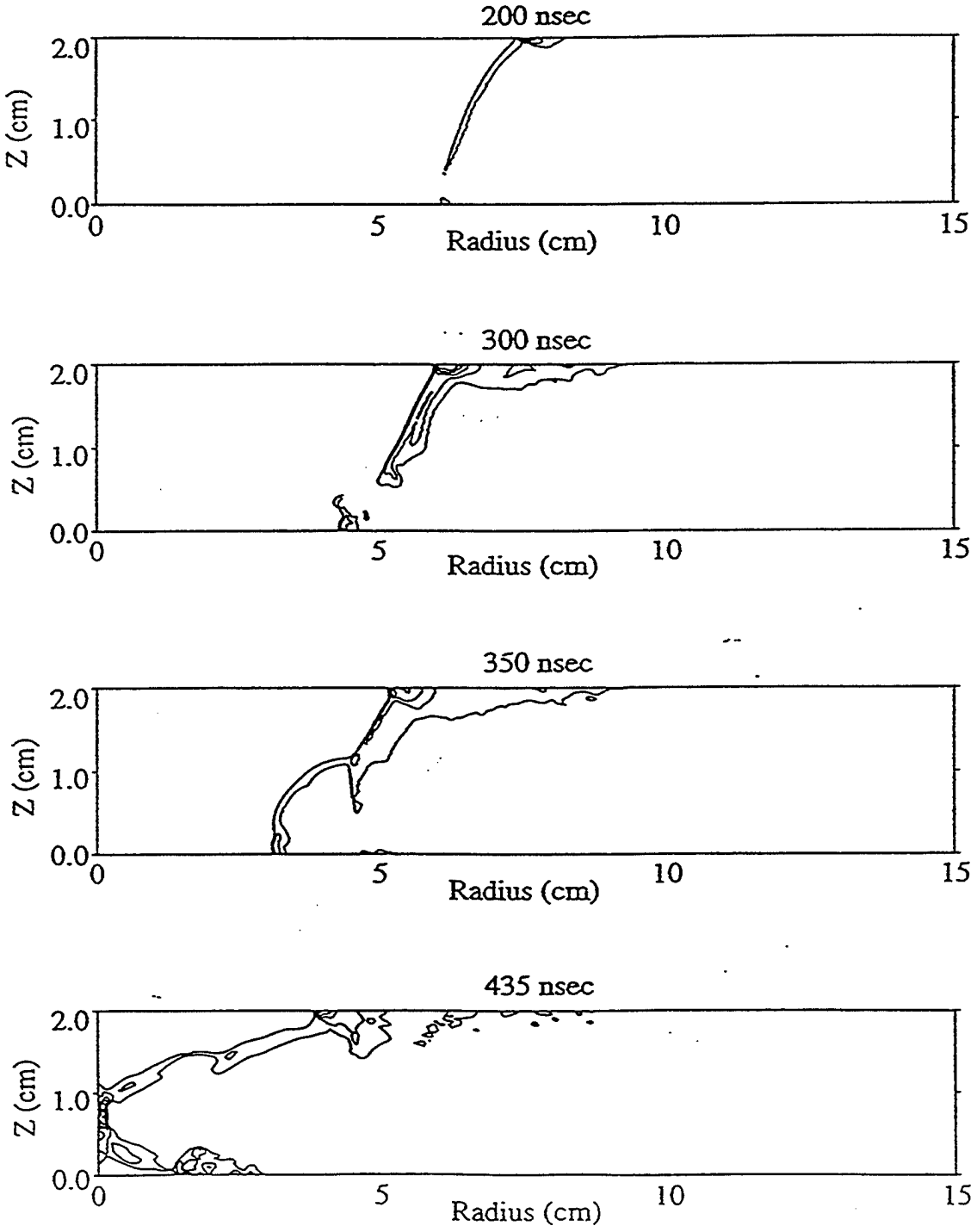
200 nsec
300 nsec
350 nsec
435 nsec
Z (cm)
2.0
1.0
0.0
0
5
10
15
Radius (cm)

Figure 2

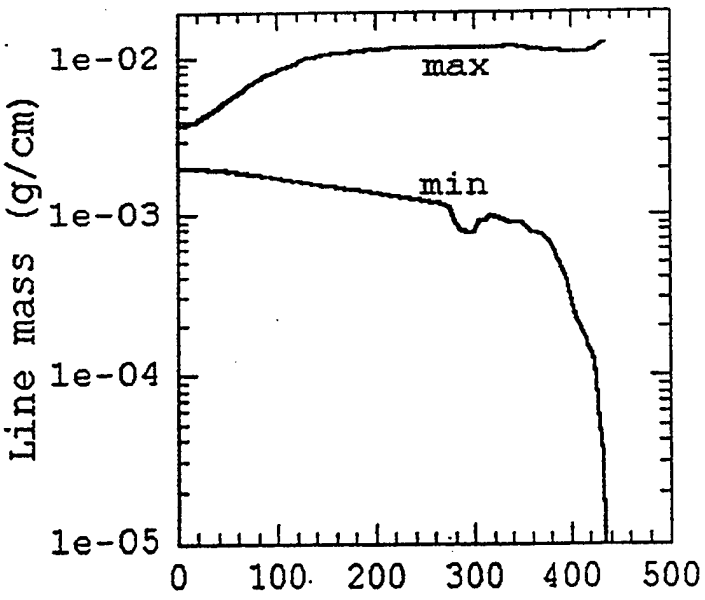

min ≅ bubble, max ≅ spike

(a)

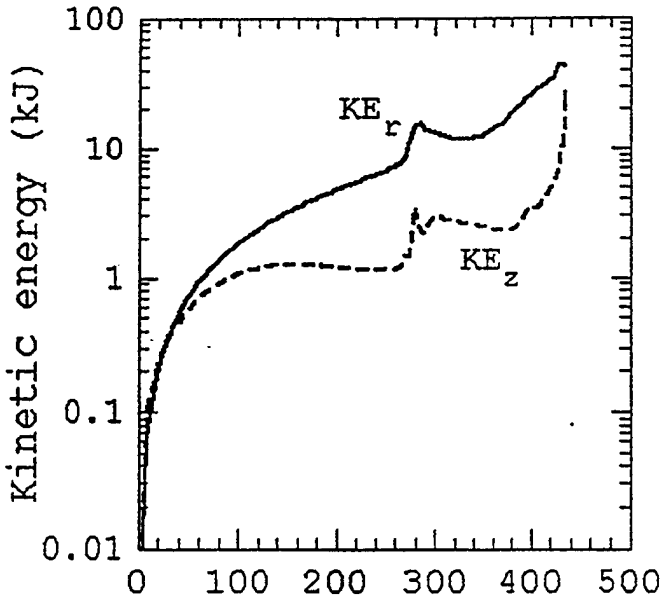

$KE_r >> KE_z$ until the bubble reaches axis at t=435 ns

(b)

Figure 3

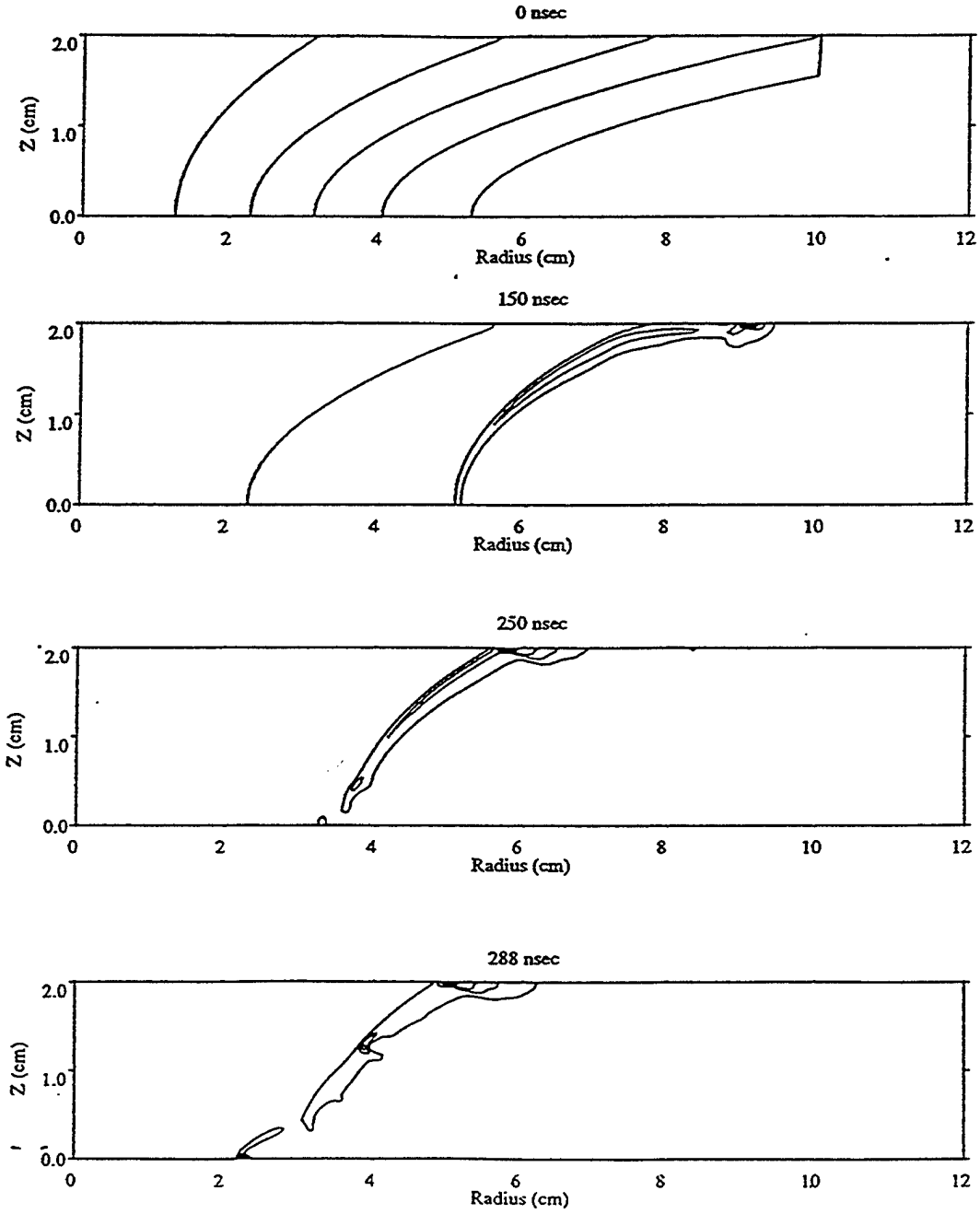
0 nsec
2.0
1.0
0.0
Z (cm)
0
2
4
6
8
10
12
Radius (cm)
150 nsec
2.0
1.0
0.0
Z (cm)
0
2
4
6
8
10
12
Radius (cm)
250 nsec
2.0
1.0
0.0
Z (cm)
0
2
4
6
8
10
12
Radius (cm)
288 nsec
2.0
1.0
0.0
Z (cm)
0
2
4
6
8
10
12
Radius (cm)

Figure 4

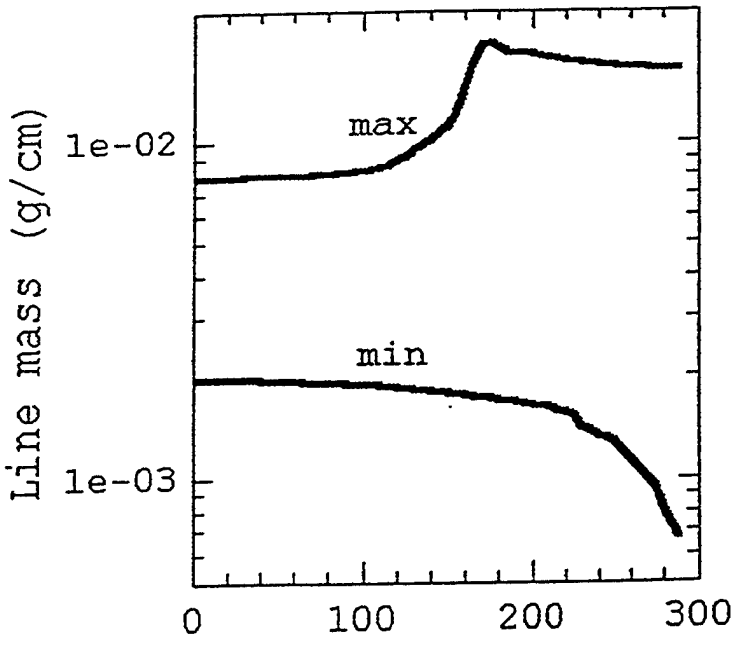

min = bubble, max = spike

(a)

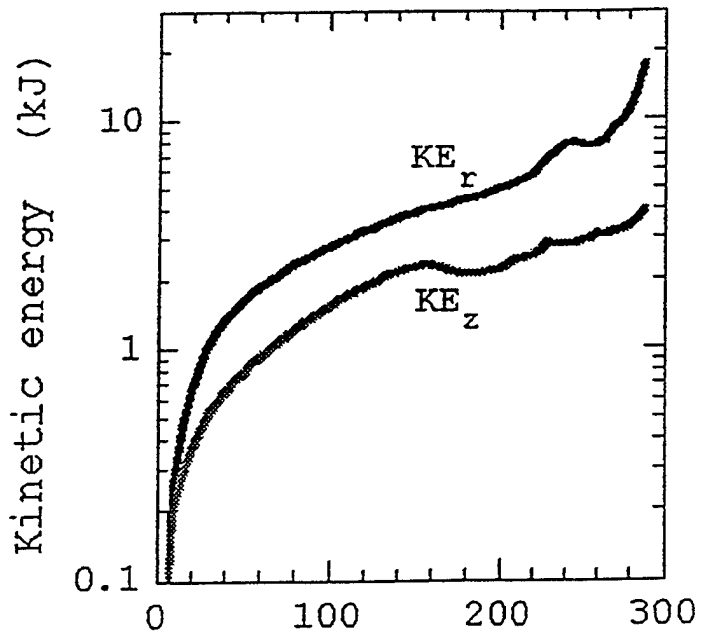

$KE_r >> KE_z$ until the bubble reaches axis at t ~ 300 ns

(b)

Figure 5

VI. ARGON GAS PUFF IMPLOSION PERFORMANCE ON AN AGGRESSIVE DECADE QUAD

A. Methodology

In a manner similar to previous work[1], the active rundown time for a model load is determined by the selection of a minimum radius R_f for the implosion, in contrast to another common choice to measure kinetic energy delivery at a fixed fraction of the initial radius. The kinetic energy coupling generally tracks the change in inductance produced in the load, but that inductance change is fixed if the implosion is followed only to a constant fraction of R_o. By having the slug model (implicitly) undergo transition from an annulus to a cylinder at a prescribed lower radius rather than at a prescribed fraction of the initial radius, this final stagnation radius is a fair measure of the change in inductance achieved and can be explicitly tied to experimental observations. The peak load kinetic energy is therefore recorded at this time of assembly, and is then used to compute the expected yield. Therefore, by selecting absolute values of initial and final radius, a coupling study can get a clearer picture of the correlation between inductance change and kinetic energy delivery.

B. Scaling Law Formulation

The expected K-shell yield per unit length, [kJ/cm], can be written as a function of two parameters. The first

$$\eta \equiv (\frac{v_f}{1.35 \cdot 10^6})^2 \mathcal{Z}^{-2.41}, \qquad (VI.1a)$$

is a measure of the excess velocity over that required to gain access to the K-shell of the element of interest, as calibrated to the atomic number $\mathcal{Z}$. For argon this fiducial velocity is $\approx 4.395 \cdot 10^7$ cm/sec. The velocity argument used is that value characteristic of the implosion as the load starts to stagnate. In a slug calculation with a transmission line code like Screamer, the stagnation process is not explicitly computed so we use the final velocity v_f achieved by the slug as it passes under the fixed minimum radius. The second parameter for the scaling law is

$$\beta = min[\ 0.3\ T_{load}\ ,\ 0.3\ T_{load} \frac{M_{load}}{\alpha(\eta, \mathcal{Z})}\ ] \qquad (VI.1b)$$

where M_{load} is the total mass loading in [g/cm], and T_{load} is the kinetic energy of the load (in kJ/cm) corresponding to v_f. The function

$$\alpha(\eta, \mathcal{Z}) = 2.58 \cdot 10^{-12} \mathcal{Z}^{5.96} \; exp(\frac{20.6}{\mathcal{Z}^{0.9}}) \; max[\, 1, \frac{\eta^2}{\eta + 12} \,], \qquad (VI.1c)$$

measures a mass break point for the transition from inefficient to efficient coupling between kinetic energy and yield. The yield scaling can be formulated piecewise over four η domains

$$Y_K = \beta \quad (1.5 \leq \eta),$$

$$Y_K = \beta[\, \eta - 0.5 \,] \quad (1.0 \leq \eta < 1.5),$$

$$Y_K = \frac{\beta}{2}[\, 1 - \sqrt{4(1-\eta)} \,] \quad (0.75 \leq \eta < 1.0)\,,$$

$$Y_K = 0 \quad (0 \leq \eta < 0.75)\,. \qquad (VI.1d)$$

For a chosen load material ($\mathcal{Z}$) and final radius (R_f), the K-shell yield (Y_K) per unit length (ℓ) can be calculated as a function of the implosion velocity (v_f) and mass loading (M) per unit length. The yield thus depends solely upon the plasma conditions at implosion.

C. Energy Coupling With An Aggressive Design

In previous work, the design characterized as "baseline" was that due to Deeney, Boller, and Schlitt. It represents a configuration using "legacy hardware" in the pulser upstream of the insulator. Such a configuration brings a peak current of about 6.5 MA to an imploding load and, working from an intial 5.0 cm radius, optimizes its kinetic energy delivery at 21.875 mg cm^2 to provide 283.5 kJ to a load experiencing a factor 20 compression.

The selected "aggressive design" is due to Spence at PSI. A line element listing (in Screamer format) is shown in the Applendix. Here the removal of the oil transmission line and the closure of vacuum gaps throughout the line appreciably reduce the front end inducance of the pulser. The coaxial to triplate transition is lower impedance and couples (at a radius of about 70 cm) into a disk triplate with nominal 1 cm gaps. The triplate is convoluted at an inner radius of 10 cm with 16 posts, and further inductance reductions are envisioned for the feed to the PRS itself. To characterize the MITL and convolute, lossy elements are added to the transmission line calculation — a triplate disk MITL and post hole convolute shunt with a fixed value for Z_{flow}.

The MITL representation chosen for this triplate is not particularly emission tolerant, with a turn-on electric field of 10 MV/m, but the general level of magnetic insulation implied by the local voltage and current solution values is nevertheless quite good. As shown in Appendix 2, the disk MITL is segmented into four 0.5 ns lossy elements. Each element closes down in radius and increases its impedance proportionately ($\propto 1/R$), evaluated at the middle of the segment's radial limits. The impedances thus derived are used as a means of bounding the flow impedance assigned to the convolute shunt.

The bounds on flow impedance are well known and can be seen to vary between two limits as the charge in the detached electron flow builds up. In the limit of very little detached current the flow impedance relaxes to the vacuum impedance, but, as the detached flow becomes more important, the flow impedance drops to a value smaller than the vacuum impedance because the charge in the detached flow screens the cathode. In the limit of full space charge limited emission from a cathode, the flow impedance is just half the vacuum value. In particular, let the ratio of cathode charge to anode charge be

$$\frac{Q_{cathode}}{Q_{anode}} = 1 - \epsilon, \qquad (VI.2a)$$

then the ratio

$$\frac{Z_{flow}}{Z_{vac}} = \frac{2\epsilon - 1 + \sqrt{1 - 4\epsilon^2 \mathcal{G}_c}}{2\epsilon}, \qquad (VI.2b)$$

with the quantity $\mathcal{G}_c \equiv V_e V_{anode}/(Z_{vac} I_c)^2$ and $V_e = m_e c^2/2e$=255.5017 kV. Hence $\epsilon \to 0$ implies vacuum impedance, while $\epsilon \to 1$ implies space charge limited emission and a flow impedance slightly greater than or equal to half the vacuum value when $\mathcal{G}_c$ gets large. Since equation II.2b does not determine a current partition I_c/I_a, the value of $\mathcal{G}_c$ is not easily calculated. One common model used to describe the Vlasov equilibrium associated with the detached electron flow is the constraint of pressure balance, viz. $I^2 - c^2 Q^2 = constant, \forall R$ over the radial extent of the electron layer.

Using the pressure balance constraint we can relate the current partition to the assumed charge partition. The relation is particularly simple, $I_c/I_a \equiv Q_c/Q_a = 1 - \epsilon$, when the constant in the pressure balance constraint vanishes. When the constant is nonzero similar

arguments still apply but one must go further to characterize the Vlasov equilibrium in more detail. Now, returning to the impedance ratio above we find,

$$\frac{Z_{flow}}{Z_{vac}} = \frac{2\epsilon - 1 + \sqrt{1 - \frac{4\epsilon^2 \mathcal{G}_a}{(1-\epsilon)^2}}}{2\epsilon}, \qquad (VI.3a)$$

with the quantity $\mathcal{G}_a$ defined as before but in terms of *anode* current only. In order for the impedance ratio to remain real,

$$\epsilon \leq \epsilon_{max} \equiv \frac{1}{1 + \sqrt{4\mathcal{G}_a}}, \qquad (VI.3b)$$

must hold, but there is no *a priori* constraint on the expected charge and current partition within this operating range. In terms of losses downstream at a convolute, the lower the flow impedance, the greater the fraction of detached current and the worse the losses.

The application of this result in detail to any particular MITL requires a lot of data and theory to assess the anode voltage, cathode current and charge in the detached flow for all points upstream of the convolute point. Rough estimates for $\mathcal{G}_a$ from Screamer solution parameters indicate that it is small ($6.9 \cdot 10^{-3}$), but the ratio ϵ is quite dependent on time varying emission results and local field quantities. The general behavior of disk feeds is to establish a flow impedance about equal to the lowest line impedance in the vicinity of the starting point for the detached flow. As the power further converges to smaller radius and higher impedance, the detached flow retains a imprint of its emission point and that lowest flow impedance.

In order to get some limits on the expected convolute losses, the model was run for several fixed values of Z_{flow} varying from the half the lowest disk feed impedance to the highest disk feed impedance. The selection is guided by the analysis above in that, by varying the expected emission point of detached flow along the radial feed, it spans the worst and best cases.

At typical well matched implosion scenario for the aggressive design shows several beneficial features, as illustrated in Fig. VI(C).1. First, the PRS current [trace 5] approaches 8 MA, allowing heavier loads to be used and thus ensuring a transition *in Ar* to an efficient coupling domain. Following the early current traces, the MITL current [trace 3] is seen to

insulate within 40 ns or so after the monitor current [trace 2] first rises, in agreement with design expectations. More energy gets downstream of the insulator [trace 6] and more energy enters the load [trace 8], even allowing for a substantial convolute shunt current [trace 4] peaking at 2 MA. The behavior shown for strong convolute losses, is a definite worst case, but even here the energy dissipated in the shunt comes at the expense of energy that would just be reflected in the absence of the shunt and not at the expense of the energy going into the PRS load [trace 9].

Near the optimum 5.0 cm loading for the baseline design, the kinetic energy (413 kJ) delivered to the *same load* by the aggressive design is more than 46 % greater. Moreover, when the mass loading is reoptimized to reflect the larger currents in the aggressive design, the available kinetic energy is improved by almost 100% , as illustrated in Fig. VI(C).2. In contrast to the case of larger mass loads at low radius for the baseline machine, the entire range of masses imploded from 5.0 cm on the aggressive machine retains implosion velocities above the critical value for unit η. Finally, using the aggressive design, the yield expectation for the mass optimized 5.0 cm case would migrate on the previously illustrated K-shell yield surface to the 60 kJ/cm range!

As discussed above, by varying Z_{flow} over the range [0.2Ω, 1.3Ω], the loss impedance spans half the lowest (outer radius) vacuum impedance up to the largest (inner radius) vacuum impedance. Only the lowest Z_{flow} values produced any significant loss of PRS kinetic energy (10 %) and shunt dissipated energy (120 kJ). Even when significant, these convolute losses are being mostly supplied by upstream energy, as illustrated again in Fig. VI(C).3. Here for fixed machine and implosion parameters the shunt current losses increase as Z_{flow} drops, but the energy loss to the PRS is about a factor 3 smaller than the energy dumped to the convolute. Owing to the assumptions laid out above, this is a very pessimistic view of probable convolute losses due to detached current. Because the triplate disk MITL is very well insulated, more detailed calculations will probably show even weaker losses.

The best set of load parameters for kinetic energy transfer was also sought over the domain of variations in the return current cage. Twist produced only moderate kinetic energy gains ($\approx$ 10 %) in the long implosion time, large mass cases. Moreover, near the optimum mass loadings, these gains were not large enough to compete with the best kinetic

energy deliveries obtained with a pure z-pinch, as illustrated in Fig. VI(C).4. The energy variation with twist shows that the cost in terms of kinetic energy given up is well within the range of kinetic energy gained by going to the aggressive design. It also shows that increased cage inductance will not tend to increase the expected convolute losses if they are already small for $N \rightarrow 0$.

Generally the cage twist strategy is going to be most effective in terms of energy delivery for pulsers that exhibit too short a timescale for good coupling to the kinematics of the PRS, and for the Decade Quad this is not a significant factor. If on the other hand, a cage twist can help mitigate Raleigh Taylor and allow the needed large radius implosions, then perhaps the tradeoff is well advised.

The final study to be discussed here is the variation of kinetic energy and pinch length, as illustrated in Fig. VI(C).5 for an otherwise optimized [3 cm] load with a small cage twist [0.5 m^{-1}]. By stretching the same load mass over a longer axial extent, the DQ driver is able to bring more energy to the pinch [trace 1] and improve the implosion velocity [trace 3]. Apart from the obvious problems associated with RT stability in a longer pinch, a second caveat with respect to this strategy is the fact that the kinetic energy per unit length [trace 2] actually drops throughout the sequence. The implied yield from such a variation thus might actually *decrease.*

These results were communicated to Deeney at Sandia, and a similar study[2] for PBFA-Z confirms these expectations. The theoretical calculation was performed with an equivalent circuit, rather than a full model, but shows a very similar dynamic range in specific kinetic energy and overall energy delivery. The experimental study shows that shorter pinch lengths translate into a rather higher relative improvement in x-ray power. Such behavior would be expected insofar as shorter pinch lengths also contributed to a more coherent assembly of the load at stagnation.

D. Conclusion

The primary upper limit on yield from the conservative Schlitt design was excessive front end impedance. Even without adding the losses from the post hole convolute and MITL feeds, the best expected Ar K-shell yield was perhaps 15 kJ/cm. From previous work

we know that improvement strategies are more numerous if large radius operation can be obtained, but a second important option is access to a lower impedance front end.

With loss processes and a detailed front end configuration included in the model, it is clear that the more aggressive, low impedance front end is amply justified in terms of performance. One finds nearly twice the available load kinetic energy, a minimal vulnerability to MITL and convolute losses, and ample parameter space for RT mitigation strategies. The survey of twisted cage loads shows that these strategies should be examined primarily for stability rather than for better energy coupling. Pinch length variations, on the other hand, may play a useful role in improving implosion velocity (η) or output power once an interesting operating point is found with respect to mass and kinetic energy.

In view of the foregoing observations, the Decade Quad reinforces a clear requirement to explore, understand, and remediate the Rayleigh Taylor instability so that longer run down lengths can be used. For the proposed device to operate well in any configuration examined here, initial implosion radii must already be pushed into somewhat uncharted territory. Moreover all approaches to a better position on that yield surface must involve a focus on operation from at least 5.0 cm, with greater radii producing diminishing relative energy improvements.

References

1. NRL Memo Report 6721–97-7912, p.95.
2. C.Deeney, private communication.

FIG. VI(C).1 AGGRESSIVE DESIGN IMPLOSION WAVEFORMS: Z pinch, 21.875 mg cm^2 from 5.0 cm

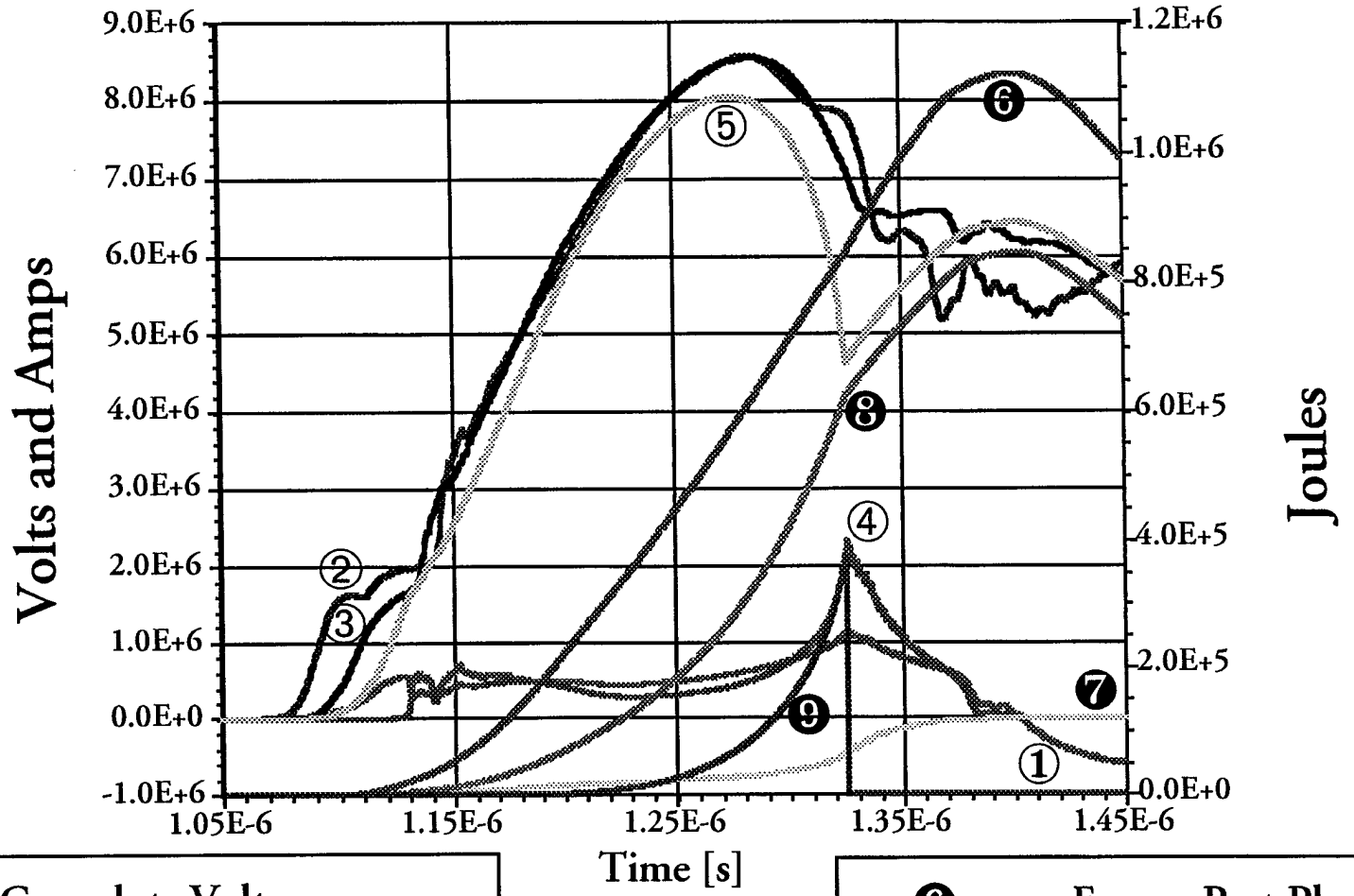

Fig. VI(C).2 Baseline vs Aggressive DQ Performance

— energy variation with m R_0^2 at 5.0 cm]—

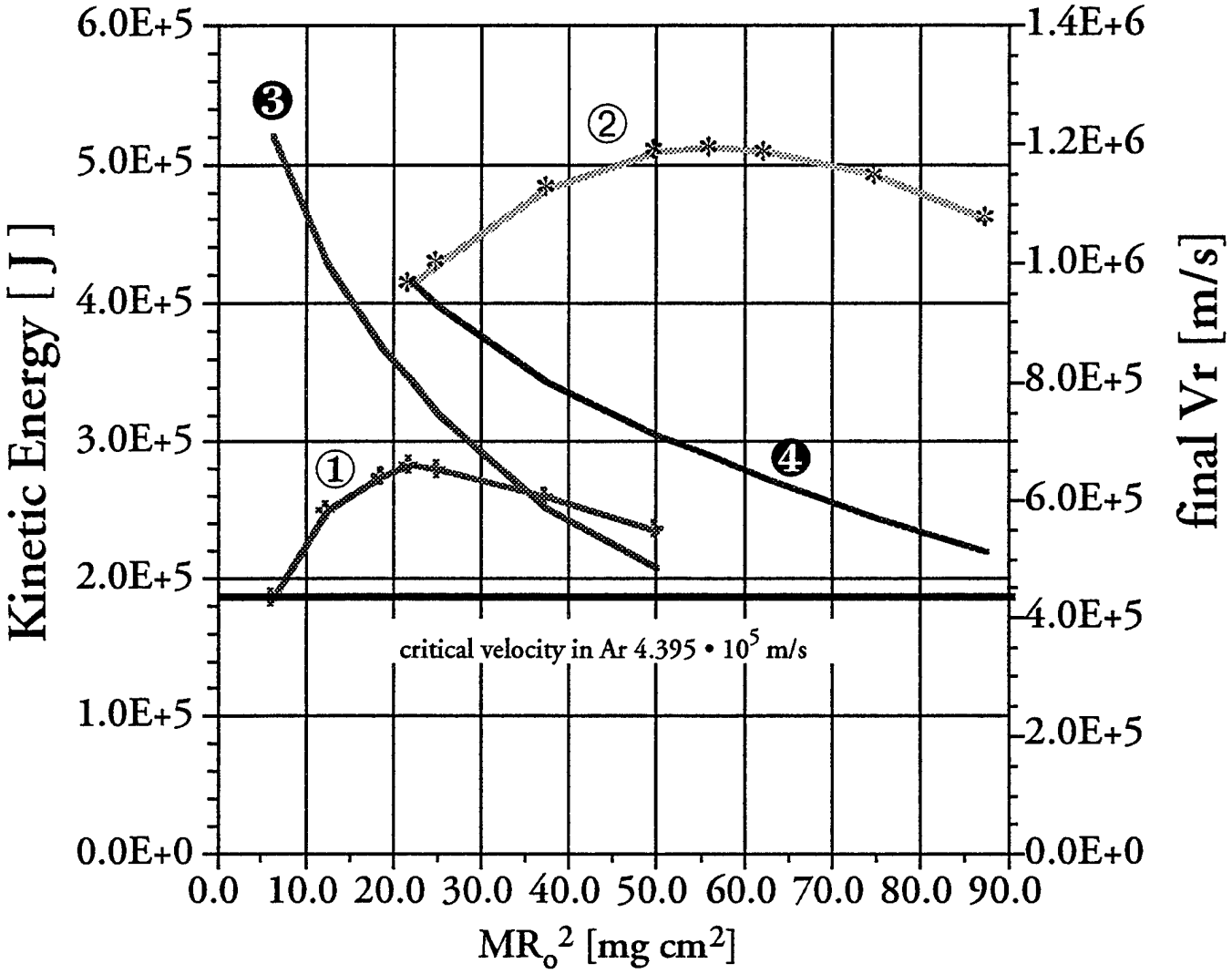

① KE prs Base	③ Vr prs Base
② KE prs Lo Z	④ Vr prs Lo Z

Fig. VI(C).3 Aggressive Decade Quad Design

— $M r_o^2$ case [21.875 mg cm^2 at 5.0 cm]—

KE variation with Z_{flo} at the post hole convolute

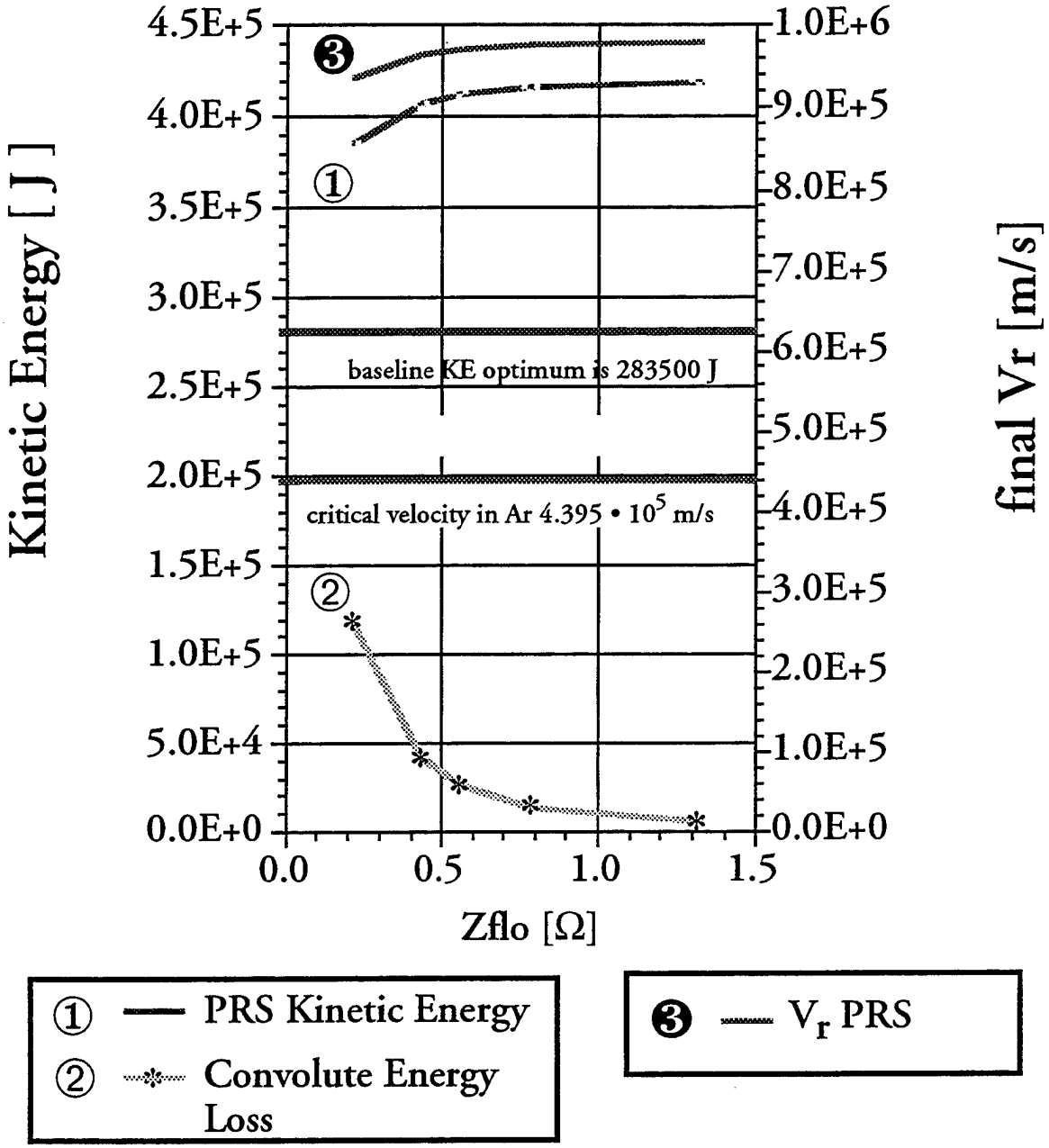

Fig. VI(C).4 Aggressive Decade Quad Design

— $M r_o^2$ case [50.0 mg cm^2 at 5.0 cm]—

KE variation with N_{cage}

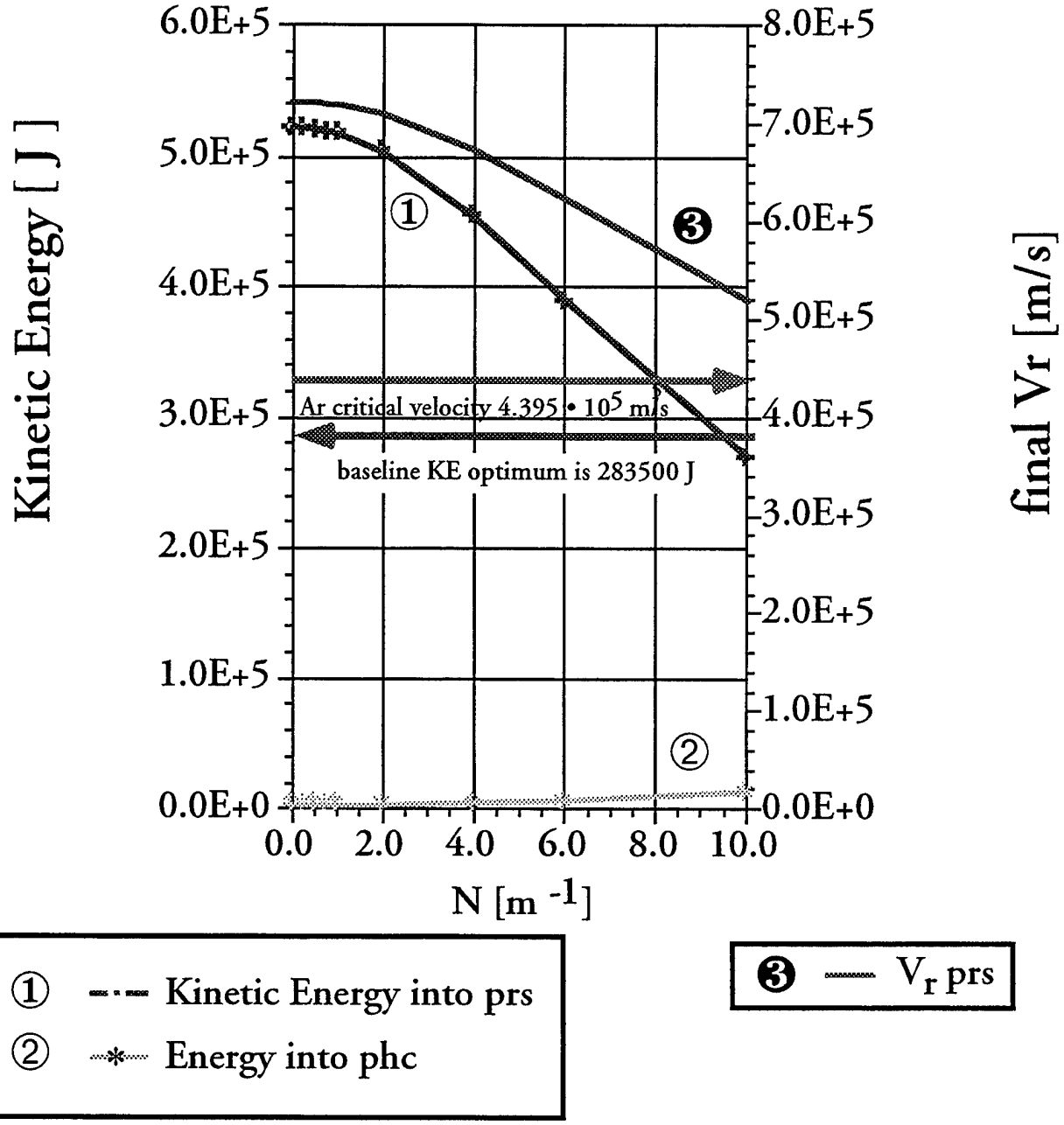

FIG. VI(C).5 ENERGY TRANSFER WITH PINCH LENGTH

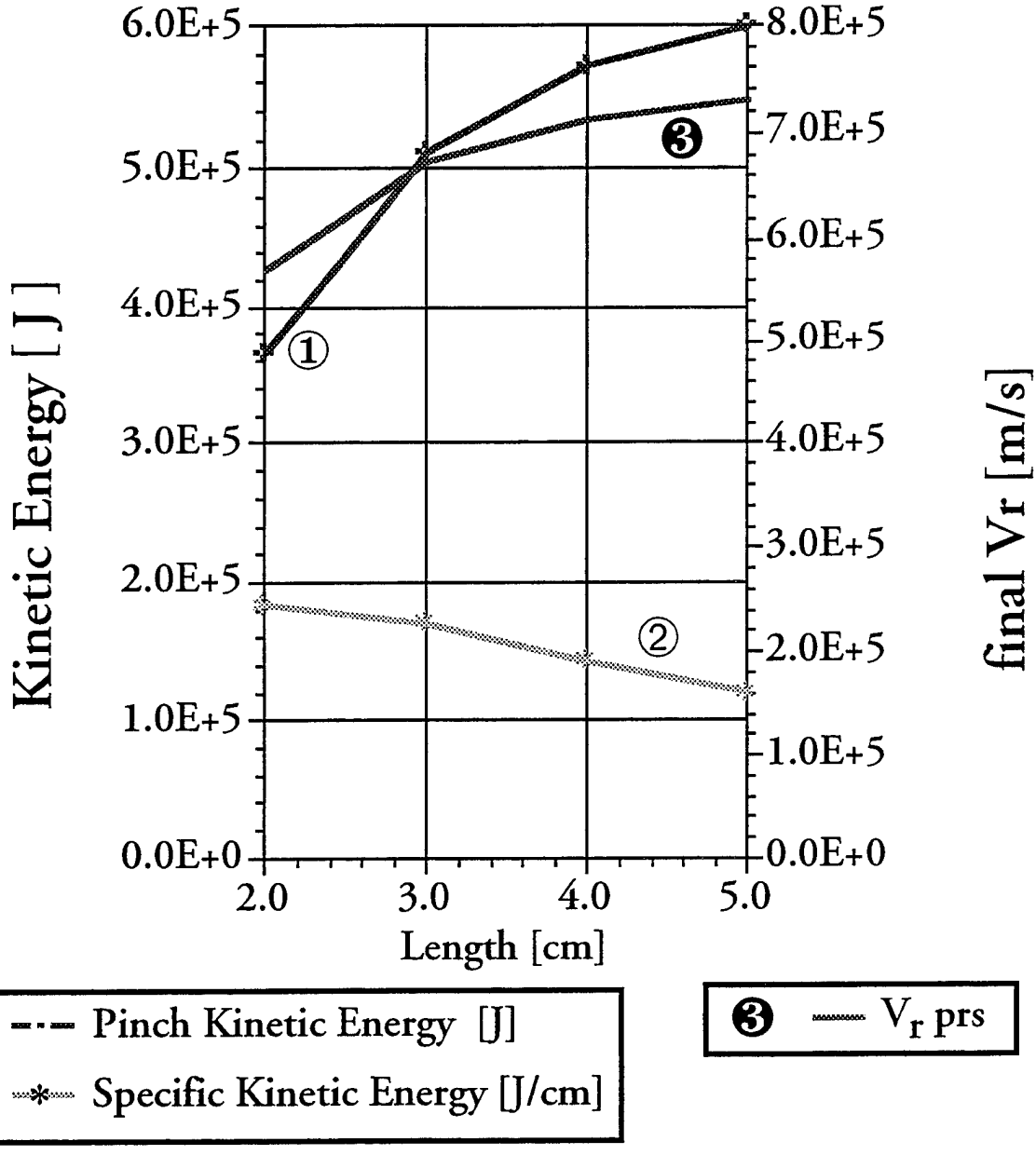

VII. D_2/Ar Uniform Fill Gas Puff Implosion: Line Converter Scheme

Introduction

The potential for producing intense sources of x-ray radiation in the megajoule regime employing pulsed power technology to drive Z-pinch plasma loads has been demonstrated with the successful operation of the "Z" Facility at Sandia National Laboratory. Recently, multiple wire array loads consisting of titanium wires or stainless steel wires (70 % Fe, 20 % Cr, 10 % Ni) produced Ti K-shell yields (> 4.5 keV) of about 150 kJ's and SS K-shell yield (> 6.5 keV) of about 65 kJ's in a pulse of about 9 ns duration. The total yield was about 1 MJ. These record yields further motivated improved load design culminating with the nested double wire array, pioneered by NRL (Davis, J. et. al., J. Appl. Phys. Lett. 70, 13 (1997)), that produced about 300 TW of radiated power. As the peak short circuit current into the load increases the simple scaling laws suggest that higher kinetic energy can be achieved generating larger η values producing a harder implosion and subsequently leading to the production of shorter wavelength x-rays with enhanced yields. However, as both the peak current and atomic number of the load increase so does the potential for deleteriously affecting the integrity of the implosion, particularly if the loads have to be mounted at larger diameter so as to implode at peak current. In addition to the enhanced possibility for generating plasma instabilities the K-shell yields may be limited because of the increase in the electron-ion equilibration times for higher atomic number loads. The slow transfer of energy from hot ions to cold electrons "freezes" the ionization states. This freezing of ionization states limits prospects of ionizing into the K-shell a substantial fraction of the plasma mass. In an effort to overcome this difficulty a number of scenarios are prudently being investigated. One such scheme has been proposed by Rudakov, et. al. And is referred to as a "Line Converter" scheme (Rudakov, L.I., et. al., Proceedings of the 4th International Conference on Z-Pinches, Vancouver (1997)).

The Line Converter scheme follows a two step process of energy conversion:

1. producing and heating the plasma with minimal radiation losses, and
2. fast "transfer" of the resulting high electron temperature to a converter.

The scheme relies on the separation of the implosion dynamics from the process of thermal conduction to the converter. However, the success of the concept depends on minimizing the radiation losses during the implosion and stagnation phases, i.e., keeping a substantial fraction of the plasma mass very hot so that it becomes fully ionized. Once fully ionized the radiative yield drops precipitously so that more of the energy, once available to be radiated away, will remain as thermal energy that can be transported effectively to the converter. However, we note for the record that there is a "slippery slope" here: if the K-shell is burned through quickly and the plasma becomes an inefficient Bremsstrahlung radiator, the plasma will sustain a very high temperature that oftentimes can lead to a softer implosion since it is harder to compress a hot plasma to compression ratios typically achieved with cooler plasmas. There is a fine line here dividing success from failure that depends on rendering Murphy's Law inoperative.

In this note we will explore only the radiative characteristics of a D_2/Ar uniform fill gas puff plasma, i.e., we will address item 1 above. The load is assumed driven first on the Sandia "Z" pulsed power accelerator. A second simulation will drive the load with a 20% increase in the peak current of "Z", i.e., 25 MA into the load. The simulations are carried out using a 1-D nonLTE Radiation Magneto-Hydrodynamics model referred to as DZAPP (Davis, J., et. al., Phys of Plasmas 2, 1766 (1995)) . The model includes an equivalent "Z" circuit selfconsistently coupled to the load. The ionization dynamic model used in these scoping simulations is more than a two level atom description but less than a full manifold of excited states. The model includes all the ground states and selected excited states in the K-shell and some structure in the Li-, Be-, and B-like states of argon. If anything, the reduced model will keep the plasma hotter than it actually would be if the full complement of excited states were used. Hence, the temperatures will be higher and the yields lower, i.e., these simulations represent a conservative estimate of conditions that might actually be achieved in the plasma. We also have a reasonable estimate of how loads with atomic numbers in the neighborhood of argon behave on "Z": Titanium wire arrays on "Z" produced about 150 kJ of K-shell and about 1 MJ total yield. A uniform fill consisting of D_2/Ar should produce similar K-shell results unless the plasma gets hot enough to be fully ionized!

Results

The initial conditions adopted are that of a uniform cylindrical fill puff gas mixture consisting of D_2 surrounding Ar. The initial radius of the load is 5 cm with a length of 2 cm. The total mass is 2400 μgm and is apportioned between the D_2 and Ar. A number of D_2:Ar mass ratios were studied, as indicated on Figure 6. For code validation purposes we performed a benchmark simulation to compare with the observed results obtained from Ti wires by imploding a shell load of pure argon from an initial radius of 2.7 cm and a length of 2 cm with a mass of 1200 μgm. The result is identified on Figure 6 and is commensurate with the Ti results in terms of K-shell yield. Although this result appears in close proximity to the 25 MA result it was actually simulated using "Z" as the driver, which coupled 18 MA into the argon shell load.

A brief history of selected hydrodynamic profiles as a function of radius (x) and time (μsec) are shown on Figure 1 for a 50/50 mixture by density of D_2/Ar gas puffs driven with a 20 MA peak short circuit current. The ion (I-Temp) and electron temperature (E-Temp) in eV, density (ρ) in gm/cm^3, and velocity ($V_>$) in cm/sec. Accompanying each plot is a "color" or "shade" scale representing a range of numerical values for each of the parameters. Note that the scale gradation is logarithmic for the ion and electron temperatures as well as the density. However, it is linear for the velocity. The plots start tracking the implosion at 200 ns and shows only the inner 2 cm of the pinch since, very little happens during the early run in phase. The temporal history continues through stagnation and peak compression and bounces out. The simulation is terminated when the plasma bounces out to a radius 2.5 times the minimum radius. The compression ratio at stagnation is about 10 to 1. This is easily seen in Figure 2 which shows a history of key pinch parameters. The peak electron temperature at peak compression is about 8 keV and the ion temperature is in excess of 100 keV. The electrons are not hot enough to fully strip all the argon. Also, as shown on Figure 1 not all the mass is heated to these peak temperatures. The spatially integrated energy history in ergs/cm is profiled on Figure 3 out to the same time, i.e., 0.2567 μsec. These include the ion thermal (Etha), electron thermal (Ethe), ionization (Eion), magnetic (Ebth), radiation (Erad), energies. The remaining energies on the Figure are self-explanatory. Although the plasma is a prolific radiator and radiated about 100 kJ's, the thermal and ion energies are almost an order of magnitude

larger. Much of this energy will be converted to kinetic energy and radiation as the plasma bounces out and cools by expansion and radiation.

The spatially and temporally integrated radiation spectrum is presented in Figure 4. The intensities for selected L- and K-shell lines are plotted as a function of photon energy from 10 eV to 10 keV. The ratio of the hydrogenlike to the heliumlike resonance line is greater than unity, and an indication that part of the plasma is hot enough to reach and sustain the hydrogenlike ionization stage. Figure 5 displays the emitted energy as a function of energy from 100 eV to 100 keV, i.e., this plot answers the question of how much thermal energy is emitted in selected energy bins for peak currents into the load by a "Z"like simulator. For the D_2/Ar load under consideration it is unlikely that 100 's of kJ's of energetic photons in excess of 3-4 keV can be generated from the thermalization process. However, the D_2/Ar load is not necessarily the optimum load if interest is in generating energetic photons in excess of 20 keV from the thermalization process on "Z"like simulators. Finally, Figure 6 presents results for "Z" for peak currents into the load of 18 and 25 MA as a function of density ratio of Ar to D_2. The total mass is 2400 μgm and the Ar/D_2 interface is fixed as indicated on the Figure. The total and K-shell energy radiated for the 25 MA machine is represented by the two upper curves while the two lower curves represent the 18 MA results. Also displayed on the Figure is the K-shell radiation from a 2.7 cm radius pure argon shell with a length of 2 cm and a mass of 1200 μgms. This result appears above the last value of the K-shell yield for the 25 MA simulation. This shell implosion is very much in line with the Ti wire array results obtained on "Z": for Ti the K-shell yield was about 150 kJ's and since Ar is of a lower atomic number one would expect an increase in the K-shell yield for Ar. Also, the K-shell scaling laws for the shell predict a result in excess of 200 kJ's in agreement with the more detailed calculations presented here.

The purpose of this exercise was to investigate the feasibility of generating energetic photons in excess of 20 keV employing a line converter scheme as proposed by Rudakov, et. al. As mentioned above, the constraints placed on the line converter scheme was: 1) to minimize the radiation and 2) fast "transfer" of the resulting high electron temperature to a converter. If the first part happens the second part is a simple heat conduction problem to a cold high-Z converter for which the physics is straightforward. However, even here

there are unanswered questions about energy conversion, blowoff plasma, radiation conversion efficiency, etc. However, phase 2 only happens if phase 1 occurs. For the loads and initial conditions investigated here the radiation was not minimized. In fact, the plasma behaved as most of the loads mounted on the "Z" facility – as prolific radiators! Because the plasma was a prolific radiator it was prevented from becoming hot enough to burn through the K-shell and become an inefficient bremsstrahlung radiator, which surely would have reduced the yield and kept the plasma hot. Also, if the yield was significantly reduced it may have become possible to uniformly heat more mass beyond the K-shell than was observed in the simulations. Based on the limited number of simulations investigated here we can only conclude that we were unable to minimize the radiation yields, impeding the prospects of uniformly heating a larger fraction of the plasma to significantly higher temperatures where all the argon would be fully stripped. In summary, the simulations presented here are not very encouraging but should not be misconstrued as very discouraging. We have only investigated a few simple loads on one real and one imaginary accelerator. There are a number of innovative loads that could be investigated on existing and proposed accelerators before making a final decision on the line converter scheme.

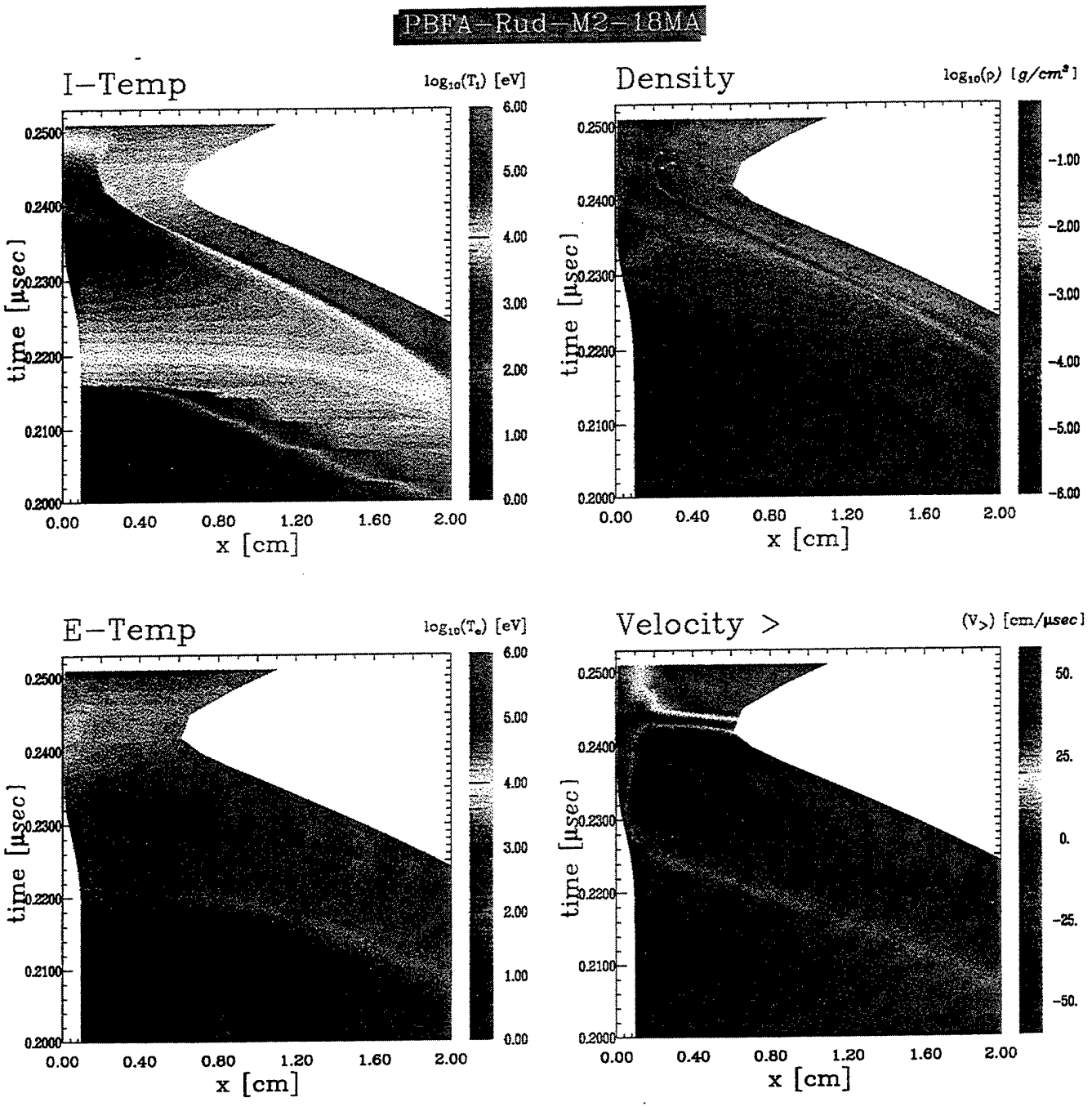
PBFA-Rud-M2-18MA
I-Temp
log10(Ti) [eV]
Density
log10(ρ) [g/cm3]
E-Temp
log10(Te) [eV]
Velocity >
(V>) [cm/μsec]
time [μsec]
x [cm]
0.2500
0.2400
0.2300
0.2200
0.2100
0.2000
0.00
0.40
0.80
1.20
1.60
2.00
6.00
5.00
4.00
3.00
2.00
1.00
0.00
-1.00
-2.00
-3.00
-4.00
-5.00
-6.00
50.
25.
0.
-25.
-50.

Fig. 1

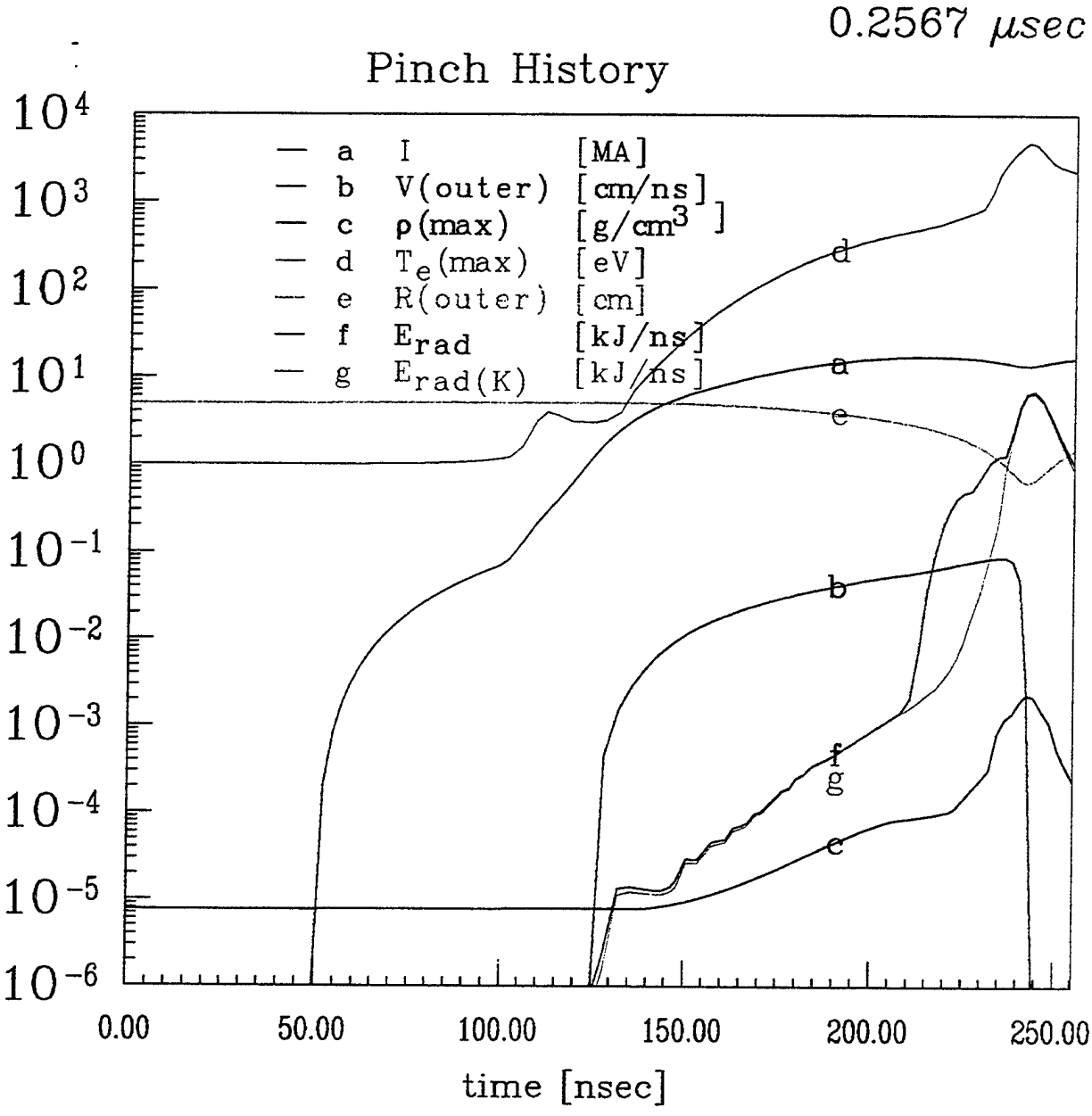

PBFA II-Z [D/Ar] Rudakov Qv= 5, Qh=1

Fig. 2

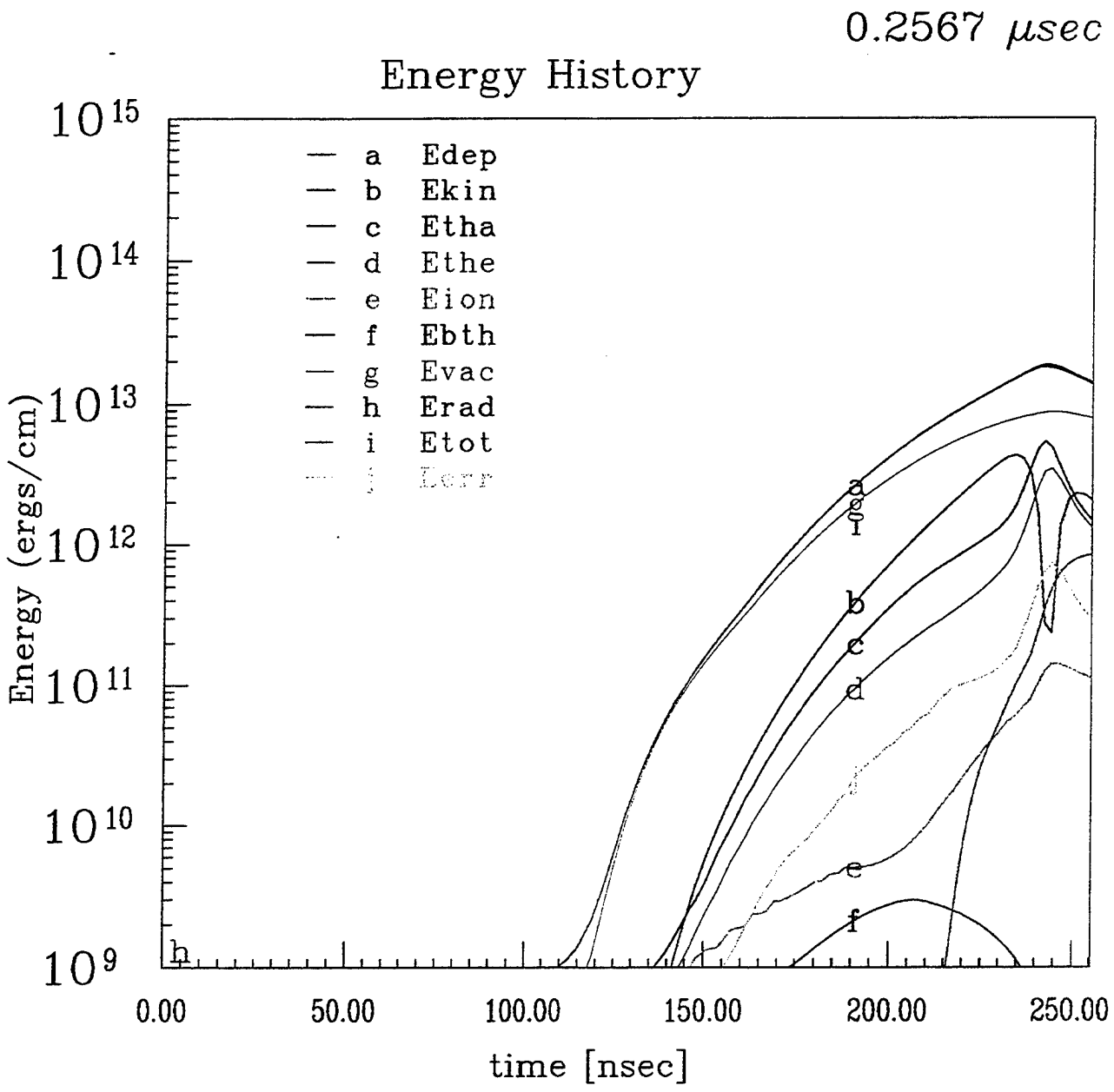

PBFA II-Z [D/Ar] Rudakov Qv= 5, Qh=1

Fig. 3

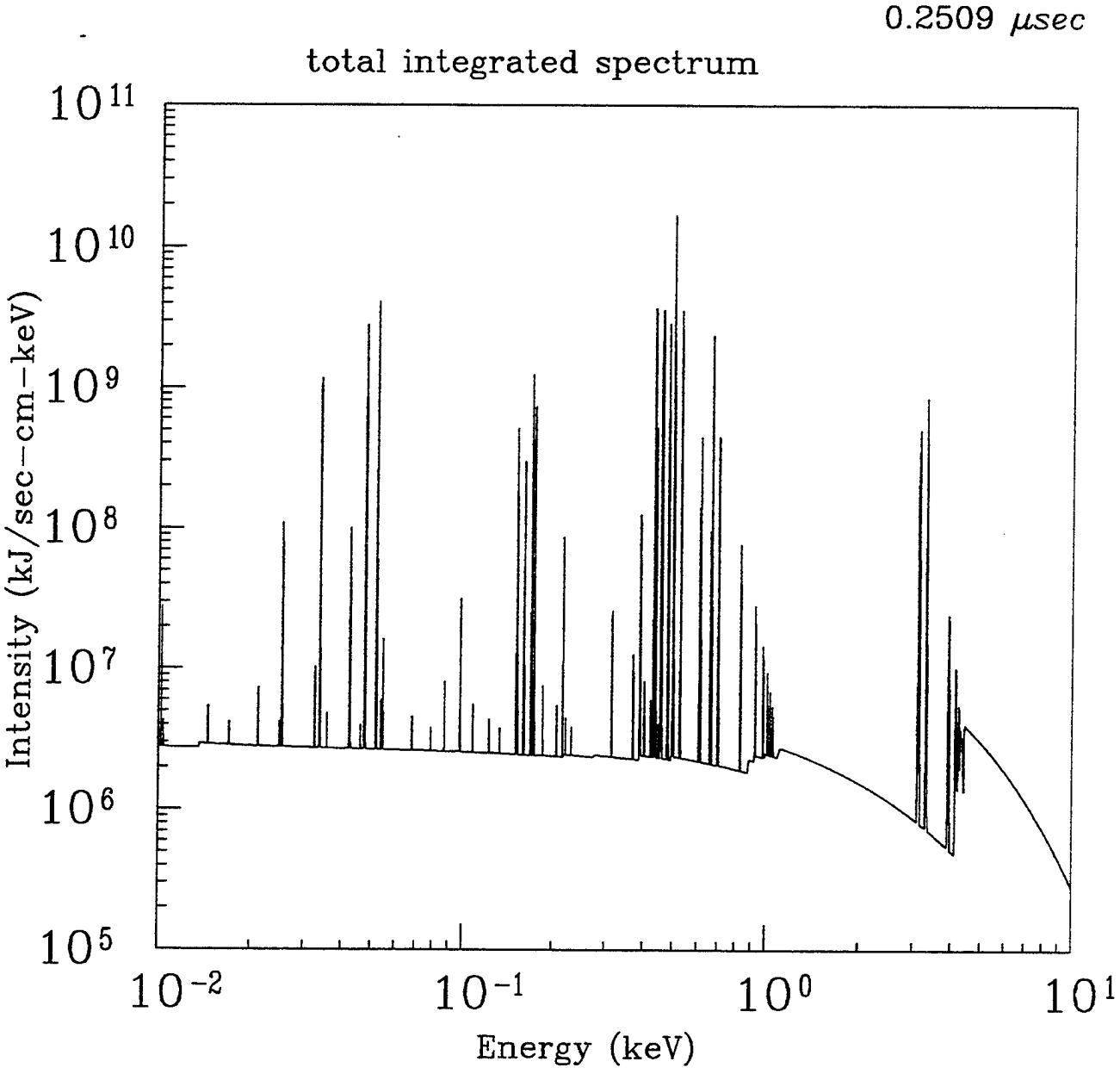

Page 1

PBFA II-Z [D/Ar] Rudakov Qv= 5, Qh=1

Fig. 4

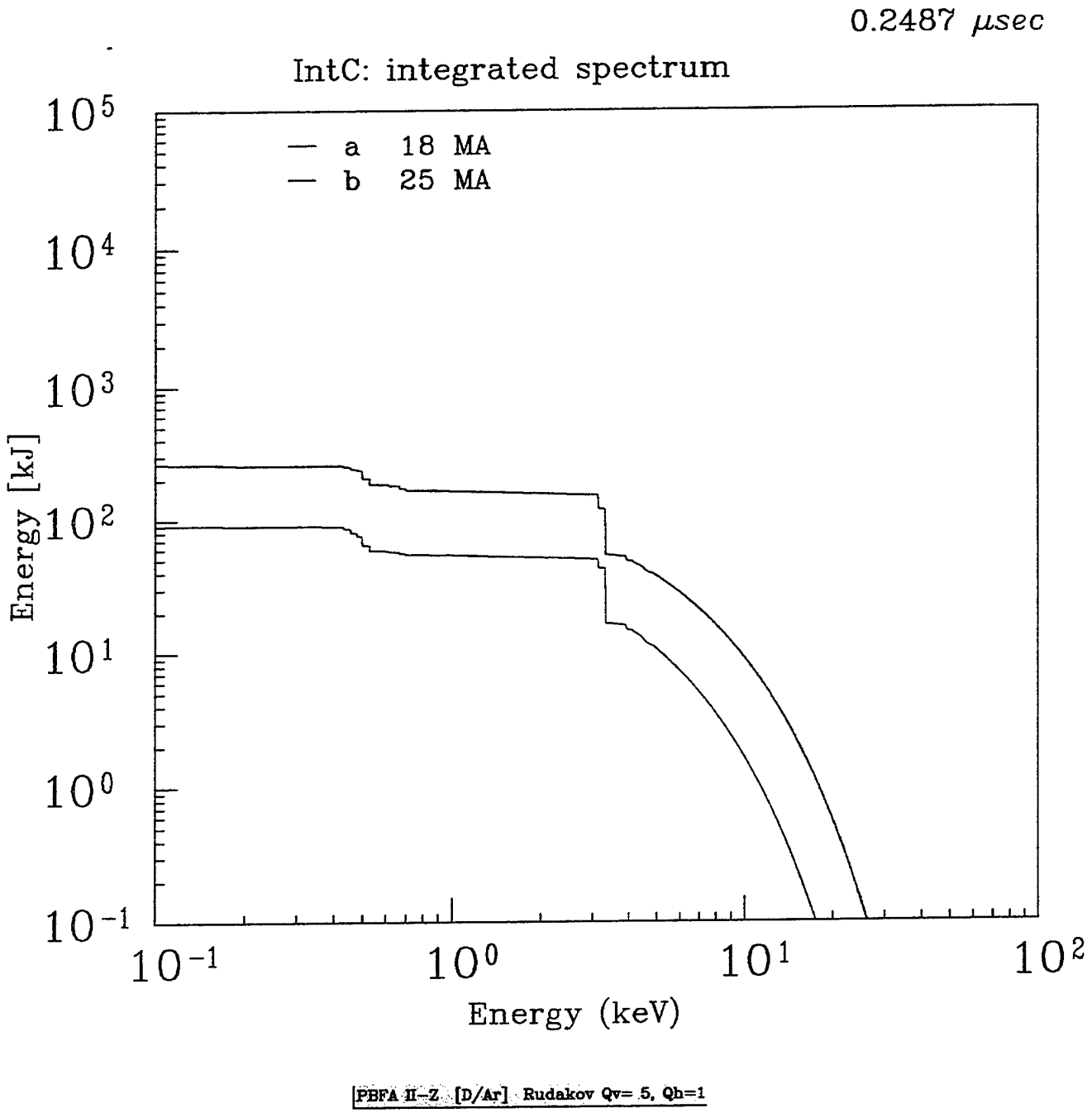
0.2487 μsec
IntC: integrated spectrum
— a 18 MA
— b 25 MA
Energy [kJ]
Energy (keV)
PBFA II-Z [D/Ar] Rudakov Qv= 5, Qh=1

Fig. 5

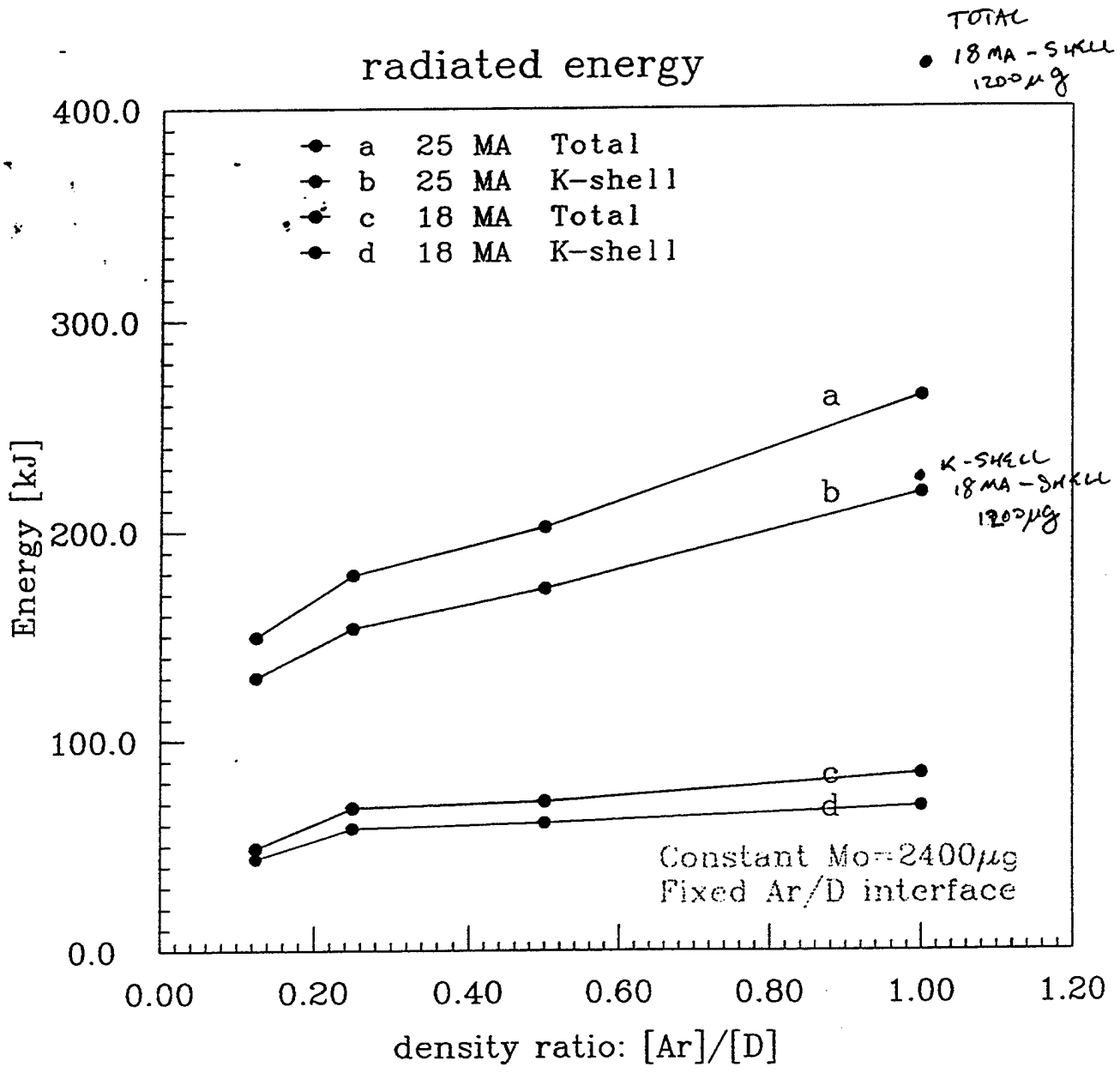

PBFA Z-25 Rudakov Qv= 5, Qh=1

Fig. 6

VIII. INFLUENCE OF IONIZATION DYNAMICS AND RADIATIVE TRANSPORT ON SPECTRA AND YIELD FROM MASSIVE ALUMINUM WIRE ARRAY IMPLOSIONS

Introduction

The modeling and numerical simulation of Z-pinch plasmas configured as multiple wire arrays, gas puffs, or various combinations of wires and puffs vary from simple slug models to complicated multidimensional scenarios. These models are then utilized to predict, postdict, and analyze the plasma as it evolves from the initial cold start phase to the final collapsed phase usually characterized by a burst of x-rays. The question always arises; how do the models describing the plasmas' ionization dynamic evolution compare with each other or predict the observations? In some instances simple slug models in conjunction with two level atom models have been employed to estimate the implosion time and the magnitude of the emitted K-shell x-ray pulse. At the other extreme there are 2- and 3-D RMHD (Radiation MagnetoHydroDynamic) scenarios that include a portfolio of subroutines on equation of state, ionization physics, transport properties, etc. These models attempt to treat the entire plasma morphology and address issues such as the onset and growth of plasma instabilities and how they affect the integrity of the implosion and the emitted x-ray pulse.

Model validation is usually done by comparing theoretically generated data with experimentally observed results for selected quantities that are considered characteristic of the implosion. These quantities often include the magnitude of the radiative yield, the x-ray pulse length and shape, x-ray pinhole photos of the assembling plasma at selected wavelengths, and emission spectra. It is well known that the emission spectrum as a function of space and time can provide a useful benchmark to validate the reliability of the simulation and help identify its strengths and weaknesses. In order to demonstrate the uniqueness and sensitivity of the emission spectrum to variations in the model we will perform a series of numerical simulations of an aluminum wire array driven by a circuit

similar to the Saturn accelerator. The simulations will be performed using a 1-D radiation MHD model to illustrate how the emission features and radiation signatures are influenced as the atomic and opacity models are modified. The use of a full 1-D model is sufficient to illustrate the sensitivity of the emission history to the choice of atomic and opacity model. For example, in the case of the multiple wire Al array loads (having 40 or more individual wires) investigated on the Saturn accelerator the implosion appeared to be less influenced by azimuthal asymmetries and, to first order, adequately represented by a 1-D implosion model at least as it approached the first bounce.[1] Also, comparing and contrasting the synthetically generated spectrum with the experimentally observed spectrum has the potential to identify any shortcomings the model possesses.

Model

The morphology of z-pinch plasmas generally exhibits three (and sometimes four) distinct and sometimes overlapping stages. The first stage is the initial heating and expansion phase. In the second stage the implosion is driven by the JxB force. The third stage is characterized by the plasma reassembling on axis converting kinetic energy of run-in to thermal energy. During this third stage the newly formed hot dense plasma emits an intense kilovolt x-ray pulse. On occasion, a final and fourth stage develops when the current is large enough to maintain plasma confinement, and additional heating and compression occurs accompanied by additional x-ray production.

The numerical simulations presented here to characterize the dynamics of a radially imploding Z-pinch plasma are based on a one-dimensional two temperature multi-zone non-LTE-radiation-magnetohydrodynamic model, DZAPP, with a transmission line circuit model representing the driving generator.[2] In a cylindrical coordinate system (r,z,t) the standard equations of continuity,

$$\frac{\partial \rho}{\partial t} + \frac{1}{r}\frac{\partial}{\partial r}(r\rho u) = 0, \tag{1}$$

total momentum,

$$\frac{\partial}{\partial t}(\rho u) + \frac{1}{r}\frac{\partial}{\partial r}(r\rho u^2) + \frac{\partial(p_i + p_e)}{\partial r} + \frac{1}{r}\frac{\partial}{\partial r}(rQ_{vis}) = -\frac{1}{c}J_z B_\phi, \qquad (2)$$

and ion internal energy,

$$\frac{\partial}{\partial t}(\rho\varepsilon_i) + \frac{1}{r}\frac{\partial}{\partial r}(r\rho\varepsilon_i u) + p_i\frac{1}{r}\frac{\partial}{\partial r}(ru) - \frac{1}{r}\frac{\partial}{\partial r}(r\kappa_i\frac{\partial T_i}{\partial r}) + Q_{vis}\frac{\partial u}{\partial r} = Q_{ie} \qquad (3a)$$

and electron internal energy,

$$\frac{\partial}{\partial t}(\rho\varepsilon_e) + \frac{1}{r}\frac{\partial}{\partial r}(r\rho\varepsilon_e u) + p_e\frac{1}{r}\frac{\partial}{\partial r}(ru) - \frac{1}{r}\frac{\partial}{\partial r}(r\kappa_e\frac{\partial T_e}{\partial r}) = -Q_{ie} + \eta J_z^2 - \Lambda \qquad (3b)$$

are integrated over each radial zone and then followed in a Lagrangian fashion. Here ρ is the mass density, u is the radial velocity, p_i the ion pressure, p_e the electron pressure, Q_{vis} the rr component of a tensor artificial viscosity for smoothing shocks, J_Z the axial current density in the pinch, B_ϕ the azimuthal magnetic field, $\varepsilon_{i(e)}$ the specific internal energy per unit mass of the ions(electrons), T_e the electron temperature, T_i the ion temperature, κ_e the electron thermal conductivity, κ_I the ion thermal conductivity, η the electrical resistivity, and Λ the radiation cooling (negative) or heating (positive) rate. The transport coefficients $\kappa_{i,e}$, η, and the ion-electron equilibration rate Q_{ie} are taken from Braginskii.[3] The numerical or artificial viscosity Q_{vis} for Lagrangian type codes is fully discussed by Schulz.[4] In the present paper we use $Q_{vis}=\beta\rho\Delta u C_S$, where Δu is the velocity difference across a zone and C_S is that zone's sound speed. Q_{vis} is zero if the zone is expanding. A value of 10 for the β parameter is used to soften the Z-pinch implosion and prevent radiative collapse.[5] Such a viscous enhancement is found to improve the agreement between experiment and simulation for the observed stagnation densities and radii.[6] Admittedly, the large viscous term is used to mimic the effect of presently unknown pinch physics leading to a softened implosion. The current density and magnetic field are related through Ampere's law

$$J_z = \frac{c}{4\pi}\frac{1}{r}\frac{\partial}{\partial r}(rB_\Phi). \qquad (4)$$

The magnetic field is determined by an induction equation by combining a generalized Ohm's law with Faraday's law:

$$\frac{\partial B_\phi}{\partial t} + \frac{\partial}{\partial r}(u B_\phi) = \frac{\partial}{\partial r}(c\,\eta J_z). \tag{5}$$

The ion internal energy includes the ion thermal energy as well as the atomic excitation + ionization specific energy (ε_x):

$$\varepsilon_i = \frac{3}{2}\frac{k_B T_i}{m_i} + \varepsilon_x \tag{6a}$$

The electron internal energy is represented by

$$\varepsilon_e = \frac{3}{2} < Z > \frac{k_B T_e}{m_i} \tag{6b}$$

where n_i is the ion number density, m_i is the ion mass, k_B is Boltzmann's constant and <Z> is the mean charge per ion.

The transmission line circuit model is similar to the BERTHA code of Hinshelwood.[7] The model follows the forward and backward propagating voltage waves assuming only transverse electromagnetic modes are present. Circuit elements have associated transit times Δt such that a line element of impedance Z has an resistance Z, an inductance $Z\Delta t$ or a capacitance $\Delta t/Z$. Wave propagation across junctions between line elements is solved through reflection and transmission coefficients derived from Kirchoff's laws. The junction at the dynamic load is treated implicitly to ensure strict conservation of electrical + plasma energy.

The ionization dynamics and radiation transport are time split from the magnetohydrodynamics, i.e., the ionization (and excitation) specific energy ε_x and charge state Z are held constant during a hydro timestep. As the excitation/ionization dynamics is updated within a zone, subject to the conservation of internal energy in that zone, the atomic level populations are determined by a set of rate equations

$$\frac{\partial f_{li}}{\partial t} = \sum_m (R_{mli}\, f_{mi} - R_{lmi}\, f_{li}), \tag{7}$$

where f_{li} is the fractional population of level l in the i^{th} ionic species, and R_{mli} is the net rate describing the transition in the i^{th} species from the initial level m to the final level l. The net rate includes collisional ionization, excitation, de-excitation, 3-body and radiative recombination, photo-ionization, radiation pumping and radiative decay. For the time dependent simulations the time derivative is maintained in eq. (7) and is neglected for equilibrium calculations. Details on the solution techniques and rate coefficients are summarized in Duston, et. al.[8]

The aluminum model contains all the ground states and an extensive manifold of excited states distributed throughout the various ionization stages. Only the strongest lines, i.e., lines with the largest oscillator strengths, were included in the simulation. Finally, except where noted, the majority of numerical simulations were carried out using an atomic model that contained a full K-shell excited state manifold with some 50 spectral lines while the L- and M-shells contained all ground states and an excited state manifold with about 150 selected spectral lines, respectively. This assumption represents a reasonable compromise between the atomic model and computational constraints, particularly when the medium is opaque.

Radiation emission, including opacity effects, from the plasma is dependent upon the local atomic-level populations, for not only are photons created by radiative recombination and decay, such photons also can lead to population redistribution. Thus the ionization dynamics and radiation transport are a strongly coupled interactive system and must be solved together as demonstrated in ref. 8. The radiation transport of the bound-bound and bound-free transitions is carried out using the probability of escape formalism described in Apruzese.[9] Multifrequency transport is performed for the free-free radiation. An additional benefit of performing detailed ionization modeling is the diagnostic capabilities that emerge directly from the calculation. Since spectral features are maintained throughout the calculation, they are easily reproduced in a form suitable for comparison with experimental data.

Results

The current profile that results from driving a Saturnlike generator circuit coupled to a changing load inductance is shown on Fig. 1. The short circuit peak current is about 10 mega-

amps. The load in this case is represented by ninety, 1.3 μm diameter aluminum wires with a total mass of 615 μgms. The initial array diameter is 1.72 cm and 2.0 cm long.

A snapshot view of the evolution of some of the hydrodynamic parameters from the DZAPP model is shown on Fig. 2 as a function of radius [(x) in cm and time in μsec] with a time dependent collisional-radiative ionization dynamic model (referred to as NEQ). The electron and ion temperatures are represented as E-Temp and I-Temp, respectively, and are measured in eV. The density is in gm/cm^3 and the velocity in cm/μsec. The plasma is expanding for positive values and is compressing for negative values of velocity, respectively. The "gray-scale" adjacent and to the right of each insert on the Figure quantifies the degree of shading. The "first" bounce occurs around 80 ns. The interpretation of the observations beyond the first bounce is clouded by the possibility that structure evolved and dominated the subsequent morphology vitiating the 1-D approach. Consequently, the structure may have significantly influenced the emission and x-ray pulse vitiating any meaningful comparison with the observational data. Therefore, we terminate the simulation after the plasma has expanded out to 2.5 times the minimum radius after the first bounce. At peak compression the ion temperature is about 160 keV and the electron temperature rises to about 15 keV in a highly localized region. The density at this time is about 0.51 gm/cm^3. Several other values are identified on each of the inserts for convenience.

To illustrate the consequences resulting from the application of various ionization dynamic models, we generate the emission spectra for some of the commonly used representations. The comparison of synthetic emission spectra with the observed spectra is often used as one of the benchmarks to assess the model and evaluate how well the numerical simulation described the implosion. In the past, analysis of a few selected spectral lines originating in the K-shell along with the continuum slope were unfolded to provide a measure of internal plasma conditions and evaluate the generators' energy-load coupling efficiency and the radiative performance. We are unaware of any attempts to create a temperature and density profile from the unfolded experimental data to re-run the models to generate a new synthetic spectra to compare with the original predictions and observations. All too often the observed spectra is not compared with the synthetic one because the radiation physics has been compromised to accommodate other aspects of the implosion modeling. It is all the more ironic

that our information and understanding of the implosion history comes from the monitored and observed "light", i.e., emitted radiation from the visible to the x-ray regime, but that the radiation modeling contained in many simulation models often remains crude and primitive and is treated in a superficial "window dressed" fashion .

The ionization dynamic models used here to quantify and construct an emission spectra are represented by NEQ, CRE (Collision Radiative Equilibrium), and LTE (Local Thermodynamic Equilibrium) for optically thick and thin simulations. All the simulations are self-contained in the sense that for each ionization model a full hydrodynamic simulation was performed rather than a post processing of a single hydrodynamic simulation. This caused some differences in the implosion times and differences in the minimum radius. All the simulations were integrated in time out to a final radius about 2.5 times the minimum implosion radius and include the first bounce and subsequent re-expansion out to the terminated radius. The total time integrated spectra produced from the NEQ model will serve as our benchmark simulation and is shown on Fig. 3. Some selected spectral lines are identified by upper and lower case letters along with the transition energy (keV), radiated power (MW/cm), and radiated energy (kJ). The helium- and hydrogen-like resonance lines account for about 50 % of the radiated K-shell energy. The calculated radiated energy emitted in the L- and K-shells is presented in Table 1.

RADIATIVE YIELDS

Ionization Model	Rad Transfer	Rad Yield (kJ) L-Shell	Rad Yield (kJ) K-Shell
NEQ	THICK	148.05	37.49
CRE	THICK	146.55	34.51
LTE	THICK	122.25	26.83
NEQ	THIN	112.80	35.54
CRE	THIN	126.30	44.16
LTE	THIN	138.00	39.10

TABLE 1

The THIN simulations are presented for completeness and because the optically thin approximation is often employed in many simulations to at least take some account of the radiative energetics and cooling of the plasma. A comparison of the magnitude of the L- and K-shell radiative yield shows that the simulations are in reasonably good agreement with each other and do not exhibit dramatically different results. The apparently good agreement of the yields for the thick and thin simulations is not purely fortuitous. The plasma is highly collisional and the bulk of the radiation originates in the L-shell, which, on the whole, is not far out of LTE for many of the lines. For the L-shell ionization dynamics both NEQ and CRE tend to LTE for many of the excited state populations. In addition, the dynamics of the implosion tends to equalize the total radiative yield. Strong radiative cooling reduces the electron temperature, which can limit the subsequent radiation. Therefore, for the overall radiative energetics the three ionization models do not differ enormously in magnitude from each other for the larger cooler plasma region. From an energetics point of view coupled with the data requirements and additional computational time involved it is easy to understand the tradeoff

in selecting the simplest model. However, only comparing the magnitude of the yields does not provide information about the energy distribution. That can only come from the emitted spectrum. Also, considering only yield ignores the fact that for the conditions generated during the implosion the plasma develops opacity in some regions of the plasma for which photopumping and radiation transport are essential. A closer scrutiny of the L-shell will reveal differences not only in the continuum but also in the peak intensity of individual lines. However slight these differences, it is more likely that the aluminum loads are well balanced for the generator and produced optimized yields minimizing the differences produced by the different models.

The experimental observations for several wire loads in this series of shots produced a total yield between 175 to 350 kJ and a K-shell yield between 35 and 51 kJ. As noted above direct comparison with the experimental observations is moot because of the uncertainty in structural integrity during the final stages of the implosion just prior to and immediately after stagnation. After the first bounce the plasma appeared unstable and showed signs of breaking up giving rise to bright spots of intensity superimposed on the bulk background plasma and may very well be the source of difference between the experimental and numerical values. However, the predictions shown in Table 1 are not totally inconsistent with the yield observations. The simulations predict a conversion of kinetic energy to total radiation of about 80% and to K-shell radiation of about 20% which is in agreement with earlier conversion efficiencies. Although the magnitude of the yield is close the distribution of radiated energy, particularly in the K-shell will be more revealing of any possible differences.

The total emission spectra are shown on Figs. 3-8 for the cases represented in Table 1. Fig. 3 represents the NEQ result and is considered our benchmark simulation. Figs. 4-8 reproduce the spectrum corresponding to the NEQ, CRE and LTE thick and thin models for comparison with Fig. 3. At first glance the NEQ, CRE, and LTE thick results look very much alike. However, the discerning eye will glimpse differences in specific lines and in the underlying continuum. The listing of transitions, radiated power and energy will help to identify individual differences. The underlying L-shell continuum is almost identical for the CRE and LTE full model results. The overall appearance as well as individual line features of the THIN simulations are remarkably similar to each other since the populations in the L-shell

are, for the most part, dominated by LTE populations. However, the THIN simulations exhibit a very different energy distribution from the THICK simulations.

This can be observed more clearly by focusing specifically on the K-shell energy distribution. Because the L-shell is so rich in line spectra it is difficult to determine from an integrated intensity distribution individual spectral differences when making the comparisons between simulations. However, the K-shell is not as densely populated and individual features can be isolated. These results are shown on Figures 9-14 for the various models. A comparison of the K-shell spectra shows quantitatively discernible differences between the simulations that can be useful in benchmarking numerical simulations and/or data bases. The distinct K-shell signature supports the premise that this methodology can be employed as a means of determining the accuracy of the simulation model as well as a tool for unfolding and analyzing conditions within the plasma as it evolves.

References

1. T. Sanford, G.O. Allshouse, et. al., Phys Rev Lett 77, 5063 (1996).
   K. Whitney, J. Thornhill, et. al., Phys Rev E 56, 1 (1997).
   T. Sanford, T. Nash, et. al., Rev Sci Instrum 68, 852 (1997).
2. J. Davis, J. Giuliani, Jr., M. Mulbrandon, Phys Plasmas 2, 1766 (1995).
3. S. Braginskii, *Review of Plasma Physics*, Ed. By M. A. Leontovich (Consultants Bureau, New York, 1, 205 (1965)).
4. W. Schultz, *Methods in Computational Physics*, Ed. By B. Alder, S. Fernbach, and M. Rotenberg (Academic Press 3, 1 (1964)).
5. J. Shearer, Phys Fluids 19, 1426 (1976).
6. J. Thornhill, K. Whitney, C. Deeney, P. Lapell, Phys Plasmas 1, 321 (1994).
7. D. Hinshelwood, Naval Research Lab Memo Rept No. 5185 (1983). Also, Technical Information Service Document No. 135024.
8. D. Duston, R. Clark, J. Davis, J. Apruzese, Phys Rev A27, 1441 (1983).
9. J. Apruzese, J Quant Spect & Rad Transfer, 25, 419 (1981).

Time (ns)	V(t) (MV)	I(t) (MA)
0.0	0.00	0.00
16.0	0.15	0.10
22.0	0.37	0.20
26.0	0.74	0.40
34.0	1.99	1.20
40.0	2.96	2.28
46.0	3.36	3.50
50.0	3.44	4.30
54.0	3.36	5.05
60.0	2.96	5.88
78.0	1.48	4.86
90.0	0.74	---
116.0	0.00	

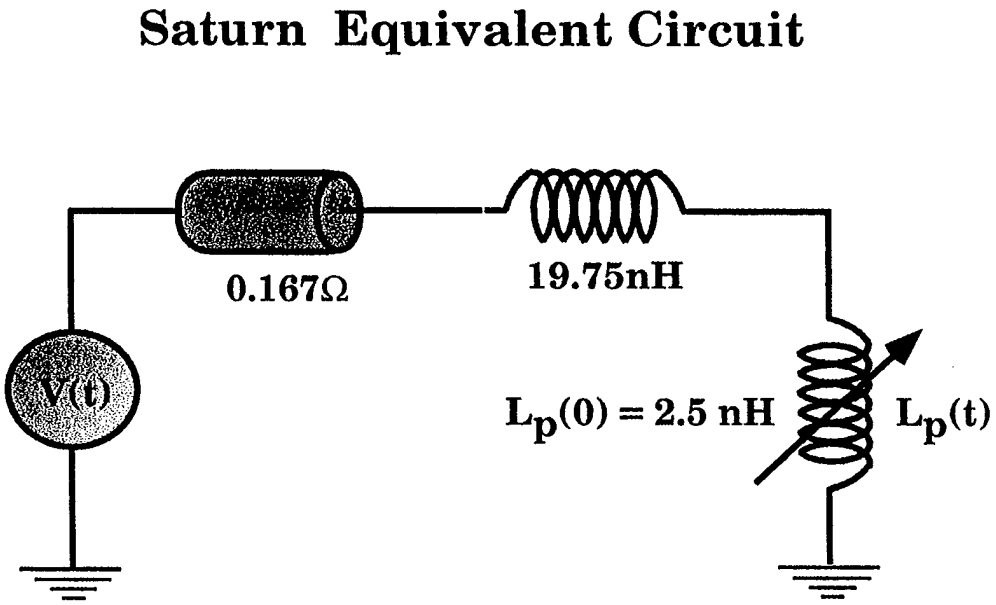

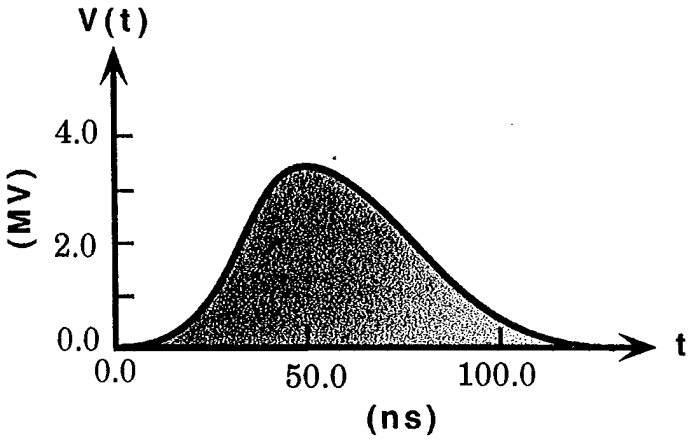

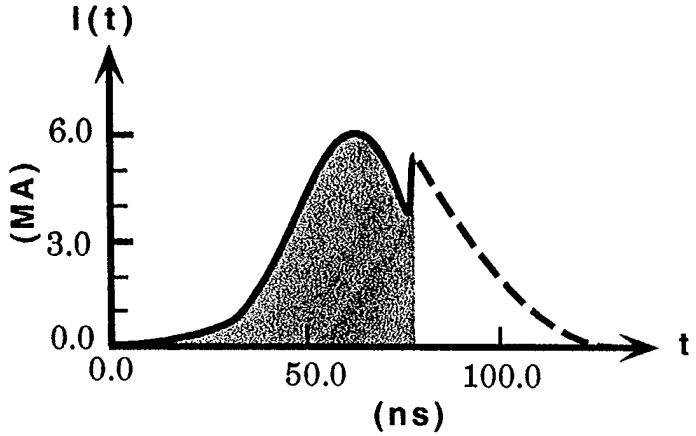

Fig. 1

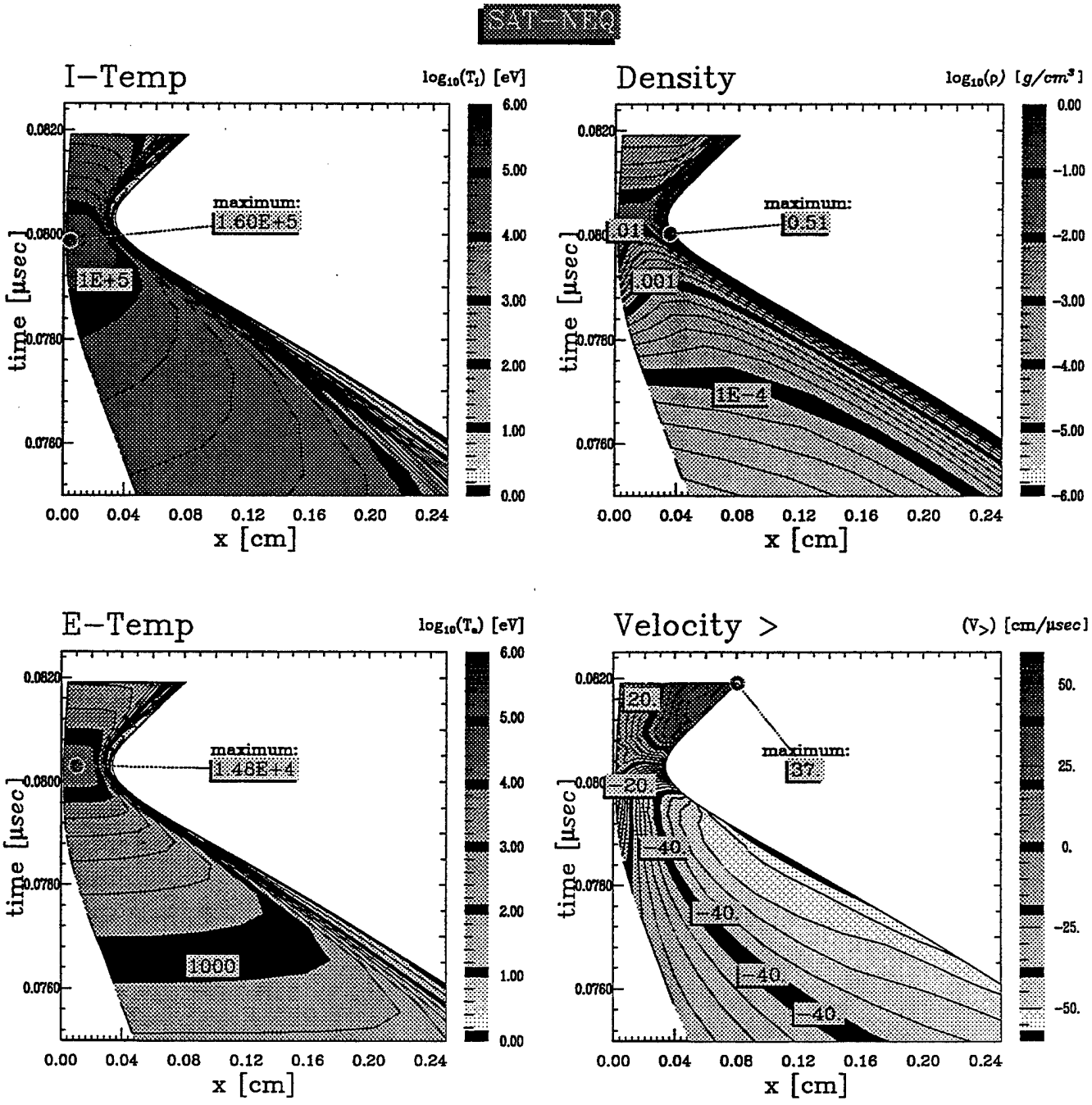
SAT-NEQ
I-Temp
log10(Ti) [eV]
maximum:
1.60E+5
1E+5
time [μsec]
x [cm]
Density
log10(ρ) [g/cm3]
maximum:
0.51
.01
.001
1E-4
E-Temp
log10(Te) [eV]
maximum:
1.46E+4
1000
Velocity >
(V>) [cm/μsec]
maximum:
37
20.
-20.
-40.

Fig. 2

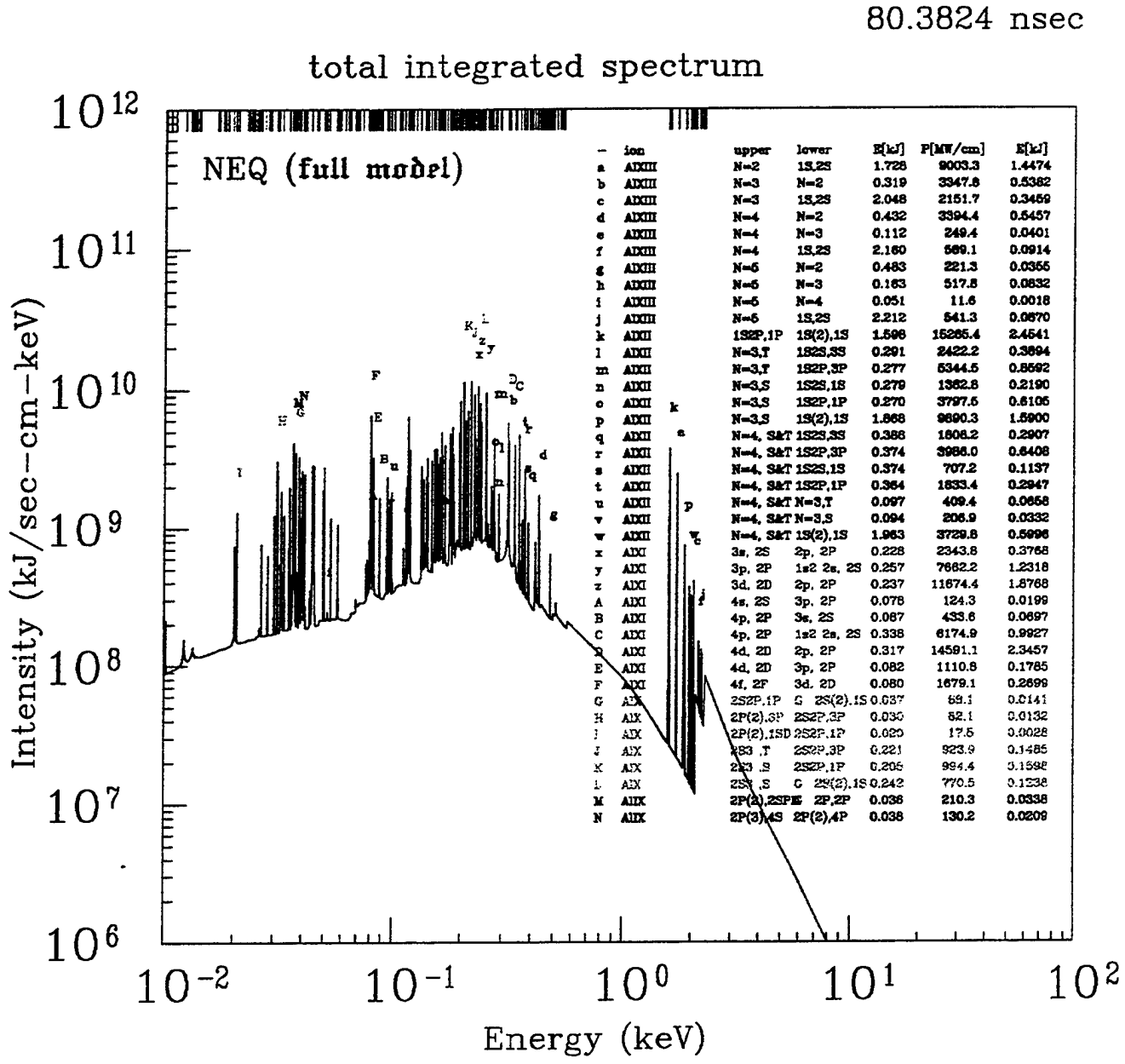
80.3824 nsec
total integrated spectrum
NEQ (full model)
Intensity (kJ/sec-cm-keV)
Energy (keV)
10^12
10^11
10^10
10^9
10^8
10^7
10^6
10^-2
10^-1
10^0
10^1
10^2
- ion upper lower E[kJ] P[MW/cm] E[kJ]
a AlXIII N=2 1S,2S 1.728 9003.3 1.4474
b AlXIII N=3 N=2 0.319 3347.8 0.5382
c AlXIII N=3 1S,2S 2.048 2151.7 0.3459
d AlXIII N=4 N=2 0.432 3394.4 0.5457
e AlXIII N=4 N=3 0.112 249.4 0.0401
f AlXIII N=4 1S,2S 2.160 569.1 0.0914
g AlXIII N=5 N=2 0.483 221.3 0.0355
h AlXIII N=5 N=3 0.163 517.8 0.0832
i AlXIII N=5 N=4 0.051 11.6 0.0018
j AlXIII N=5 1S,2S 2.212 541.3 0.0870
k AlXII 1S2P,1P 1S(2),1S 1.596 15265.4 2.4541
l AlXII N=3,T 1S2S,3S 0.291 2422.2 0.3894
m AlXII N=3,T 1S2P,3P 0.277 5344.5 0.8592
n AlXII N=3,S 1S2S,1S 0.279 1362.8 0.2190
o AlXII N=3,S 1S2P,1P 0.270 3797.5 0.6105
p AlXII N=3,S 1S(2),1S 1.868 9690.3 1.5900
q AlXII N=4, S&T 1S2S,3S 0.386 1806.2 0.2907
r AlXII N=4, S&T 1S2P,3P 0.374 3986.0 0.6408
s AlXII N=4, S&T 1S2S,1S 0.374 707.2 0.1137
t AlXII N=4, S&T 1S2P,1P 0.364 1833.4 0.2947
u AlXII N=4, S&T N=3,T 0.097 409.4 0.0658
v AlXII N=4, S&T N=3,S 0.094 206.9 0.0332
w AlXII N=4, S&T 1S(2),1S 1.963 3729.8 0.5996
x AlXI 3s, 2S 2p, 2P 0.228 2343.8 0.3768
y AlXI 3p, 2P 1s2 2s, 2S 0.257 7662.2 1.2318
z AlXI 3d, 2D 2p, 2P 0.237 11674.4 1.8768
A AlXI 4s, 2S 3p, 2P 0.078 124.3 0.0199
B AlXI 4p, 2P 3s, 2S 0.087 433.6 0.0697
C AlXI 4p, 2P 1s2 2s, 2S 0.338 6174.9 0.9927
D AlXI 4d, 2D 2p, 2P 0.317 14591.1 2.3457
E AlXI 4d, 2D 3p, 2P 0.082 1110.8 0.1785
F AlXI 4f, 2F 3d, 2D 0.080 1679.1 0.2699
G AlX 2S2P,1P 1S 2S(2),1S 0.037 88.1 0.0141
H AlX 2P(2),3P 2S2P,3P 0.030 82.1 0.0132
I AlX 2P(2),1SD 2S2P,1P 0.020 17.5 0.0028
J AlX 2S3 ,T 2S2P,3P 0.221 923.9 0.1485
K AlX 2S3 ,S 2S2P,1P 0.205 994.4 0.1598
L AlX 2S3 ,S 1S 2S(2),1S 0.242 770.5 0.1238
M AlIX 2P(2),2SP3 2P,2P 0.036 210.3 0.0338
N AlIX 2P(3),4S 2P(2),4P 0.038 130.2 0.0209

Fig. 3

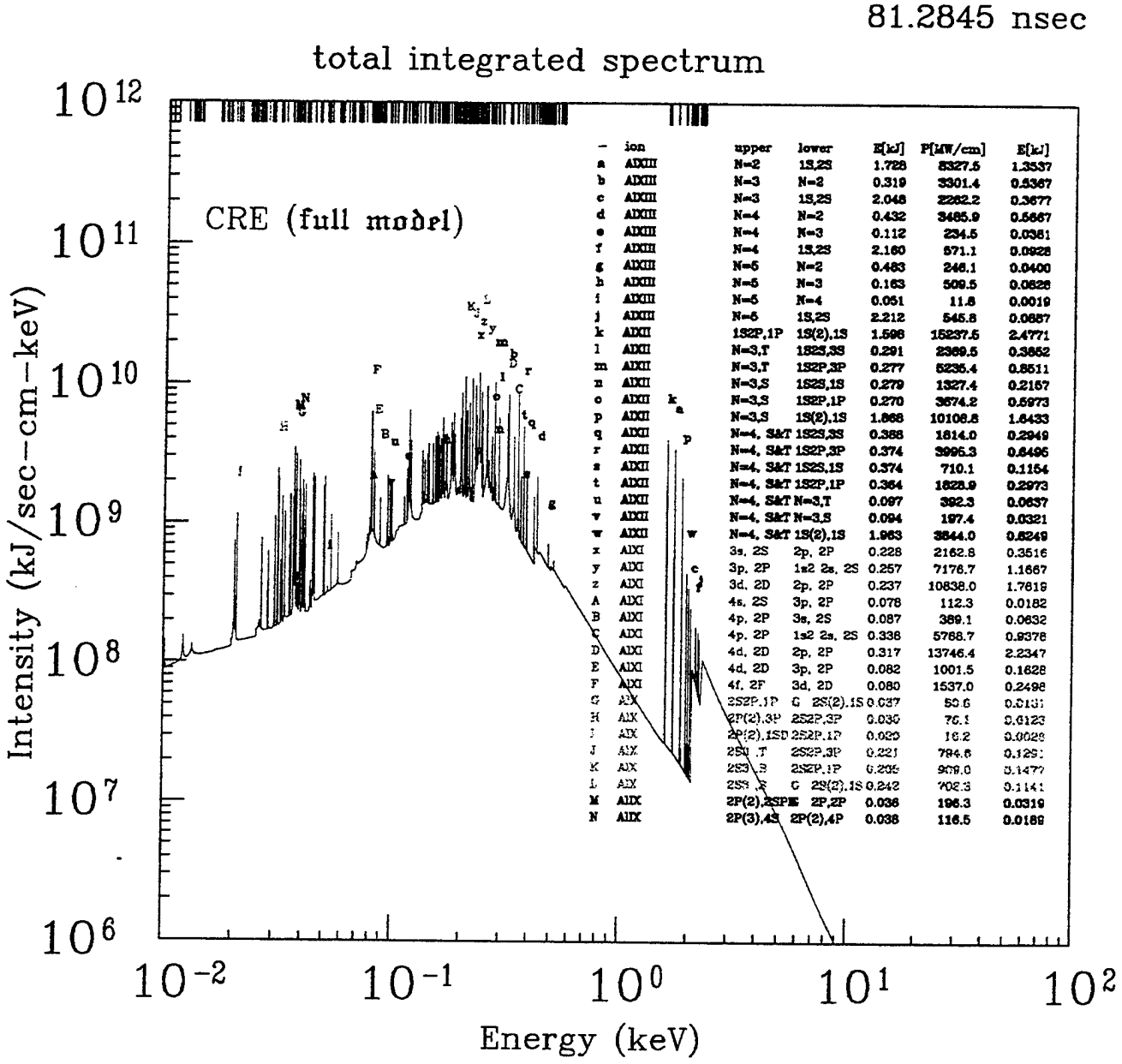
81.2845 nsec
total integrated spectrum
CRE (full model)
Intensity (kJ/sec-cm-keV)
Energy (keV)
10^{12}
10^{11}
10^{10}
10^{9}
10^{8}
10^{7}
10^{6}
10^{-2}
10^{-1}
10^{0}
10^{1}
10^{2}
- ion upper lower E[kJ] P[MW/cm] E[kJ]
a AlXIII N=2 1S,2S 1.728 8327.5 1.3537
b AlXIII N=3 N=2 0.319 3301.4 0.5367
c AlXIII N=3 1S,2S 2.048 2282.2 0.3677
d AlXIII N=4 N=2 0.432 3465.9 0.5667
e AlXIII N=4 N=3 0.112 234.5 0.0361
f AlXIII N=4 1S,2S 2.160 571.1 0.0928
g AlXIII N=5 N=2 0.483 246.1 0.0400
h AlXIII N=5 N=3 0.163 509.5 0.0828
i AlXIII N=5 N=4 0.051 11.8 0.0019
j AlXIII N=5 1S,2S 2.212 545.8 0.0887
k AlXII 1S2P,1P 1S(2),1S 1.596 15237.5 2.4771
l AlXII N=3,T 1S2S,3S 0.291 2369.5 0.3852
m AlXII N=3,T 1S2P,3P 0.277 5235.4 0.8511
n AlXII N=3,S 1S2S,1S 0.279 1327.4 0.2157
o AlXII N=3,S 1S2P,1P 0.270 3674.2 0.5973
p AlXII N=3,S 1S(2),1S 1.868 10108.8 1.6433
q AlXII N=4, S&T 1S2S,3S 0.368 1814.0 0.2949
r AlXII N=4, S&T 1S2P,3P 0.374 3995.3 0.6496
s AlXII N=4, S&T 1S2S,1S 0.374 710.1 0.1154
t AlXII N=4, S&T 1S2P,1P 0.364 1828.9 0.2973
u AlXII N=4, S&T N=3,T 0.097 392.3 0.0637
v AlXII N=4, S&T N=3,S 0.094 197.4 0.0321
w AlXII N=4, S&T 1S(2),1S 1.963 3844.0 0.6249
x AlXI 3s, 2S 2p, 2P 0.228 2162.8 0.3516
y AlXI 3p, 2P 1s2 2s, 2S 0.257 7176.7 1.1667
z AlXI 3d, 2D 2p, 2P 0.237 10838.0 1.7619
A AlXI 4s, 2S 3p, 2P 0.078 112.3 0.0182
B AlXI 4p, 2P 3s, 2S 0.087 389.1 0.0632
C AlXI 4p, 2P 1s2 2s, 2S 0.338 5768.7 0.9378
D AlXI 4d, 2D 2p, 2P 0.317 13746.4 2.2347
E AlXI 4d, 2D 3p, 2P 0.082 1001.5 0.1628
F AlXI 4f, 2F 3d, 2D 0.080 1537.0 0.2498
G AlX 2S2P,1P G 2S(2),1S 0.037 50.6 0.0131
H AlX 2P(2),3P 2S2P,3P 0.030 76.1 0.0123
I AlX 2P(2),1SD 2S2P,1P 0.020 16.2 0.0026
J AlX 2S0 ,T 2S2P,3P 0.221 784.6 0.1291
K AlX 2S3 ,S 2S2P,1P 0.205 909.0 0.1477
L AlX 2S9 ,S G 2S(2),1S 0.242 702.3 0.1141
M AlIX 2P(2),2SPE 2P,2P 0.036 196.3 0.0319
N AlIX 2P(3),4S 2P(2),4P 0.038 116.5 0.0189

Fig. 4

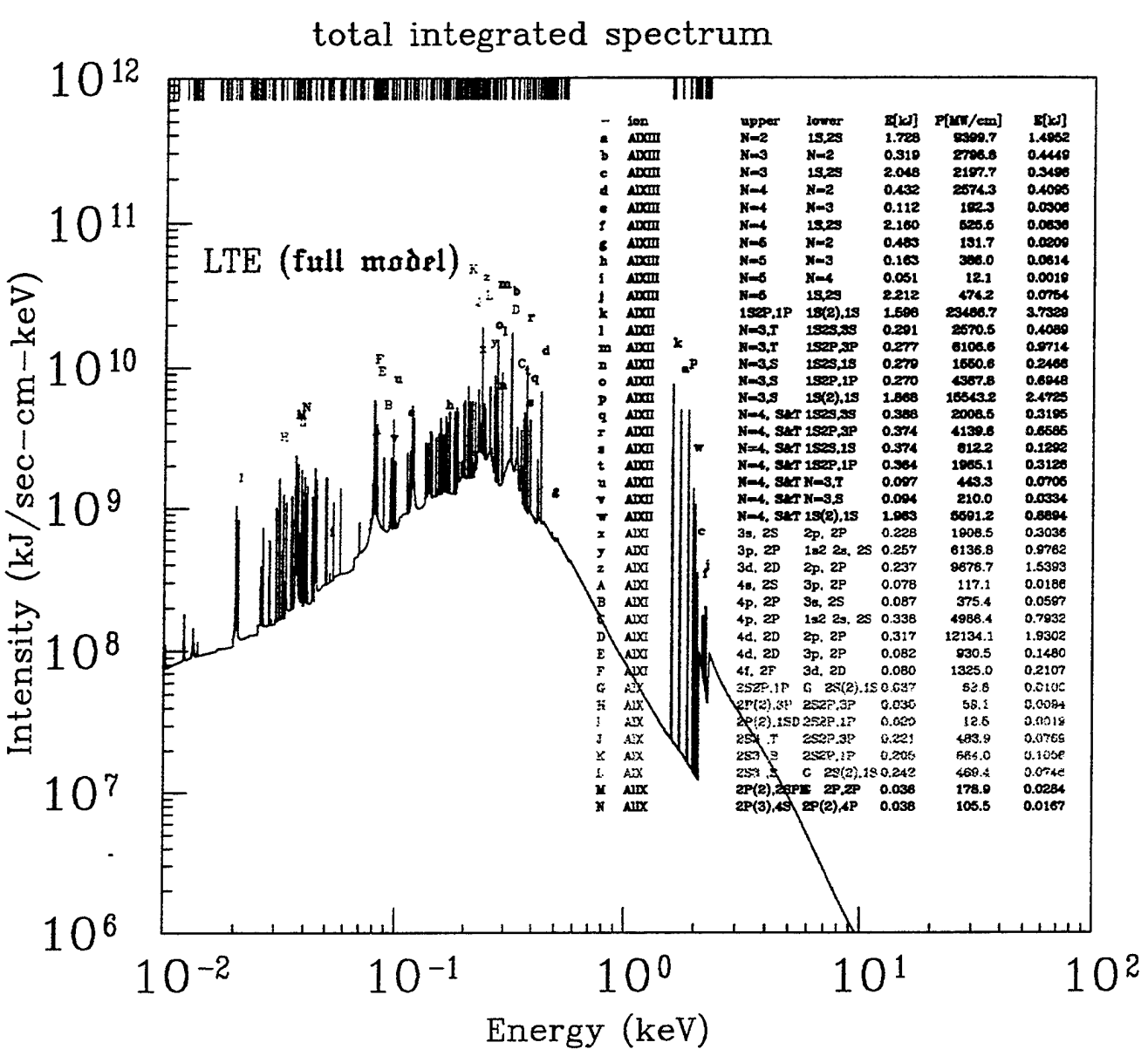

–	ion	upper	lower	E[kJ]	P[MW/cm]	E[kJ]
a	AlXIII	N=2	1S,2S	1.728	9399.7	1.4952
b	AlXIII	N=3	N=2	0.319	2796.8	0.4449
c	AlXIII	N=3	1S,2S	2.048	2197.7	0.3496
d	AlXIII	N=4	N=2	0.432	2574.3	0.4095
e	AlXIII	N=4	N=3	0.112	192.3	0.0306
f	AlXIII	N=4	1S,2S	2.160	525.5	0.0836
g	AlXIII	N=5	N=2	0.483	131.7	0.0209
h	AlXIII	N=5	N=3	0.163	386.0	0.0614
i	AlXIII	N=5	N=4	0.051	12.1	0.0019
j	AlXIII	N=6	1S,2S	2.212	474.2	0.0754
k	AlXII	1S2P,1P	1S(2),1S	1.596	23466.7	3.7329
l	AlXII	N=3,T	1S2S,3S	0.291	2570.5	0.4089
m	AlXII	N=3,T	1S2P,3P	0.277	6106.6	0.9714
n	AlXII	N=3,S	1S2S,1S	0.279	1550.6	0.2466
o	AlXII	N=3,S	1S2P,1P	0.270	4367.8	0.6948
p	AlXII	N=3,S	1S(2),1S	1.868	15543.2	2.4725
q	AlXII	N=4, S&T	1S2S,3S	0.388	2008.5	0.3195
r	AlXII	N=4, S&T	1S2P,3P	0.374	4139.8	0.6585
s	AlXII	N=4, S&T	1S2S,1S	0.374	812.2	0.1292
t	AlXII	N=4, S&T	1S2P,1P	0.364	1965.1	0.3126
u	AlXII	N=4, S&T	N=3,T	0.097	443.3	0.0705
v	AlXII	N=4, S&T	N=3,S	0.094	210.0	0.0334
w	AlXII	N=4, S&T	1S(2),1S	1.963	5591.2	0.8894
x	AlXI	3s, 2S	2p, 2P	0.228	1908.5	0.3036
y	AlXI	3p, 2P	1s2 2s, 2S	0.257	6136.8	0.9762
z	AlXI	3d, 2D	2p, 2P	0.237	9676.7	1.5393
A	AlXI	4s, 2S	3p, 2P	0.078	117.1	0.0186
B	AlXI	4p, 2P	3s, 2S	0.087	375.4	0.0597
C	AlXI	4p, 2P	1s2 2s, 2S	0.338	4986.4	0.7932
D	AlXI	4d, 2D	2p, 2P	0.317	12134.1	1.9302
E	AlXI	4d, 2D	3p, 2P	0.082	930.5	0.1480
F	AlXI	4f, 2F	3d, 2D	0.080	1325.0	0.2107
G	AlX	2S2P,1P	G 2S(2),1S	0.037	52.8	0.0100
H	AlX	2P(2),3P	2S2P,3P	0.030	58.1	0.0094
I	AlX	2P(2),1SD	2S2P,1P	0.020	12.5	0.0019
J	AlX	2S3 ,T	2S2P,3P	0.221	483.9	0.0769
K	AlX	2S3 ,S	2S2P,1P	0.205	664.0	0.1056
L	AlX	2S3 ,S	G 2S(2),1S	0.242	469.4	0.0746
M	AlIX	2P(2),2SPE	2P,2P	0.036	178.9	0.0284
N	AlIX	2P(3),4S	2P(2),4P	0.038	105.5	0.0167

Fig. 5

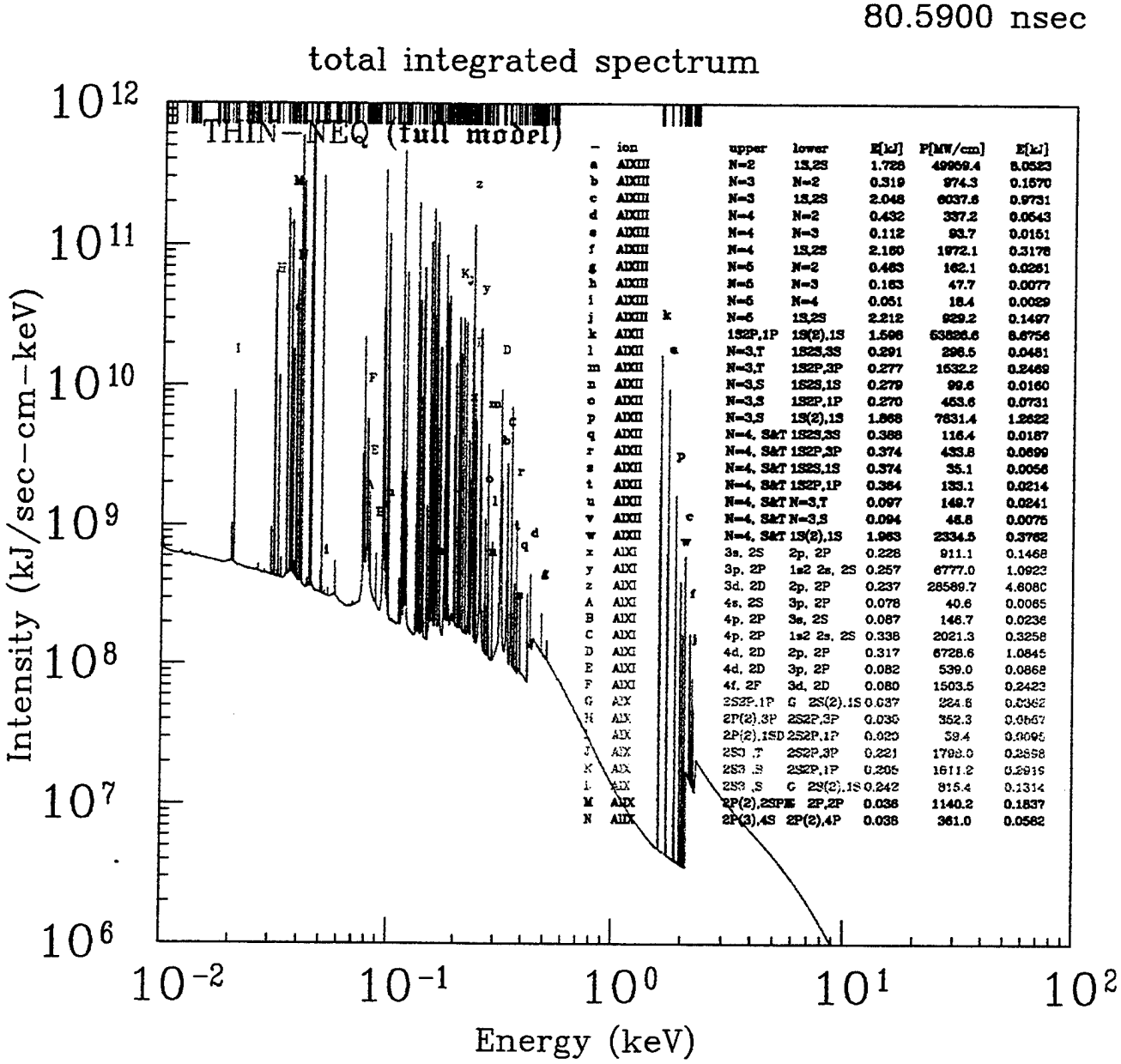

–	ion	upper	lower	E[kJ]	P[MW/cm]	E[kJ]
a	AlXIII	N=2	1S,2S	1.728	49959.4	8.0523
b	AlXIII	N=3	N=2	0.319	974.3	0.1570
c	AlXIII	N=3	1S,2S	2.048	6037.6	0.9731
d	AlXIII	N=4	N=2	0.432	337.2	0.0543
e	AlXIII	N=4	N=3	0.112	93.7	0.0151
f	AlXIII	N=4	1S,2S	2.160	1972.1	0.3178
g	AlXIII	N=5	N=2	0.463	162.1	0.0261
h	AlXIII	N=5	N=3	0.163	47.7	0.0077
i	AlXIII	N=5	N=4	0.051	18.4	0.0029
j	AlXIII	N=6	1S,2S	2.212	929.2	0.1497
k	AlXII	1S2P,1P	1S(2),1S	1.596	53826.6	8.6756
l	AlXII	N=3,T	1S2S,3S	0.291	296.5	0.0481
m	AlXII	N=3,T	1S2P,3P	0.277	1632.2	0.2469
n	AlXII	N=3,S	1S2S,1S	0.279	99.6	0.0160
o	AlXII	N=3,S	1S2P,1P	0.270	453.6	0.0731
p	AlXII	N=3,S	1S(2),1S	1.868	7831.4	1.2622
q	AlXII	N=4, S&T	1S2S,3S	0.388	116.4	0.0187
r	AlXII	N=4, S&T	1S2P,3P	0.374	433.8	0.0699
s	AlXII	N=4, S&T	1S2S,1S	0.374	35.1	0.0056
t	AlXII	N=4, S&T	1S2P,1P	0.364	133.1	0.0214
u	AlXII	N=4, S&T	N=3,T	0.097	149.7	0.0241
v	AlXII	N=4, S&T	N=3,S	0.094	46.6	0.0075
w	AlXII	N=4, S&T	1S(2),1S	1.963	2334.5	0.3762
x	AlXI	3s, 2S	2p, 2P	0.228	911.1	0.1468
y	AlXI	3p, 2P	1s2 2s, 2S	0.257	6777.0	1.0923
z	AlXI	3d, 2D	2p, 2P	0.237	28589.7	4.6080
A	AlXI	4s, 2S	3p, 2P	0.078	40.6	0.0065
B	AlXI	4p, 2P	3s, 2S	0.087	146.7	0.0236
C	AlXI	4p, 2P	1s2 2s, 2S	0.338	2021.3	0.3258
D	AlXI	4d, 2D	2p, 2P	0.317	6728.6	1.0845
E	AlXI	4d, 2D	3p, 2P	0.082	539.0	0.0868
F	AlXI	4f, 2F	3d, 2D	0.080	1503.5	0.2423
G	AlX	2S2P,1P	G 2S(2),1S	0.037	224.6	0.0362
H	AlX	2P(2),3P	2S2P,3P	0.036	352.3	0.0567
I	AlX	2P(2),1SD	2S2P,1P	0.020	59.4	0.0095
J	AlX	2S3 ,T	2S2P,3P	0.221	1798.0	0.2898
K	AlX	2S3 ,S	2S2P,1P	0.205	1611.2	0.2919
L	AlX	2S3 ,S	G 2S(2),1S	0.242	815.4	0.1314
M	AlX	2P(2),2SPIE	2P,2P	0.036	1140.2	0.1837
N	AlX	2P(3),4S	2P(2),4P	0.038	361.0	0.0582

Fig. 6

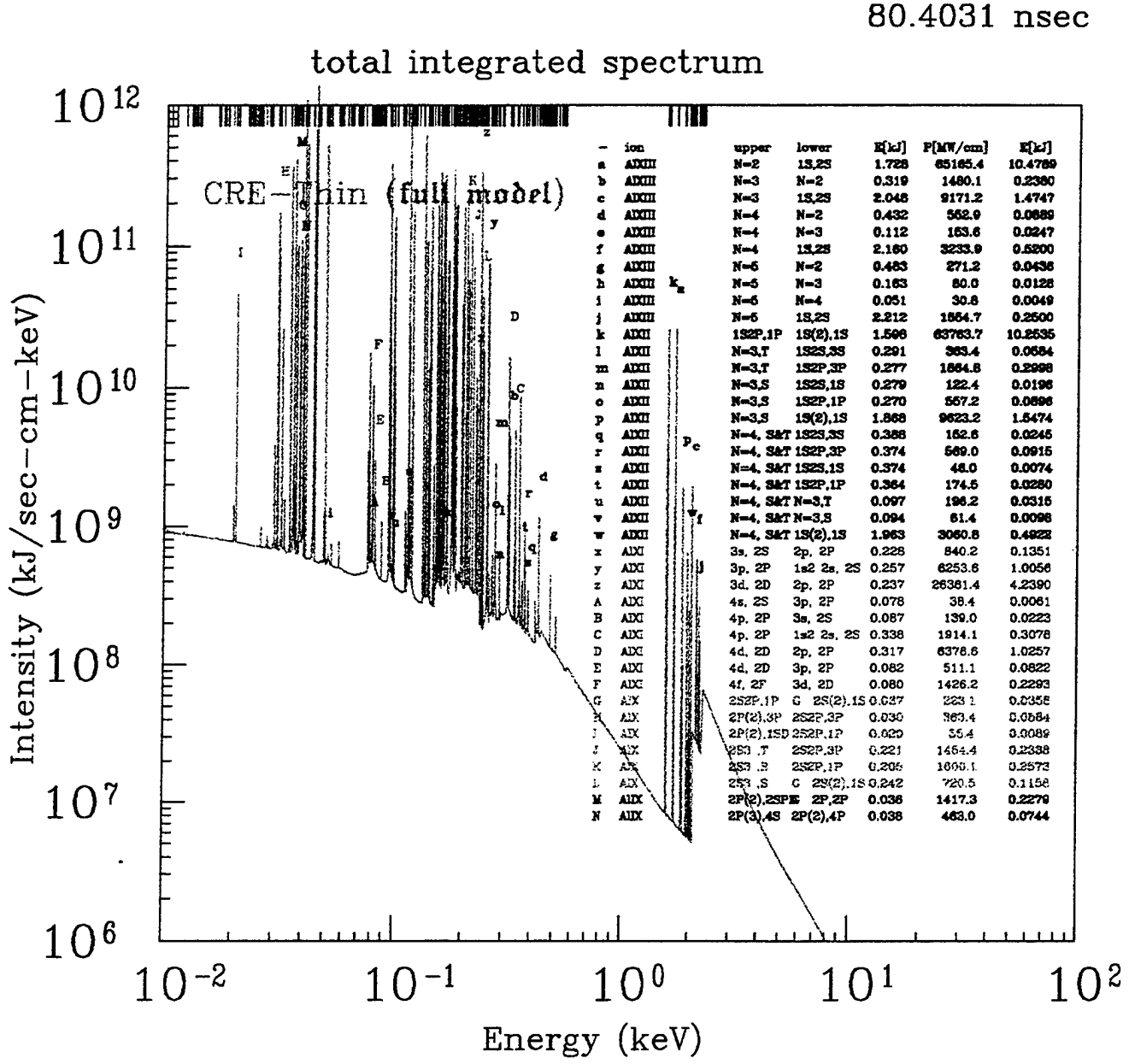

-	ion	upper	lower	E[kJ]	P[MW/cm]	E[kJ]
a	AlXIII	N=2	1S,2S	1.728	65165.4	10.4789
b	AlXIII	N=3	N=2	0.319	1480.1	0.2380
c	AlXIII	N=3	1S,2S	2.048	9171.2	1.4747
d	AlXIII	N=4	N=2	0.432	552.9	0.0889
e	AlXIII	N=4	N=3	0.112	153.6	0.0247
f	AlXIII	N=4	1S,2S	2.160	3233.9	0.5200
g	AlXIII	N=5	N=2	0.483	271.2	0.0436
h	AlXIII	N=5	N=3	0.163	80.0	0.0128
i	AlXIII	N=5	N=4	0.051	30.8	0.0049
j	AlXIII	N=5	1S,2S	2.212	1554.7	0.2500
k	AlXII	1S2P,1P	1S(2),1S	1.566	63763.7	10.2535
l	AlXII	N=3,T	1S2S,3S	0.291	363.4	0.0584
m	AlXII	N=3,T	1S2P,3P	0.277	1864.8	0.2998
n	AlXII	N=3,S	1S2S,1S	0.279	122.4	0.0196
o	AlXII	N=3,S	1S2P,1P	0.270	557.2	0.0896
p	AlXII	N=3,S	1S(2),1S	1.868	9623.2	1.5474
q	AlXII	N=4, S&T	1S2S,3S	0.388	152.6	0.0245
r	AlXII	N=4, S&T	1S2P,3P	0.374	569.0	0.0915
s	AlXII	N=4, S&T	1S2S,1S	0.374	46.0	0.0074
t	AlXII	N=4, S&T	1S2P,1P	0.364	174.5	0.0280
u	AlXII	N=4, S&T	N=3,T	0.097	196.2	0.0315
v	AlXII	N=4, S&T	N=3,S	0.094	61.4	0.0098
w	AlXII	N=4, S&T	1S(2),1S	1.963	3060.8	0.4922
x	AlXI	3s, 2S	2p, 2P	0.228	840.2	0.1351
y	AlXI	3p, 2P	1s2 2s, 2S	0.257	6253.6	1.0056
z	AlXI	3d, 2D	2p, 2P	0.237	26381.4	4.2390
A	AlXI	4s, 2S	3p, 2P	0.078	38.4	0.0061
B	AlXI	4p, 2P	3s, 2S	0.087	139.0	0.0223
C	AlXI	4p, 2P	1s2 2s, 2S	0.338	1914.1	0.3078
D	AlXI	4d, 2D	2p, 2P	0.317	6376.6	1.0257
E	AlXI	4d, 2D	3p, 2P	0.082	511.1	0.0822
F	AlXI	4f, 2F	3d, 2D	0.080	1426.2	0.2293
G	AlX	2S2P,1P	G 2S(2),1S	0.027	223.1	0.0358
H	AlX	2P(2),3P	2S2P,3P	0.030	363.4	0.0584
I	AlX	2P(2),1SD	2S2P,1P	0.020	55.4	0.0089
J	AlX	2S3 ,T	2S2P,3P	0.221	1454.4	0.2338
K	AlX	2S3 ,S	2S2P,1P	0.205	1600.1	0.2573
L	AlX	2S3 ,S	G 2S(2),1S	0.242	720.5	0.1158
M	AlIX	2P(2),2SPE	2P,2P	0.036	1417.3	0.2279
N	AlIX	2P(3),4S	2P(2),4P	0.038	463.0	0.0744

Fig. 7

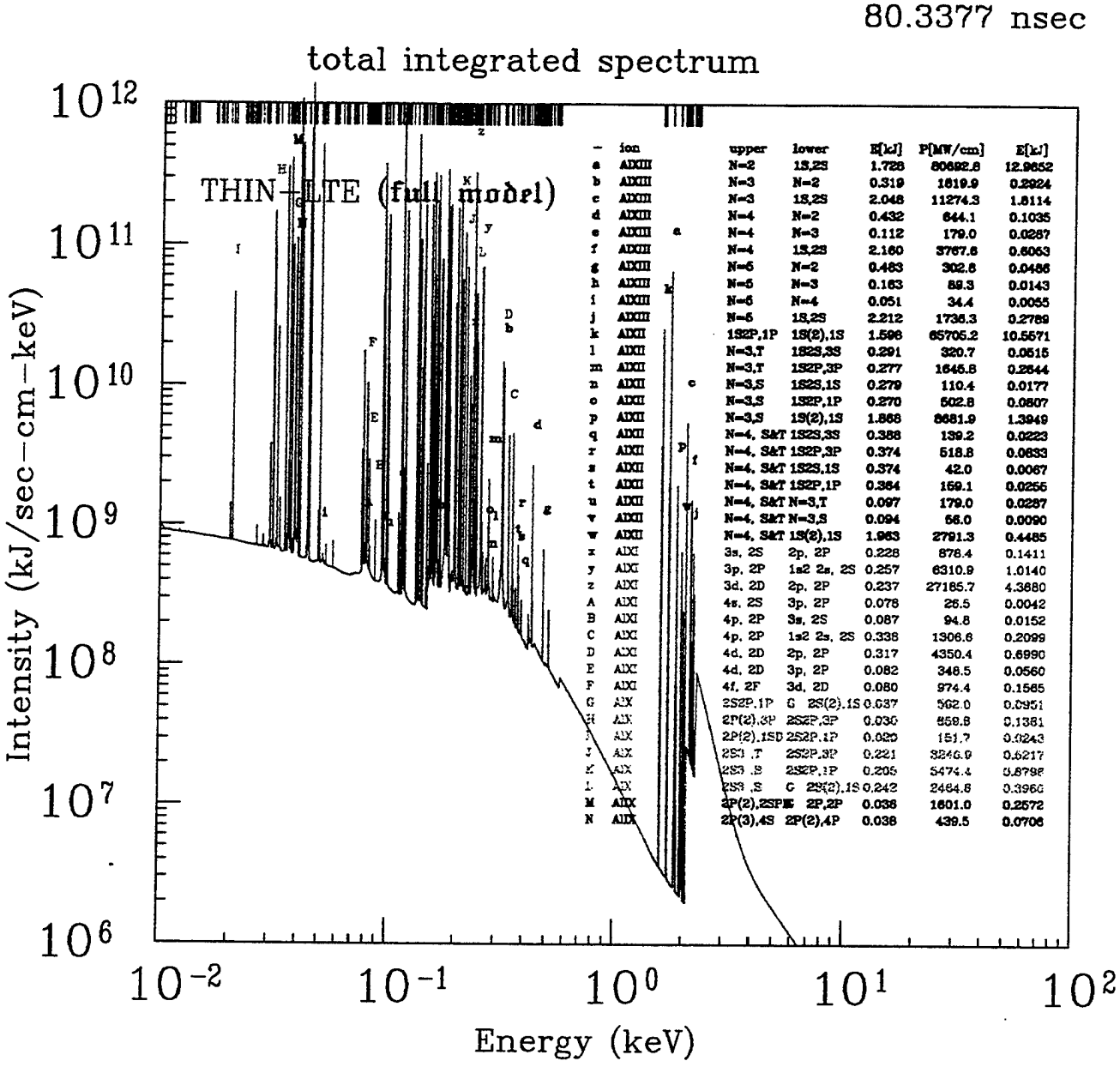
80.3377 nsec
total integrated spectrum
THIN-LTE (full model)
Intensity (kJ/sec-cm-keV)
Energy (keV)
10^{12}
10^{11}
10^{10}
10^{9}
10^{8}
10^{7}
10^{6}
10^{-2}
10^{-1}
10^{0}
10^{1}
10^{2}
– ion upper lower E[kJ] P[MW/cm] E[kJ]
a AlXIII N=2 1S,2S 1.726 80692.8 12.9652
b AlXIII N=3 N=2 0.319 1619.9 0.2924
c AlXIII N=3 1S,2S 2.048 11274.3 1.8114
d AlXIII N=4 N=2 0.432 644.1 0.1035
e AlXIII N=4 N=3 0.112 179.0 0.0287
f AlXIII N=4 1S,2S 2.160 3767.6 0.6053
g AlXIII N=5 N=2 0.483 302.8 0.0486
h AlXIII N=5 N=3 0.163 89.3 0.0143
i AlXIII N=6 N=4 0.051 34.4 0.0055
j AlXIII N=5 1S,2S 2.212 1736.3 0.2789
k AlXII 1S2P,1P 1S(2),1S 1.596 65705.2 10.5571
l AlXII N=3,T 1S2S,3S 0.291 320.7 0.0515
m AlXII N=3,T 1S2P,3P 0.277 1645.8 0.2644
n AlXII N=3,S 1S2S,1S 0.279 110.4 0.0177
o AlXII N=3,S 1S2P,1P 0.270 502.8 0.0807
p AlXII N=3,S 1S(2),1S 1.868 8681.9 1.3949
q AlXII N=4, S&T 1S2S,3S 0.388 139.2 0.0223
r AlXII N=4, S&T 1S2P,3P 0.374 518.8 0.0833
s AlXII N=4, S&T 1S2S,1S 0.374 42.0 0.0067
t AlXII N=4, S&T 1S2P,1P 0.364 159.1 0.0255
u AlXII N=4, S&T N=3,T 0.097 179.0 0.0287
v AlXII N=4, S&T N=3,S 0.094 56.0 0.0090
w AlXII N=4, S&T 1S(2),1S 1.963 2791.3 0.4485
x AlXI 3s, 2S 2p, 2P 0.228 878.4 0.1411
y AlXI 3p, 2P 1s2 2s, 2S 0.257 6310.9 1.0140
z AlXI 3d, 2D 2p, 2P 0.237 27185.7 4.3680
A AlXI 4s, 2S 3p, 2P 0.078 26.5 0.0042
B AlXI 4p, 2P 3s, 2S 0.087 94.8 0.0152
C AlXI 4p, 2P 1s2 2s, 2S 0.338 1306.6 0.2099
D AlXI 4d, 2D 2p, 2P 0.317 4350.4 0.6990
E AlXI 4d, 2D 3p, 2P 0.082 348.5 0.0560
F AlXI 4f, 2F 3d, 2D 0.080 974.4 0.1565
G AlX 2S2P,1P G 2S(2),1S 0.037 562.0 0.0951
H AlX 2P(2),3P 2S2P,3P 0.030 859.8 0.1381
I AlX 2P(2),1SD 2S2P,1P 0.020 151.7 0.0243
J AlX 2S1 ,T 2S2P,3P 0.221 3846.9 0.6217
K AlX 2S3 ,S 2S2P,1P 0.205 5474.4 0.8798
L AlX G 2S(2),1S 0.242 2464.6 0.3960
M AlX 2P(2),2SPIE 2P,2P 0.038 1601.0 0.2572
N AlX 2P(3),4S 2P(2),4P 0.038 439.5 0.0706

Fig. 8

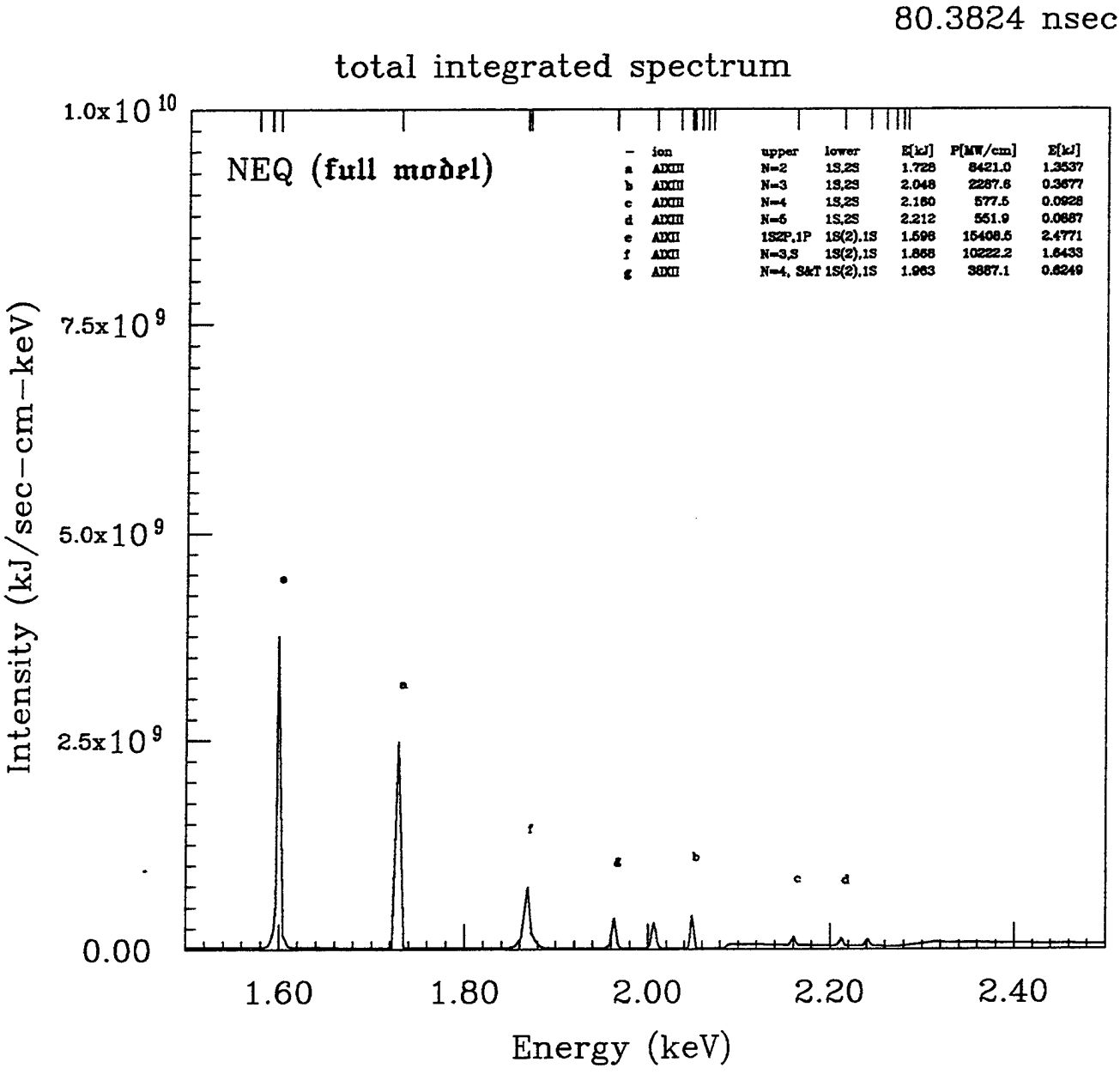
80.3824 nsec
total integrated spectrum
NEQ (full model)
1.0x10 10
7.5x10 9
5.0x10 9
2.5x10 9
0.00
Intensity (kJ/sec-cm-keV)
1.60
1.80
2.00
2.20
2.40
Energy (keV)
– ion upper lower E[kJ] P[MW/cm] E[kJ]
a AlXIII N=2 1S,2S 1.728 8421.0 1.3537
b AlXIII N=3 1S,2S 2.048 2287.6 0.3677
c AlXIII N=4 1S,2S 2.160 577.5 0.0928
d AlXIII N=5 1S,2S 2.212 551.9 0.0887
e AlXII 1S2P,1P 1S(2).1S 1.598 15408.5 2.4771
f AlXII N=3,S 1S(2),1S 1.858 10222.2 1.6433
g AlXII N=4, S&T 1S(2),1S 1.963 3887.1 0.6249

Fig. 9

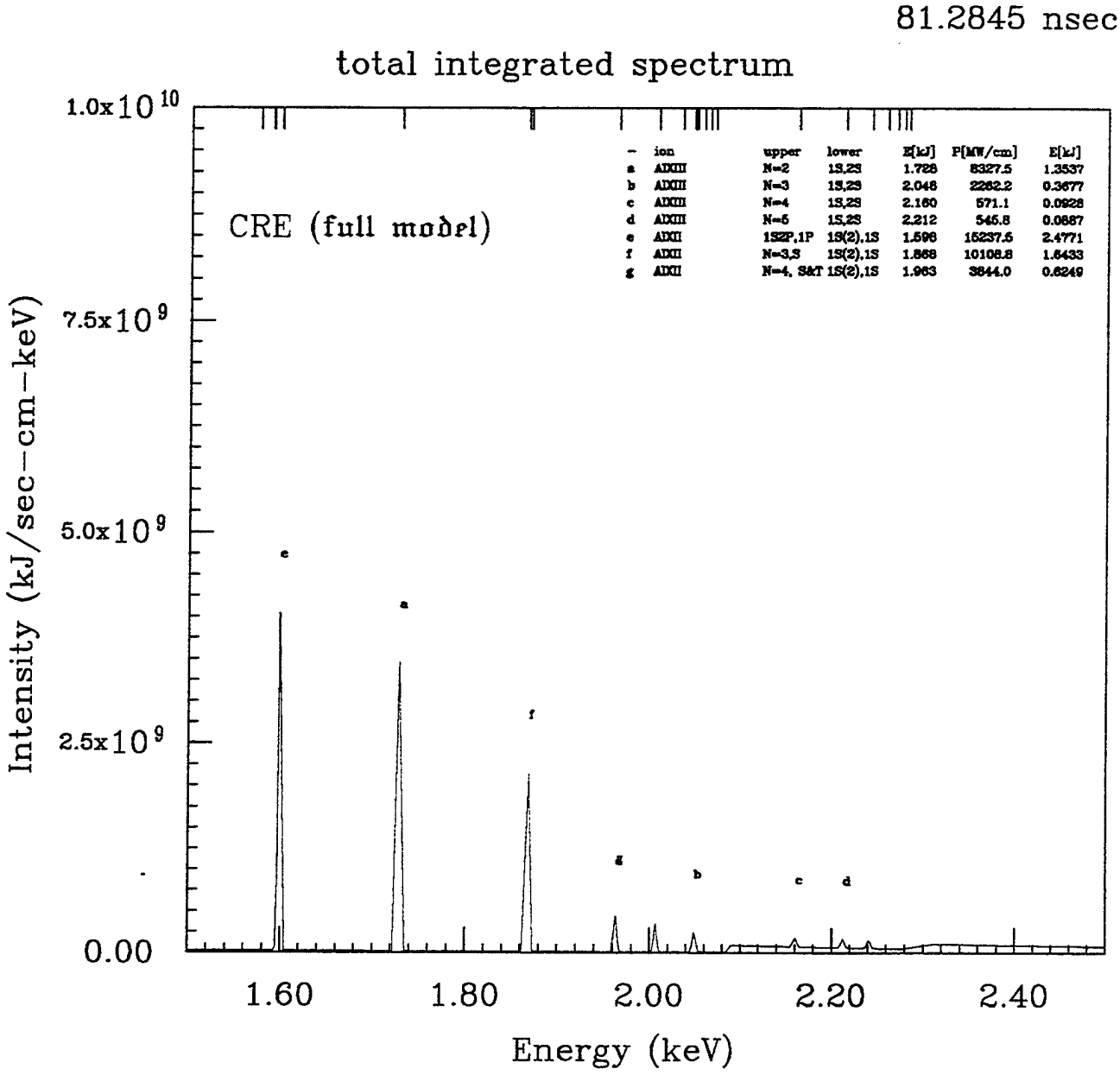
81.2845 nsec
total integrated spectrum
CRE (full model)
– ion upper lower E[kJ] P[MW/cm] E[kJ]
a AlXIII N=2 1S,2S 1.728 8327.5 1.3537
b AlXIII N=3 1S,2S 2.048 2282.2 0.3677
c AlXIII N=4 1S,2S 2.160 571.1 0.0928
d AlXIII N=5 1S,2S 2.212 545.8 0.0887
e AlXII 1S2P,1P 1S(2),1S 1.596 15237.5 2.4771
f AlXII N=3,S 1S(2),1S 1.868 10108.8 1.6433
g AlXII N=4, S&T 1S(2),1S 1.963 3844.0 0.6249
1.0x10 10
7.5x10 9
5.0x10 9
2.5x10 9
0.00
Intensity (kJ/sec-cm-keV)
1.60
1.80
2.00
2.20
2.40
Energy (keV)

Fig. 10

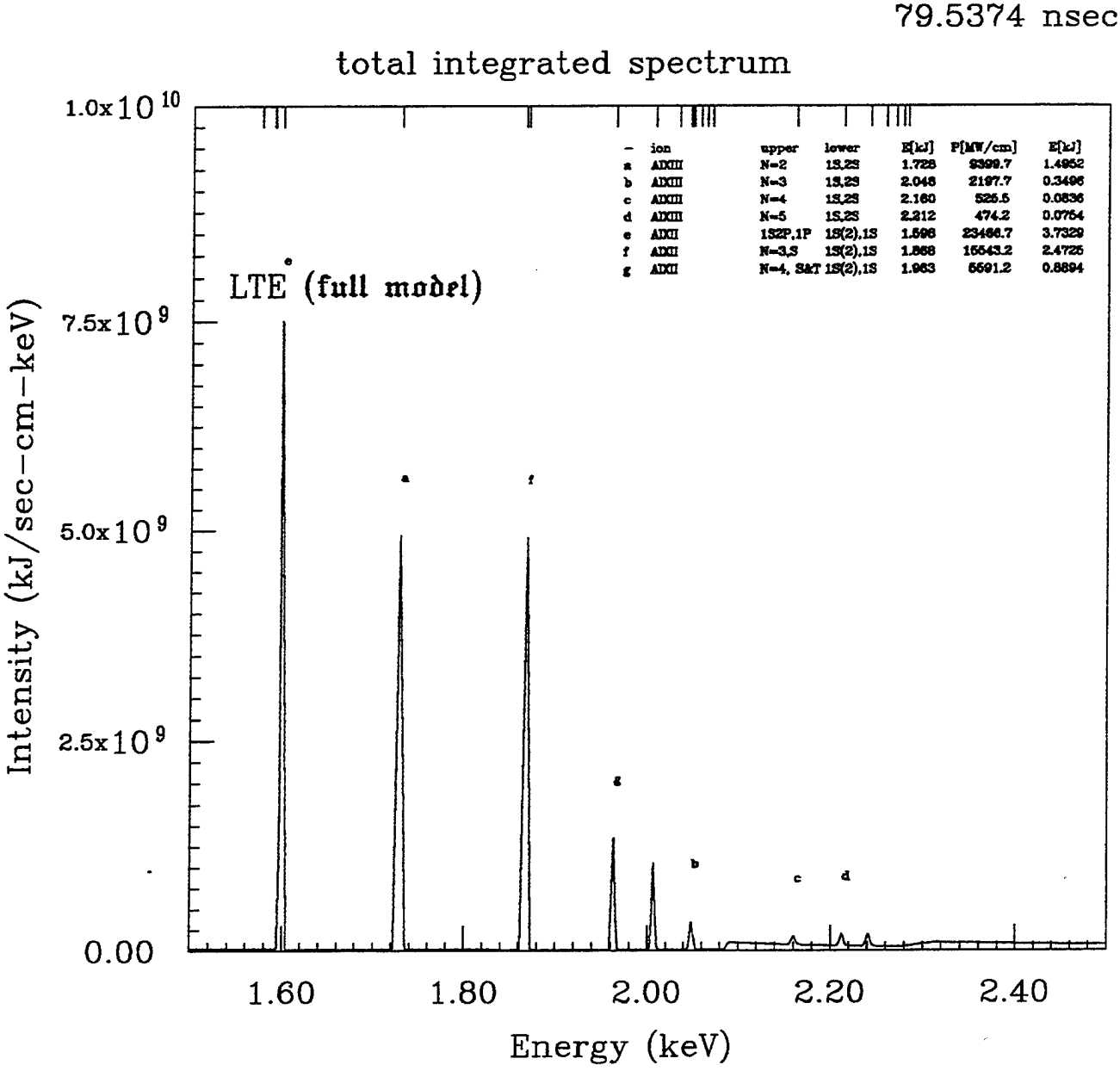
79.5374 nsec
total integrated spectrum
LTE (full model)
Intensity (kJ/sec-cm-keV)
1.0x10 10
7.5x10 9
5.0x10 9
2.5x10 9
0.00
1.60
1.80
2.00
2.20
2.40
Energy (keV)
- ion upper lower E[kJ] P[MW/cm] E[kJ]
a AlXIII N=2 1S,2S 1.728 9399.7 1.4952
b AlXIII N=3 1S,2S 2.048 2197.7 0.3496
c AlXIII N=4 1S,2S 2.160 526.5 0.0836
d AlXIII N=5 1S,2S 2.212 474.2 0.0754
e AlXI 1S2P,1P 1S(2),1S 1.596 23466.7 3.7329
f AlXII N=3,S 1S(2),1S 1.868 15643.2 2.4725
g AlXII N=4, S&T 1S(2),1S 1.963 5591.2 0.8894

Fig. 11

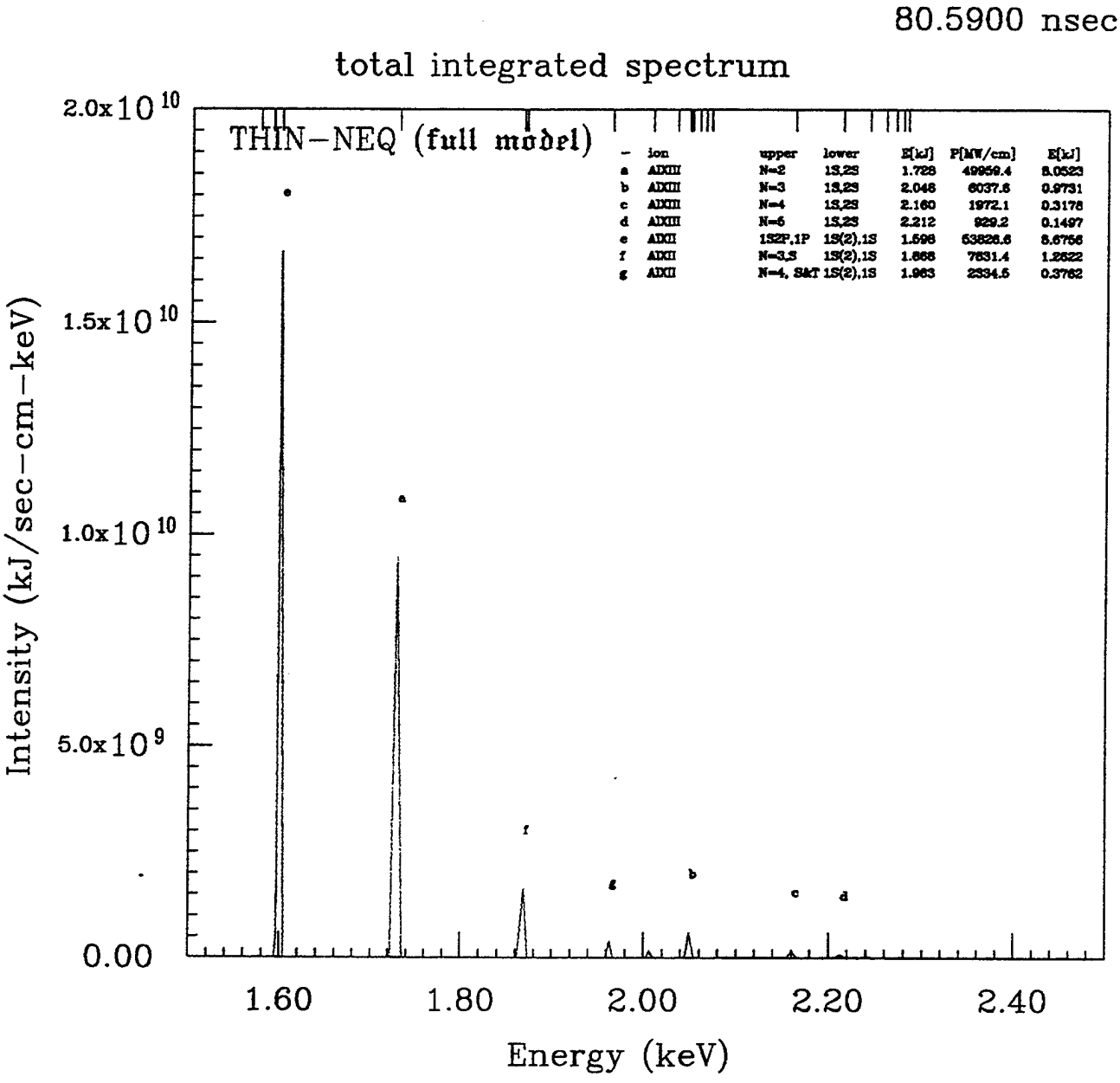
80.5900 nsec
total integrated spectrum
THIN-NEQ (full model)
2.0x10 10
1.5x10 10
1.0x10 10
5.0x10 9
0.00
Intensity (kJ/sec-cm-keV)
1.60
1.80
2.00
2.20
2.40
Energy (keV)
- ion upper lower E[kJ] P[MW/cm] E[kJ]
a AlXIII N=2 1S,2S 1.728 49959.4 8.0523
b AlXIII N=3 1S,2S 2.048 6037.6 0.9731
c AlXIII N=4 1S,2S 2.160 1972.1 0.3178
d AlXIII N=5 1S,2S 2.212 929.2 0.1497
e AlXII 1S2P,1P 1S(2),1S 1.596 53826.6 8.6756
f AlXII N=3,S 1S(2),1S 1.668 7831.4 1.2622
g AlXII N=4, S&T 1S(2),1S 1.963 2334.5 0.3762

Fig. 12

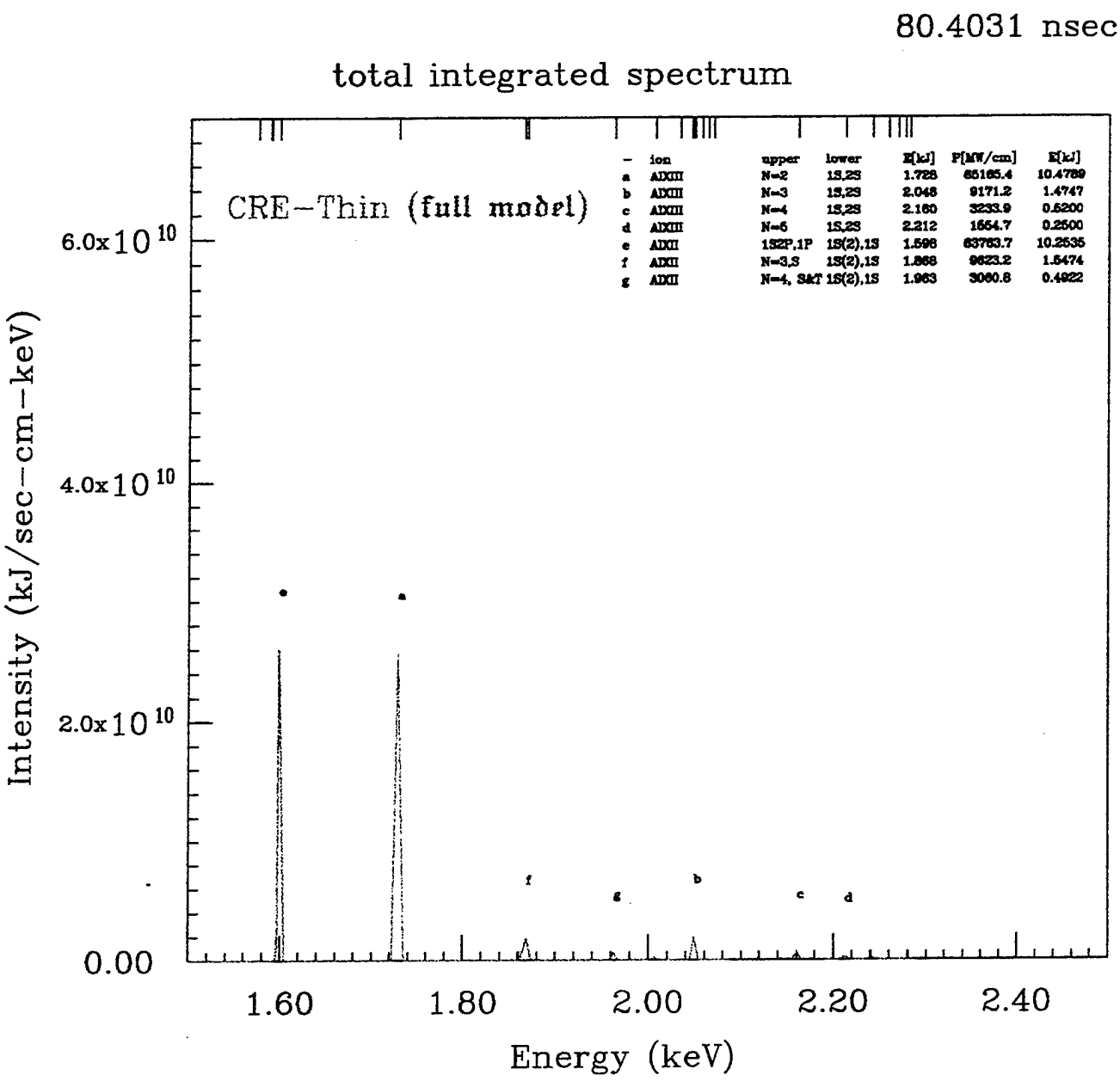
80.4031 nsec
total integrated spectrum
CRE-Thin (full model)
– ion upper lower E[kJ] P[MW/cm] E[kJ]
a AlXIII N=2 1S,2S 1.728 65165.4 10.4789
b AlXIII N=3 1S,2S 2.048 9171.2 1.4747
c AlXIII N=4 1S,2S 2.160 3233.9 0.5200
d AlXIII N=5 1S,2S 2.212 1554.7 0.2500
e AlXII 1S2P,1P 1S(2),1S 1.598 63763.7 10.2535
f AlXII N=3,S 1S(2),1S 1.868 9623.2 1.5474
g AlXII N=4, S&T 1S(2),1S 1.963 3060.8 0.4922
6.0x10 10
4.0x10 10
2.0x10 10
0.00
Intensity (kJ/sec-cm-keV)
1.60
1.80
2.00
2.20
2.40
Energy (keV)

Fig. 13

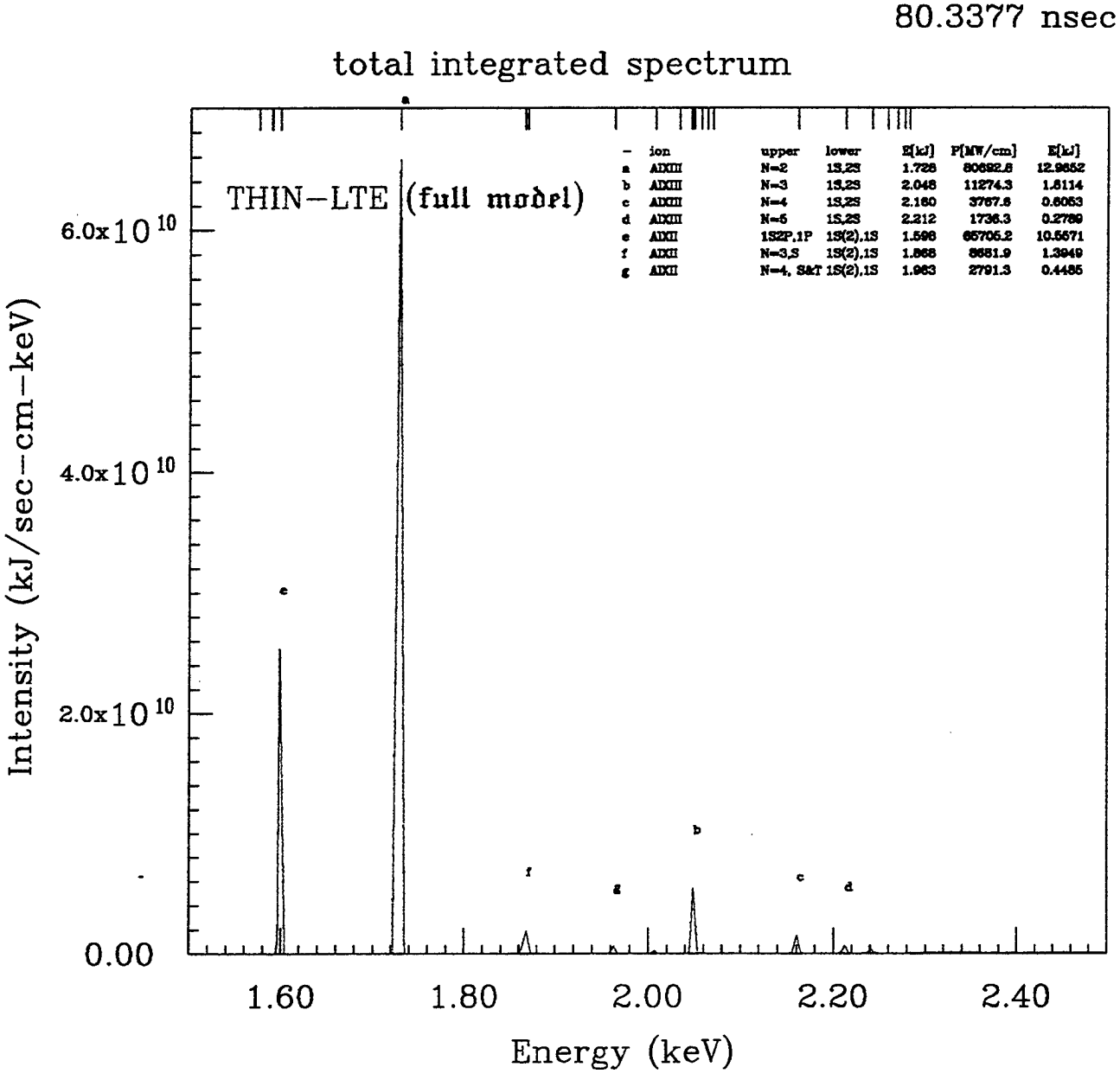
80.3377 nsec
total integrated spectrum
THIN−LTE (full model)
– ion upper lower E[kJ] P[MW/cm] E[kJ]
a AlXIII N=2 1S,2S 1.728 80692.8 12.9652
b AlXIII N=3 1S,2S 2.048 11274.3 1.8114
c AlXIII N=4 1S,2S 2.160 3767.8 0.6053
d AlXIII N=5 1S,2S 2.212 1736.3 0.2789
e AlXII 1S2P,1P 1S(2),1S 1.596 65705.2 10.5571
f AlXII N=3,S 1S(2),1S 1.868 8681.9 1.3949
g AlXII N=4, S&T 1S(2),1S 1.963 2791.3 0.4485
6.0x10 10
4.0x10 10
2.0x10 10
0.00
Intensity (kJ/sec−cm−keV)
1.60
1.80
2.00
2.20
2.40
Energy (keV)

Fig. 14